Self-purifying $La_{2/3}Sr_{1/3}MnO_3$ epitaxial films: Observation of surface precipitation of Mn_3O_4 particles for excess Mn ratios

Alexandra Steffen

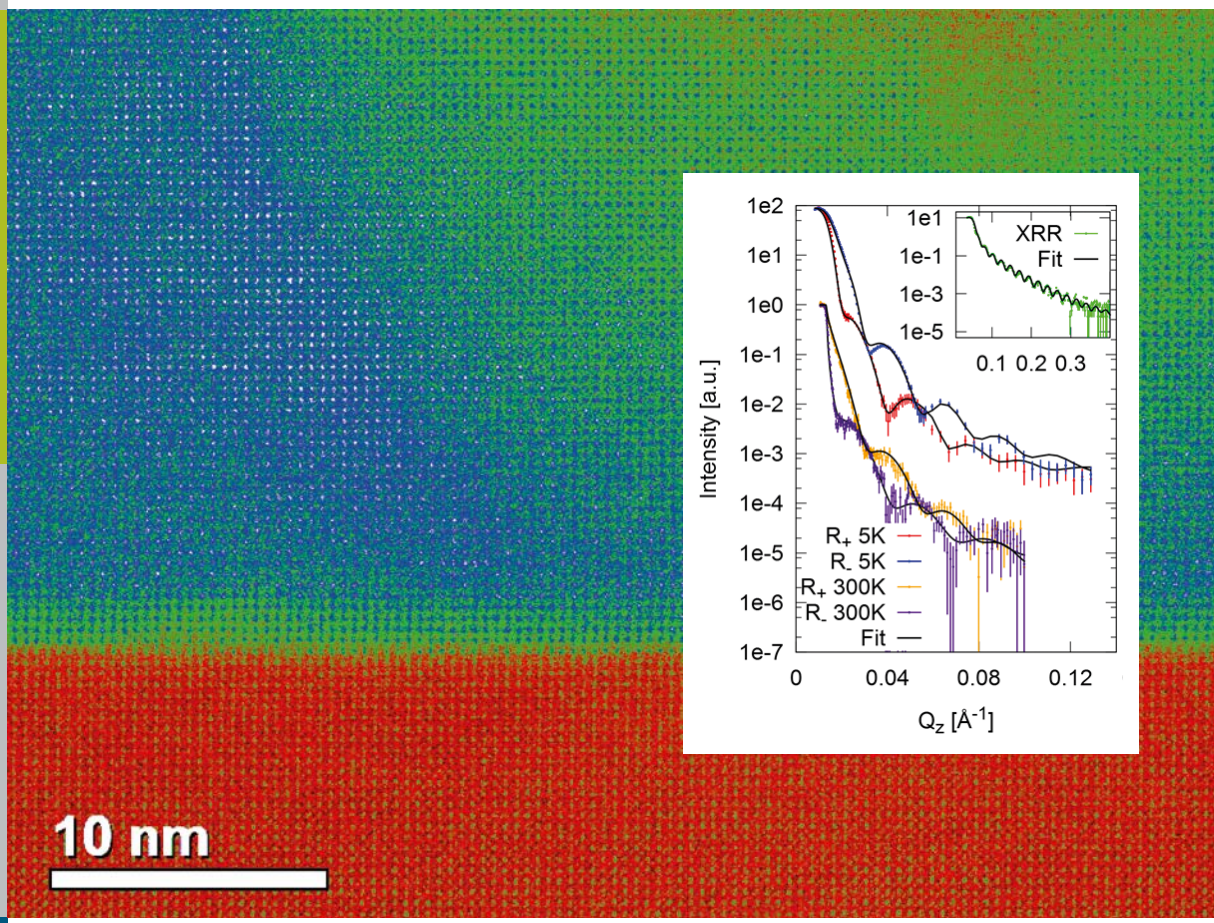

Member of the Helmholtz Association

Schlüsseltechnologien / Key Technologies
Band / Volume 128
ISBN 978-3-95806-162-0

JÜLICH FORSCHUNGSZENTRUM

Schriften des Forschungszentrums Jülich
Reihe Schlüsseltechnologien / Key Technologies Band / Volume 128

Forschungszentrum Jülich GmbH
Jülich Centre for Neutron Science
JCNS

Self-purifying $La_{2/3}Sr_{1/3}MnO_3$ epitaxial films: Observation of surface precipitation of Mn_3O_4 particles for excess Mn ratios

Alexandra Steffen

Schriften des Forschungszentrums Jülich
Reihe Schlüsseltechnologien / Key Technologies Band / Volume 128

ISSN 1866-1807 ISBN 978-3-95806-162-0

Bibliographic information published by the Deutsche Nationalbibliothek.
The Deutsche Nationalbibliothek lists this publication in the Deutsche Nationalbibliografie; detailed bibliographic data are available in the Internet at http://dnb.d-nb.de.

Publisher and Distributor: Forschungszentrum Jülich GmbH
Zentralbibliothek
52425 Jülich
Tel: +49 2461 61-5368
Fax: +49 2461 61-6103
Email: zb-publikation@fz-juelich.de
www.fz-juelich.de/zb

Cover Design: Grafische Medien, Forschungszentrum Jülich GmbH

Printer: Grafische Medien, Forschungszentrum Jülich GmbH

Schriften des Forschungszentrums Jülich
Reihe Schlüsseltechnologien / Key Technologies, Band / Volume 128

D 82 (Diss., RWTH Aachen University, 2016)

ISSN 1866-1807
ISBN 978-3-95806-162-0

The complete volume is freely available on the Internet on the Jülicher Open Access Server (JuSER) at www.fz-juelich.de/zb/openaccess.

Zusammenfassung

20-25 nm dünne Schichten basierend auf $La_{2/3}Sr_{1/3}MnO_3$ (LSMO) werden mittels Oxide Molecular Beam Epitaxy (MBE, Molekularstrahlepitaxie) hergestellt. Verschiedene Arten der Effusionszellen-Shutteröffnungsintervalle werden benutzt, um Proben per Co-Deposition und Shuttered Deposition herzustellen. In-situ Reflection High-Energy Electron Diffraction (RHEED, Beugung hochenergetischer Elektronen bei Reflexion)-Intensitätsmessungen werden in Abhängigkeit von der Evaporationszeit durchgeführt. Die RHEED-Intensitäten weisen deutlich ausgeprägte Oszillationen auf, was auf eine Schichtanordnung hindeutet, deren Stöchiometrie durch die Shutteröffnungsintervalle kontrolliert wird, insbesondere der $La_{2/3}Sr_{1/3}O$ vs. MnO-Zusammensetzung. Innerhalb der LSMO-Filme werden vertikal stöchiometrisch konstante und stöchiometrische Gradientenstrukturen erzeugt.

Low Energy Electron Diffraction (LEED, Beugung niederenergetischer Elektronen) und X-Ray Diffraction (XRD, Röntgendiffraktion) weisen die Bragg-Reflexe auf, die im Falle epitaktischen Wachstums der dünnen Schichten erwartet werden. X-Ray Reflectivity (XRR, Röntgenreflektometrie) bestätigt nominelle Schichtdicke und -komposition.

Um die magnetische Schichtdicke zu bestimmen und zu erfahren, ob ein magnetischer Gradient innerhalb des strukturellen Gradienten entstanden ist, werden Polarisierte Neutronen-Reflektometriemessungen (PNR) durchgeführt und evaluiert. Das tiefenabhängige Magnetisierungsverhalten ergibt nicht die erwartete Probenstruktur. Eine kombinierte Verfeinerung von Röntgen- und Neutronenreflektometriedaten benötigt einen MnO_x-Überschuss an der Oberfläche im Modell der Streulängendichte. Ergänzende High-Resolution Transmission Electron Microscopy (HRTEM, Hochauflösende Transmissionselektronenmikroskopie)-Bilder enthüllen die Existenz einer homogenen LSMO-Schicht mit Perowskit-Struktur samt eingeschlossenen MnO_x-Präzipitaten. Detailierte SQUID-Messungen lassen vermuten, dass die Präzipitate eine Mn_3O_4-Stöchiometrie aufweisen.

Aufgrund der Kombination von verschienenen experimentellen Methoden konnte die Differenz zwischen nomineller und tatsächlicher Schichtkomposition identifiziert werden. Dies zeigt, dass LSMO bevorzugt als reine $La_{2/3}Sr_{1/3}MnO_3$-Perowskit-Phase auf $SrTiO_3$ wächst. Die Beobachtung dieser Phasenseparation wird diskutiert.

Abstract

20-25 nm thin films based $La_{2/3}Sr_{1/3}MnO_3$ (LSMO) are prepared via Oxide Molecular Beam Epitaxy setup (MBE). Different ways of effusion cell shutter opening intervals are used to produce samples in co-deposition and shuttered mode. In-situ Reflection High-Energy Electron Diffraction (RHEED) intensity measurements in dependence of evaporation time are performed. The RHEED intensities exhibit distinct oscillations, indicating a stacking of layers with a stoichiometry controlled by the shutter opening times, in particular of the $La_{2/3}Sr_{1/3}O$ vs. MnO content. Inside the thin LSMO films, vertical stoichiometric constant and gradient structures are produced.

Low Energy Electron Diffraction (LEED) and X-Ray Diffraction (XRD) exhibit the Bragg reflections expected for epitaxial growth of the thin films. XRR analysis is in agreement with the nominal layer thickness and composition.

To determine the magnetic layer thickness and to see whether a magnetic gradient inside the structural gradient takes place, Polarized Neutron Reflectometry (PNR) measurements are performed and evaluated. The depth-dependent magnetization behavior does not render the anticipated sample structure. A combined refinement of XRR and PNR data requires MnO_x excess towards the surfaces in the model of the scattering length density. Additional High-Resolution Transmission Electron Microscopy (HRTEM) images reveal the existence of pure homogeneous perovskite LSMO layers with enclaved MnO_x precipitates. Detailed SQUID measurements indicate these particles to have a Mn_3O_4 stoichiometry.

Due to the combination of different experimental methods, the difference between the nominal and the actual layer composition can be identified showing that LSMO prefers to grow in pure $La_{2/3}Sr_{1/3}MnO_3$ perovskite phase on $SrTiO_3$. The observation of this phase separation effect will be discussed.

Contents

Chapter 1

Introduction

Transition metal oxides with strong electronic correlations which show effects like spin-orbital ordering, unconventional superconductivity, colossal magnetoresistance or formation of 2d electron gas at interfaces are currently of large interest due to their potential applications in novel electronic devices. One of the most often investigated systems is the oxide $La_{1-x}Sr_xMnO_3$/ $SrTiO_3$ (LSMO/STO), in particular with the composition x=1/3, because of its ferromagnetic-paramagnetic transition far above room temperature.

However, the phase diagram of ($La_{1-x}Sr_x$) vs. Mn for x=1/3 is far less explored. On the one hand thin films produced by co-deposition of (La/Sr) and Mn lead to Mn atoms at the (La/Sr) position in case of Mn excess [1], on the other hand layer-by-layer-growth was only used to produce members of the Ruddlesden-Popper series via (La/Sr) overdoping [2].

The purpose of this investigation was to probe the modulation of the magnetization inside the sample resulting from stoichiometric gradients. Therefore different multilayers consisting of $La_{2/3}Sr_{1/3}O$ (LSO) and MnO_2 (MO) were grown on top of STO (001) substrates, every sample with a total layer thickness of approximately 250 Å. For this work, first $La_{2/3}Sr_{1/3}Mn_1O_3$ was prepared. After verifying the stoichiometry and comparing the physical properties with literature, the stoichiometry of LSO vs. MO was varied.

The reference system $La_{2/3}Sr_{1/3}Mn_1O_3$ is known to influence magnetism in neighboring layers like inducing magnetic moments at the Ti atom in LSMO/STO heterostructures [3] or introducing ferromagnetic inclusions within the antiferromagnetic $Pr_{2/3}Ca_{1/3}MnO_3$ layers in LSMO/$Pr_{2/3}Ca_{1/3}MnO_3$ superlattices [4]. Rocksalt monolayers are known to influence the magnetic coupling [5]. Here, the system was systematically overdoped with MnO layers. To identify the real MnO contribution, not only simple constant LS_xM_yO stoichiometries were selected, but graded manganites produced to test if the magnetization is following the stoichiometric gradient.

The tailored stoichiometry and in addition production of stoichiometric gradients within a sample was attempted via the shuttered growth technique. With polarized neutron reflectometry the impact of this localized alteration of stoichiometry was probed in order to reveal the magnetic depth profile as correlation of regional stoichiometry to provide more insight into the additional layer contribution to the magnetism.

All samples were grown by utilizing the oxide Molecular Beam Epitaxy (MBE) system of Jülich Centre for Neutron Science at Heinz Maier-Leibnitz Zentrum (JCNS@MLZ) [6]. These structures are not feasible in bulk or powder; only the combination of shuttered growth and in-situ RHEED control enables one to produce such structures. Pulsed Laser Deposition (PLD) and

sputter systems require targets to produce a certain stoichiometry [7]. Via MBE deposition, a stoichiometry is introduced by setting of rate of evaporation from the effusion cells, monitored via quartz crystal balance. Before each sample preparation, the growth rates were calibrated. Various 200 Å to 250 Å thick films were prepared as reference samples with a constant stoichiometry like $(LS)_2M_3O$ to determine the properties of the individual stoichiometry.

Samples were produced to relate in-sample-varied (La/Sr) concentration vs. Mn concentration to the magnetic depth profile. The used "shuttered growth" technique modifies the stoichiometry within a sample via opening and closing the shutters of effusion cells individually and therefore giving the opportunity to control atomic layer by atomic layer the composition. For this work, the advantages of an Oxide Molecular Beam Epitaxy setup were utilized, where additional rocksalt structured layers can be introduced into a ABO_3 perovskite system by individually opening shutters of the A or B effusion cells during growth [8]. In-situ performed RHEED (Reflection High Energy Electron Diffraction) measurements of intensity oscillations of the specular spot were used to achieve and control the specific stoichiometry with the aim to reveal the magnetic modulation in the magnetic depth profile to explore the influence of the local stoichiometry. These stoichiometric changes were expected to manipulate the profile following the structural changes.

The projected sample preparation protocol of this thesis did not render the anticipated sample structure. Via PNR instead of the assumed stoichiometric gradients, the samples were found to have an increased Mn excess towards the surface. TEM images revealed the existence of pure stoichiometric perovskite LSMO films without any rock salt structures and additionally MnO_x precipitates. The volume of the precipitates inside the whole sample was quantified and via SQUID the precipitate stoichiometry was determined to be Mn_3O_4.

This thesis is divided into following chapters:

In this chapter, the topic and the idea were introduced. Chapter 2 provides the theoretical background. Chapter 3 introduces the experimental methods. Since the sample preparation was an important part of this thesis, the used method is explained in detail in chapter 4

As first samples, co-deposited LSMO was produced multiple times to evaluate the sample quality as well as the sample reproducibility in chapter 5. In chapter 6, the samples grown via the shuttered growth technique are introduced. After preparation and standard characterization, they are investigated in chapter 7 via PNR to check their magnetic profile and the TEM data are shown and discussed. With respect to these PNR and TEM-based findings, the observed features are investigated more detailed in chapter 8.

The results are discussed in chapter 9 and an outlook is given in chapter 10. Finally, the work is summarized in chapter 11.

In the appendix B the prepared MBE scripts are shown, logfiles are displayed in appendix C, and the used symbols and abbreviations are listed in appendix D.

In the following, the targeted, nominal sample stoichiometry is written behind the sample number, e.g. sample 288 ($(LS)_2M_1O$); this is not necessarily equal to the real sample stoichiometry.

Chapter 2

Theoretical background

2.1 Correlated electron systems and perovskite structure ABO_3

Transition metal oxides are prime examples for strongly correlated electron systems. Here, the electrons are neither fully localized as in ionic crystals, nor delocalized as in metals, so that e.g. the band model cannot be applied. For the here used bondings, the ionic contribution is in the range of 60 % to 70 %. Models featuring independent electrons do not describe these systems correctly.

In strongly correlated electron systems, long-range Coulomb interaction has to be taken into account and the motion of one electron is influenced by all other electrons. Hence properties of strongly correlated electron systems cannot be described by single particle approaches. Examples for materials, where strong electronic correlations play an important role are high temperature superconductors like YBCO, multiferroics like $LuFeO_3$ or ferroelectrics like $BaTiO_3$. For fascinating reviews of these effects in transistion metal oxides, see e.g. [9–13]. $La_{1-x}Sr_xMnO_3$ shows a variety of interesting characteristics like the colossal magnetoresistance (CMR effect) or the giant magnetostriction effect, it demonstrates a high spin polarization and the Curie temperature is above 350 K [14].

The crystallographic structures used in this work are displayed in fig. 2.1. The rock salt structure in fig. 2.1a consists of two face-centered lattices, shifted by half of the lattice constant. In the perovskite structure ABO_3 in fig. 2.1b the central atom B, here Mn or Ti, in the middle of the unit cell is surrounded by six oxygen atoms forming an octahedron, which is framed by a cube. At the cubes corners the A atoms are located. The structure of Ruddlesden-Popper series $A_{n+1}B_nO_{3n+1}$ consisits of perovskite cubes with additional layers of one atom height introduced as rock salt layers. In fig. 2.1c, the Ruddlesden-Popper member n=2 is shown.

While $SrTiO_3$ (STO) is the model candidate for exhibiting the perovskite structure ABO_3, most perovskites do no have a perfect perovskite structure, but are slightly distorted within the structure. As bulk material, $La_{2/3}Sr_{1/3}MnO_3$ (LSMO) is rhombohedral (space group R-3c) with lattice parameters a=5.4957 Å, b=5.4957 Å and c=13.3713 Å (ICSD, Collection Code 156020); the angles in pseudocubic representation are α=β=γ=90.26 ° and the pseudocubic lattice constant is 3.87 Å. This distortion is due to the ions of $La_{2/3}$ and $Sr_{1/3}$ not having perfect radii to form the perovskite cube; additionally, the electronic configuration of Mn^{3+} and Mn^{4+} can distort the oxygen octahedron of the perovskite structure.

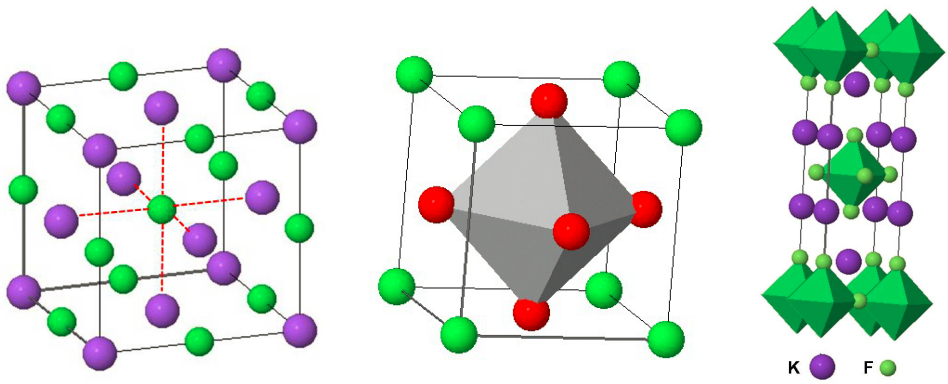

(a) Rock salt structure, space group Fm-3m

(b) Perovskite structure ABO_3, space group Pm-3m

(c) $KNiF_3$ structure, space group I4/mmm

Figure 2.1: Crystal structures used in this work, taken from [15]

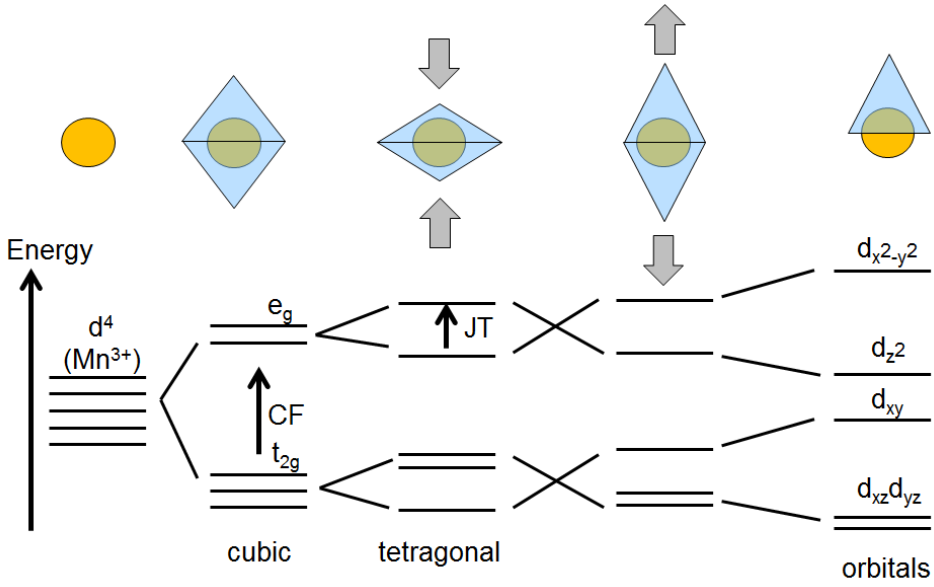

Figure 2.2: Sketch of crystal field (CF) splitting. In the upper part, the local environment of the central cation B (yellow) inside the oxygen octahedra (blue) of the ABO_3 structure is visualized; in the lower part, the according energy level diagrams are drawn. a) free ion and degenerated d orbitals, b) cubic environment and CF splitting, c) vertically compressed cation environment due to Jahn-Teller (JT) contributions, d) horizontally compressed cation environment due to epitaxian strain, e) oxygen vacancy and resulting orbitals; see text for details

A point charge model, which takes the influence of the next neighbors into account as an effect of electric field created by oxygen onto the central cation, is the crystal field theory. This is a generalization of anisotropic charge density distribution around the 3d ions [16]. The interaction of the crystal field multiplet with the spin-orbit coupling gives rise to a local anisotropy for the spin degree of freedom, which is called crystal field anisotropy. The orientation of the 3d orbitals towards the negative oxygen octrahedron corners for $d_{3z^2-r^2}$ and $d_{x^2-y^2}$ and an orientation away from these corners for d_{xy}, d_{yz} and d_{zx} leads to crystal field splitting.

In fig. 2.2 the different models are sketched with the corresponding local environment above. The degenerated 3d band (only cation influence, 2.2a) is splitted by the crystal field (CF) into a t_{2g} band and an e_g band, see fig. 2.2b. In this octahedral configuration, the e_g band is shifted to higher energies. Additional decrease of degeneracy is related to further symmetry reduction like Jahn-Teller distortions (JT, fig. 2.2c) or epitaxial distortions (fig. 2.2c or 2.2d, depending on tensile or compressive strain). Even further splitting can be accomplished via a bigger symmetry reduction such as oxygen defects, see fig. 2.2e.

In $La_{2/3}Sr_{1/3}MnO_3$, 2/3 of all manganese atoms have a Mn^{3+} valence state and therefore [Ar]$3d^4$ electronic configurations with a spin angular momentum S=2 and orbit angular momentum L=2; 1/3 has a Mn^{4+} valence state, therefore [Ar]$3d^3$ electronic configuration with S=3/2 and L=3. This is only valid for pure ionic bonding; if the energy levels split, the 3d orbitals degenerate, therefore L=0, therefore S=J and for the Landé factor g=2.

For Mn^{3+} the electronic configuration is $3d^4$. Following Hund's rules, to maximize the total spin S (first rule), all electron spins are parallel. The ground state has the largest value of total spin angular momentum (second rule), therefore t_{2g} has three electrons, e_g one electron ("high spin state"; S=2). When the crystal field splitting is large enough, it is energetically favorable to be antiparallel to the already existing electron in the t_{2g} orbital double ("lower spin state",; S=1). In the high spin state, one electron occupies the e_g electronic energy band, which corresponds to two degenerate orbital wave functions: $d_{3z^2-r^2}$ or $d_{x^2-y^2}$. This degeneracy can be revoked by a Jahn-Teller distortion of the surrounding local environment. The cooperative Jahn-Teller effect describes the lattice place distortions which lead to a periodic distortion pattern. Here, orbital order (electronic orbitals occupying periodically a crystal) can minimize the interaction. Here, the states are split, e_g as well as t_{2g} [17]. Mn^{3+} degenerates in terms of orbitals, which distorts the crystal, Mn^{4+} with $3d^3$ cannot show a Jahn-Teller distortion.

In $La_{1-x}Sr_xMnO_3$ the wave functions of the Mn-3d orbitals do not overlap directly, the magnetism is conveyed via the oxygen 2p orbitals in fig. 2.2b, which are located between the manganese atoms. The two most prominent exchange mechanisms in LSMO are the superexchange mechansim, which preferably takes place between electrons in the t_{2g} levels of neighboring atoms and which describes a virtual hopping process, and the double exchange mechanism, which takes place between e_g orbitals of neighboring Mn^{3+} and Mn^{4+} atoms and favors ferromagnetic order. Depending on the bonding angle, orbital filling state, metal valencies and doping of the bondings, antiferromagnetic or ferromagnetic orbital order occurs. A detailed description is given by the Goodenough-Kanamori-Andersen rules, see e.g. [18], which can explain the phase diagram for bulk $La_{1-x}Sr_xMnO_3$.

2.1.1 Used materials

Bulk LSMO is paramagnetic above 370 K and ferromagnetic below; at the Fermi level there are only spin-up electrons, it is a half metal [19]. The physical properties are insensitive to small stoichiometric changes; $La_{0.25}Sr_{0.75}MnO_3$ to $La_{0.45}Sr_{0.55}MnO_3$ are tetragonal, metallic and ferromagnetic below T_C (320 .. 370 K) and paramagnetic above. The extreme cases $LaMnO_3$ and $SrMnO_3$ are both antiferromagetic at low temperatures and paramagnetic at room temperature, which can be seen in the phase diagram of [14].

The substrate material STO has a perfect perovskite structure at room temperature (group Pm-3m) with a lattice constant of 3.9056 Å. The melting temperature is 2360 K. It is diamagnetic, paraelectric and therefore electrically isolating as perfect stoichiometric STO; it can become conducting upon doping with oxygen vacancies [20, 21] or Nb [22]. At 105 K STO undergoes a phase transition into a ferrodistortive low temperature phase [23]. $SrTiO_3$ is used as a substrate in (100) orientation. It is chemically compatible with LSMO, it does not react with the deposited layer and therefore no interdiffusion of $SrTiO_3$ with LSMO is expected. Furthermore, $SrTiO_3$ has a cubic structure with a lattice parameter which only deviates 1 % from the $La_{2/3}Sr_{1/3}MnO_3$ bulk lattice parameter. For epitaxial growth of LSMO on STO and thin, non-relaxing layer parameters, the substrate provides the in-plane lattice parameters for the crystalline layer structure. Under the assumption that the epitaxially grown unit cell volume of LSMO is equal to the relaxed one of bulk LSMO, the out-of-plane lattice constant should be c($La_{2/3}Sr_{1/3}MnO_3$)=3.847 Å, a deviation of 6 % to the relaxed LSMO pseudocubic lattice parameter of 3.87 Å.

The perovskite representation of LSMO can be sliced into a $La_{2/3}Sr_{1/3}O$ layer and a MnO_2 layer. In contrast to manganese oxide, LaSrO is not inert. Both, LaO as well as SrO, are hygroscopic at room temperature and humid atmosphere. LaO exists as hexagonal single crystal (as long as it is protected from atmosphere, e.g. cast in synthetic resin). The targeted stoichiometric variations within the LSMO layer are therefore challenging in growth via target-based methods like Pulsed Laser Deposition or Sputter machines. Palgrave et al. [2] needed $La_{2/3}Sr_{1/3}MnO_3$ and SrO targets to produce $(La_{1/2}Sr_{1/2})_4Mn_3O_{10}$; to vary that stoichiometry while keeping the La vs. Sr ratio constant, for each stoichiometry variation a different LSMO target is required.

2.2 Scattering

For high quality samples, a well-defined crystal structure is needed, the existence of which can be determined via scattering methods. Electron, X-ray and neutron beams with wavelength comparable to interatomic distances can be used to determine the atomic ordering inside the crystal.

2.2.1 General scattering

The following discussion is based on the introduction into scattering methods of Th. Brückel [16].

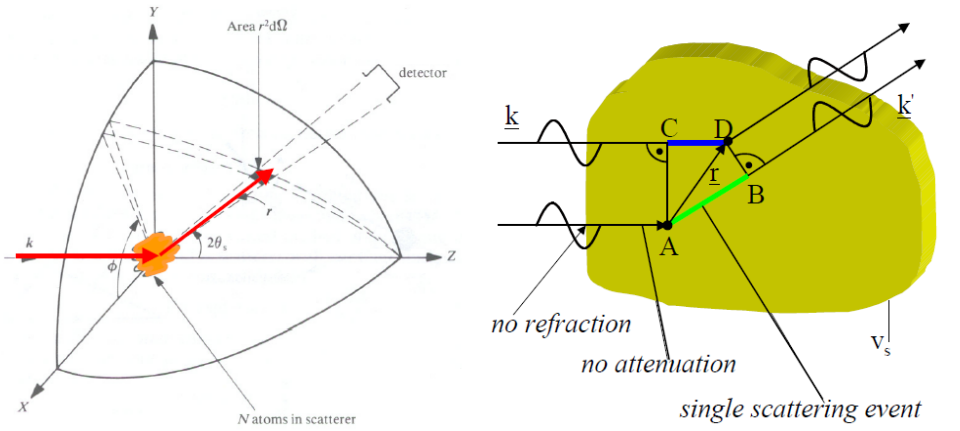

(a) Sketch of scattering geometry, which introduces the parameters needed for the definition of the double-differential scattering cross section

(b) Phase difference of incoming and scattered beam

Figure 2.3: Scattering geometry, taken from [16]

All used methods fulfill the Fraunhofer approach: Source, sample and detector are at large distances so that the at-source and sample-formed spherical waves can be approximated as plane waves. Additionally, the scattering process is assumed to be purely elastic; magnitude of wave factors before and after scattering are identical: $k = |\vec{k}| = |\vec{k'}| = k' = \frac{2\pi}{\lambda}$, where $\vec{k}$ is the wave vector of incoming and $\vec{k'}$ is the wave vector of the outgoing wave.

The scattering vector $\vec{Q}$ with quasiimpulse $\hbar\vec{Q}$ represents the momentum transfer during the scattering process:

$$Q = |\vec{Q}| = |\vec{k'} - \vec{k}| = \sqrt{k^2 + k'^2 - 2kk'cos2\theta} = \frac{4\pi}{\lambda} sin\theta \tag{2.1}$$

To describe the scattering cross section, n' particles per second are scattered into a solid detector angle element dΩ with a scattering angle 2Θ in an energy interval between E' and E'+dE'. This is shown in figure 2.3a.

The double-differential scattering cross section is defined as:

$$\frac{d^2\sigma}{d\Omega dE'} = \frac{n'}{j d\Omega dE'} \tag{2.2}$$

j is the incoming beam flux as function of particles per area and time. Without change of energy during the scattering process, the formula for the differential scattering cross section becomes:

$$\frac{d\sigma}{d\Omega} = \int_0^\infty \frac{d^2\sigma}{d\Omega dE'} dE' \tag{2.3}$$

The so-called total cross section is a measure for the total scattering probability, which is inde-

pendent of energy change and scattering angle:

$$\sigma = \int_0^{4\pi} \frac{d\sigma}{d\Omega} d\Omega \tag{2.4}$$

The scattering density depends on the kind of used rays and interaction of rays with the sample. For *neutrons*, the Fermi pseudo-potential describes the point-shaped scattering at the nucleus at the location $\vec{R}$ via a δ function, in which the scattering length b is the characteristic scattering probability for a definite atom nucleus. Via the point-shaped scattering model the scattering process can be described in line with the Born approximation. The Born approximation describes a single scattering processes of the incident wave, which is assumed to be a planar wave $e^{i\vec{k}\vec{r}}$. It does not take into account multiple scattering, refraction of incoming and outgoing beams or extinction of the primary beam. In figure 2.3b the phase difference between the scattered wave at the origin and at position $\vec{r}$ is given by

$$\Delta\Phi = 2\pi \frac{\overline{AB} - \overline{CD}}{\lambda} = \vec{k}' \cdot \vec{r} - \vec{k} \cdot \vec{r} = \vec{Q} \cdot \vec{r} \tag{2.5}$$

This phase shift is used inside the total scattering amplitude which can be described as (assuming a laterally coherent beam):

$$A = A_0 \int_{V_S} \rho_s(\vec{r}) e^{i\vec{Q}\vec{r}} d^3r \tag{2.6}$$

Here the scattering density $\rho_s(\vec{r})$ is proportional to the scattering amplitude at this position $\vec{r}$. During an experiment, only the intensity $I \approx |A^2|$ can be observed, therefore the phase information is lost.

Additionally, a neutron has a spin 1/2 and therefore a magnetic moment $\vec{\mu}_N$. Therefore the neutron can be scattered inside a material via interaction of electromagnetic fields $\vec{B}$. This leads to

$$V = -\vec{\mu}_N \vec{B} \tag{2.7}$$

Photons interact with the electrons of the outer shells, therefore the photo effect, the Thompson effect (or Compton scattering, resp.), and pair production have to be taken into account for different energies.

2.2.2 Reflectivity

An essential target of characterization of the growth process is the examination of the layer structure. For that, X-ray reflectivity under grazing incidence is suited for because for small incoming angles α_i towards sample surface, X-rays and neutrons are not sensitive to resolve the atomic structure. In this geometry, X-rays are only sensitive to a change in refractive index of layers, e.g. by different elementary composition or by density changes. Analogous to optics of light, refraction and reflection appear at each interface and at the surface. In contrast to optics of light, the refractive index of all materials for X-rays is smaller than 1 [24]. Below the critical angle the total beam is reflected, while starting from the critical angle $\alpha_{c,j} = \arccos(n_1/n_2)$ the reflected part is proportional to the square root to the dispersion δ.

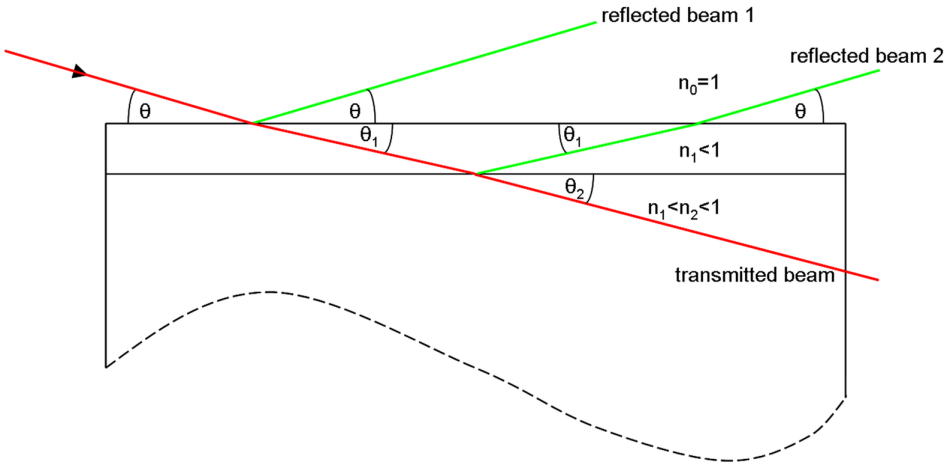

Figure 2.4: Reflection and refraction from a single layer on a substrate; incoming beam in red, reflected beam in green. Taken from [24]

Specular reflectivity occurs at flat surfaces and interfaces. In this process, the beams reflected from different interfaces interfere (see fig. 2.4), so that for periodic structures angle-dependent peaks appear when plotting the incoming angle vs. intensity. The so-called Kiessig fringes display the total layer thickness. While correlated roughness at interfaces can be detected via off-specular scattering ($\alpha_i \neq \alpha_f$), uncorrelated roughness cannot be determined via off-specular reflectometry. Below only the specular reflectivity (incoming angle α_i equals outgoing angle α_f) is discussed. Thus the scattering vector is perpendicularly orientated to the sample surface, in this scattering geometry only laterally averaged information of the sample is accessible.

The complex refraction index of a sample is given by

$$n = 1 - \delta + i\beta \tag{2.8}$$

with refractive index n, dispersion δ, absorption β. For X-rays and electrons, δ and β are proportional to the electron density ρ_j. For neutrons, which scatter at the nucleus, the absorption β=0 and δ=$\frac{\lambda^2}{2\pi}\sum_j b_j\rho_j$, while for photons it is:

$$n = 1 - \frac{\lambda^2 r_0}{2\pi}\sum_j \rho_j(Z_j + f'_j + if''_j) =: 1 - \delta + i\beta \tag{2.9}$$

with electron radius r_0, Z atomic number and f'_j and f''_j correction term for dispersion and absorption near the resonant energy. A very good introduction into this topic can be found at [24].

If an X-ray beam strikes a sample surface under grazing incidence, it is reflected at every change of density. The X-ray beam interacts with electrons and is therefore only senitive onto change of electron density due to different materials. At angles below the critical angle θ_c, the beam is entirely reflected at the sample surface. For larger angles, the beam partially enters the sample and is no longer fully reflected.

To evaluate X-Ray measurements in terms of total layer thickness, surface and interface roughness, the optical matrix formalism according to Parratt [25] is used in both programs GenX and Plot-Script, the latter using the formulas of [26]. These formulas require homogeneous layers and a substrate thick enough, so that no reflection at the back side of the sample takes place:

$$X_j = \frac{R_j}{T_j} = e^{-2ik_{z,j}z_j} \frac{r_{j,j+1} + X_{j+1}e^{2ik_{z,j+1}z_j}}{1 + r_{j,j+1}X_{j+1}e^{2ik_{z,j+1}z_j}} \tag{2.10}$$

Therefore, the ratio of amplitudes of reflected and transmitted wave is given by a recursive formula, for which the Fresnel coefficients $r_{j,j+1}$ and the z component of the wave vector $\vec{k}_j^i$ contribute. The reflected intensity is proportional to the square of the amplitude ratio.

The used model takes laterally correlated roughnesses into account via modified Fresnel coefficients

$$\tilde{r}_{j,j+1} = r_{j,j+1}e^{-2\sigma^2 k_{z,j}k_{z,j+1}} \tag{2.11}$$

with σ beeing the standard deviation of a Gaussian-shaped distribution for the local height. This model was developed for laterally structured metallic MBE samples with correlated roughnesses.

The Parratt formalism requires that roughness values are far below layer thickness values. If roughness and thickness values are in the same order of magnitude, this ends up in discontinuities of the dispersion profile and the process of the refraction index [27].

Therefore, the grown layers must fulfill minimum quality standards before further evaluation is feasible.

2.2.3 Polarized Neutron Reflectometry

Neutrons have a magnetic moment and are thus sensitive to magnetic materials. The incoming neutron beam is polarized by a supermirror. A polarization parallel towards the guide filed is described as "+" antiparallel is marked as "-".

The following two equations describe the scattering process for polarized neutrons using polarized neutron beams:

$$\Psi''_+(\vec{r}) + \left[k^2 - 4\pi b\rho_N + \frac{2m\gamma_n\mu_N}{\hbar^2}B_\parallel\right]\Psi_+(\vec{r}) + \frac{2m\gamma_n\mu_N}{\hbar^2}B_\perp\Psi_-(\vec{r}) = 0 \tag{2.12}$$

$$\Psi''_-(\vec{r}) + \left[k^2 - 4\pi b\rho_N - \frac{2m\gamma_n\mu_N}{\hbar^2}B_\parallel\right]\Psi_-(\vec{r}) + \frac{2m\gamma_n\mu_N}{\hbar^2}B_\perp\Psi_+(\vec{r}) = 0 \tag{2.13}$$

Two different processes take place, the Non-Spin-Flip (NSF) and the Spin-Flip (SF) process. During a spin flip process, the mangetic quantum number S_z of the neutron spin momentum changes sign upon scttering. This can occur for magnetic scattering. Therefore, four channels describe the scattering process: "+ +" is the NSF process with spins parallel to the external magnetic field, "- -" describes the NSF process with spins antiparallel to the field before and after scattering at the sample. The SF channels "+ -" and "- +" only show a signal if the magnetic moments of the sample are not perfectly parallel to the applied field.

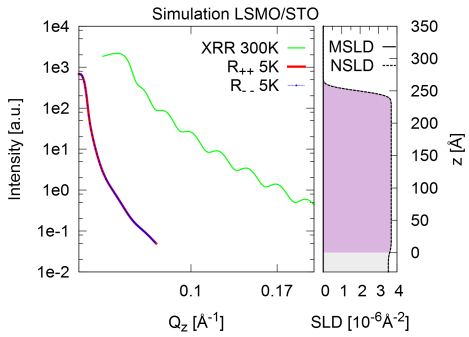

(a) Simulation of LSMO/STO without magnetic contribution: No difference in neutron nuclear SLD between LSMO and STO

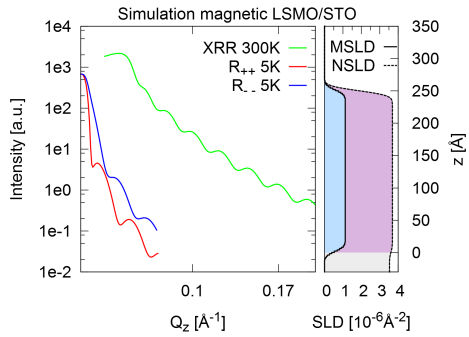

(b) Simulation of LSMO/STO with magnetic contribution of ferromagnetic LSMO film

Figure 2.5: Simulated reflectivities of the LSMO/STO system: XRR (green) gives total layer thickness and roughness, PNR, R_+ (red) and PNR, R_- (blue) contribute information magnetic layer thickness and depth-dependent Magnetic Scattering Length Density (MSLD). The for the simulations used Nuclear Scattering Length Density (NSLD) is displayed next to the simulated reflectivities (grey: STO, purple: nuclear LSMO, blue: magnetic LSMO)

All measurements performed for this thesis were taken on ferromagnetic samples in saturation, therefore there is no signal in the spin-flip channels. The neutron beam was thus polarized but not analyzed, resulting in shorter counting times for the "+" and "-" channel. Via measuring the "+" and the "-" channel, the magnetic and nuclear scattering can be separated and a depth-sensitive information about the magnetic structure of the sample can be obtained like in fig. 2.5.

2.2.4 Diffraction

While reflection probes changes in density, diffraction describes the process when a beam is elastically scattered at the length scale of atomic periodic structures. The Bragg law describes the condition for the constructive interference:

$$n * \lambda = 2d * sin\theta \tag{2.14}$$

with λ wavelength, d interplanar spacing and θ outgoing angle/2. A lattice point "uvw" is at the position $u\vec{a}_1$+$v\vec{a}_2$+$w\vec{a}_3$ with basis vectors $\vec{a}_1$, $\vec{a}_2$, and $\vec{a}_3$. The first plane from the origin of a set of lattice planes makes intercepts a/h, b/k, c/l on the X, Y, Z axes [28]. With n being an integer, the Miller indices (hkl) are therefore defined by

$$\frac{hx}{a} + \frac{ky}{b} + \frac{lz}{c} = n \tag{2.15}$$

A set of lattice planes (hkl) is separated by a characteristic interplanar spacing d(hkl). For cubic crystals with lattice constant a, the spacing d between adjacent (hkl) lattice planes is

Table 2.1: STO powder pattern peaks for X-ray Cu K_{α_1} source, simulated via [30]

H	K	L	2theta	intensity
1	0	0	22.75	39.2
1	1	0	32.40	1000.0
1	1	1	39.96	199.4
2	0	0	46.47	395.2
2	1	0	52.35	31.3
2	1	1	57.79	378.7
2	2	0	67.82	216.7
3	0	0	72.56	4.0
2	2	1	72.56	16.0
3	1	0	77.18	162.0
3	1	1	81.72	53.9
2	2	2	86.21	70.8
3	2	0	90.67	11.5
3	2	1	95.13	214.0
4	0	0	104.19	39.8
4	1	0	108.84	11.2
3	2	2	108.84	11.2
3	3	0	113.62	50.9
4	1	1	113.62	101.8

$$d_{hkl} = \frac{a}{\sqrt{h^2 + k^2 + l^2}} \tag{2.16}$$

In the LSMO/STO system, the main peak positions at angle θ provide the out-of-plane lattice parameters c:

$$c = \frac{n * \lambda}{2sin\theta} \tag{2.17}$$

In pure out-of-plane geometry, the distance of fringes with i,j fringe orders give the total crystalline layer thickness d [29]:

$$d = \frac{(i-j)\lambda}{2sin(\theta_i' - \theta_j')} \tag{2.18}$$

with ω' 1/2 outgoing angle.

If $SrTiO_3$ (space group Pm-3m) were without the oxygen atoms and additionally Sr and Ti were identical atoms, that structure would be body-centered, therefore the (h+k+l=odd) reflections were forbidden. Instead, in the Pm-3m structure the odd reflections still exist, but their intensity is drastically reduced compared to the even ones. Via ICSD [30], the powder pattern for STO was simulated, to compare more quantitatively the even vs. odd reflections, see tab. 2.1. With respect to these values, the pure out-of-plane measurements around one substrate reflex are performed at the (0 0 2) STO reflex to determine the out-of-plane lattice parameter while the intensity to background ratio is maximized.

Chapter 3

Experimental methods and setups

Thin oxide films were produced and investigated. The methods used for this thesis are shown in fig. 3.1. The sample quality had to be evaluated and routines had to be developed for these evaluations. In the following, the most important methods are discussed.

To produce a sample, the Oxide Molecular Beam Epitaxy (MBE) setup including Quartz Crystal Balance (QCB), Reflection High-Energy Electron Diffraction (RHEED), Low Energy Electron Diffraction (LEED) and Auger Electron Spectroscopy (AES) was utilized. The resultant data are visualized via Gnuplot and Python. To check sample quality, X-Ray Reflectivity (XRR) and X-Ray Diffraction (XRD) are applied and data interpretation is performed via Plot-Script [31]. To confirm the stoichiometry, samples are investigated by Rutherford Backscattering Spectrometry (RBS). To determine the magnetic characteristics, samples are measured via Magnetic Properties Measurement Setup (MPMS). The depth-dependent magnetization behavior is investigated by Polarized Neutron Reflectometry (PNR) and evaluated via GenX. Surface topography is measured via SEM; cross-sections of samples showed the local structure and stoichiometry via Transmission Electron Microscopy (TEM) and Energy-Dispersive X-ray spectroscopy (EDX).

3.1 The Oxide Molecular Beam Epitaxy (MBE) setup

All samples in this work were produced via a DCA Instruments M600 MBE system [32], the Oxide MBE setup of JCNS@MLZ. Here, the used components are described; a full description of the instrument can be found in [6].

The MBE setup is displayed in fig. 3.2 and consists of three chambers, separated by UHV gate valves. The **load lock** (LL) chamber is used to introduce samples into the UHV and for storage due to its transfer trolley with 12 sample holders. The load lock has a base pressure of $2*10^{-8}$ Torr and can be heated up to 200 °C to remove water contamination due to air humidity.

The **buffer line** (fig. 3.2a, BL) is the transfer area between load lock and preparation chamber and is equipped with two spheres to treat substrates and perform quality control before and after sample preparation. In the outer sphere, an Auger Electron Spectroscopy (AES) device is mounted. The AES sample holder can treat samples up to 1000 °C. The sphere next to the transfer rod, towards the preparation chamber, contains a Low Energy Electron Diffraction (LEED) setup. It is a commercially available SPECS setup, containing the Reverse View LEED

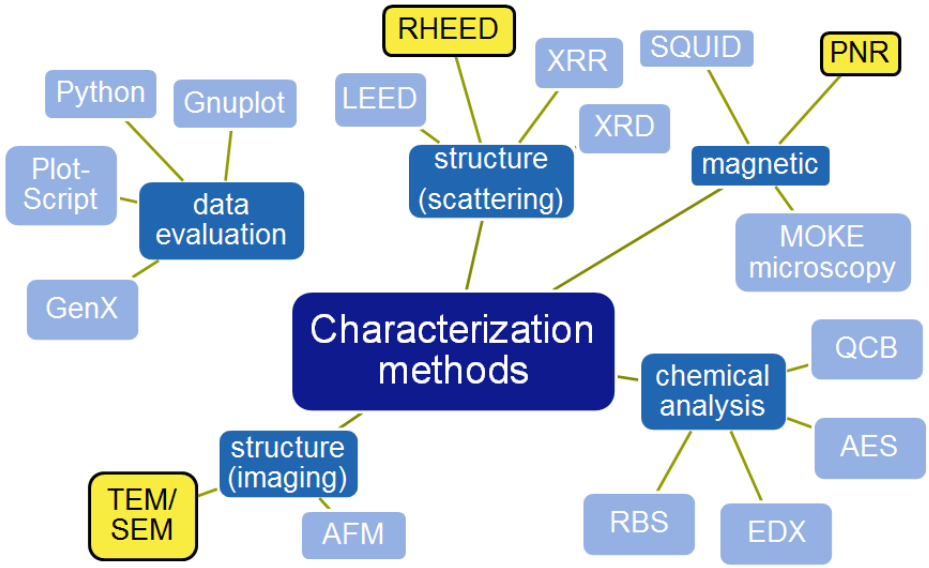

Figure 3.1: Tools employed to investigate samples; see text for definition of the acronyms. The most frequently used methods are marked by yellow background

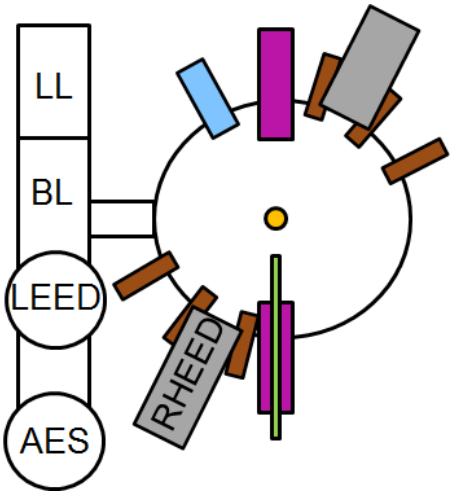

(a) Sketch: top view of MBE setup including buffer line (BL) and load lock (LL). Brown rectangles symbolize effusion cells, blue: oxygen plasma source, green: quartz crystal balance, purple: e-guns, yellow: sample holder, grey: RHEED setup

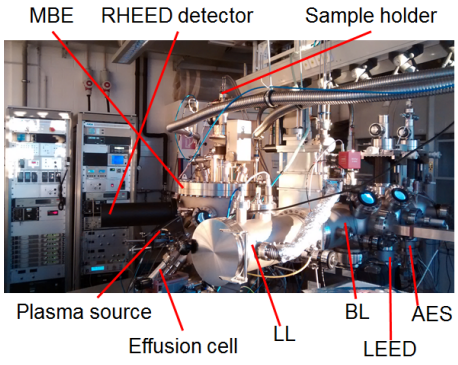

(b) Photo of MBE setup; label "MBE" pointing towards MBE preparation chamber

Figure 3.2: MBE setup

Optics ErLEED 100/150 [33]. For LEED and RHEED data aquisition, the kSA400 software (version 5.30, [34]) from k-Spaces Associates Inc. was used. The base pressure is $2*10^{-10}$ Torr, realized via a "Gamma Vacuum 300l ion pump" [35].

The **preparation chamber** is attached towards the buffer line. It is equipped with 6 effusion cells (in fig. 3.2a brown rectangles), 2 electron guns, each with 4 crucibles (violet rectangle) and an oxygen plasma source, model HD25RF atom, Oxford Applied Research [36] (blue rectangle). For the samples described in this work, the electron guns were not used. The base pressure is 10^{-10} Torr, provided by a CTI cryogenics cryo pump, and Pfeiffer 500 l/s turbo pump. During thin oxide film preparation, the pressure is at 10^{-5} Torr. A typical growth rate is 15 nm/h. The RHEED setup (grey rectangle without description: RHEED camera) is attached at the MBE chamber. It is a Staib Instruments RHEED 20 setup with 20 kV maximum voltage and 1.8 A maximum current [37]. The fluorescent screen is monitored by the kSA setup and software mentioned for LEED.

The water cooling system cools the quartz crystal balances (fig. 3.2a, green rectangle) and the effusion cells. Additionally, for effusion cell temperatures or substrate holder temperatures above 500 °C (or to get a better base pressure for thin metal film preparation) liquid nitrogen is filled into a cryopanel working as an adsorption pump.

With the used Oxide MBE setup, substrate temperatures up to 1000 °C are possible. The mentioned temperature values are always measured with the same thermocouple device (s-type). Due to the transparency of STO at high temperatures, the STO temperatures were never verified with a pyrometer.

The sample holder (orange circle in fig. 3.2a) consists of an SiC Heater, the temperature-read out is performed via an S-type Pt/Rh thermocouple, controlled via Eurotherm PID 3508 controller [38] and TDK lambda DC power supply. The here used substrate holder are made of Molybdenum and can hold up to two samples. For samples prepared as twin samples, the letter "a" or "b" indicates the existence of twin samples, with "a" always 10mm x 10mm and "b always 5mm x 5mm.

All effusion cells point towards the focus point of the MBE setup. To reach the required growth rates for LSMO, the corresponding temperatures of the effusion cells equipped with Sr, Mn, and La were approximately 500 °C, 850 °C, and 1600 °C. For La, a high-temperature effusion cell of Createc was used which is specified for use at operation temperatures up to 2300 °C. Different crucibles for different materials were used; for Sr and Mn, Pyrolytic Boron Nitride (PBN) crucibles were used, for La, the crucible was made of Ta due to the far higher operation temperature, and for Ti, a special crucible of DCA was used, which is part of a US patent (No. US20090301390 A1).

The purities of the materials put into the effusion cells are in the range between 99.995 % (for Ti) and 99% (for Sr); the oxygen used for oxygen plasma was bought with a purity of 99.995 %. Additionally, Sr is stored in oil and has to be cleaned in hexane before introduction into the UHV chamber. To ensure that there is no carbon contamination, AES scans were performed after preparation of thin films containing Sr; no peak was found around the typical carbon energy of 272 eV. Additionally, within the RBS scans no contamination was revealed above the analysis limit of 0.008 %. With a Residual Gas Analyzer (*RGA*) the composition of the residual gas atoms was constantly monitored.

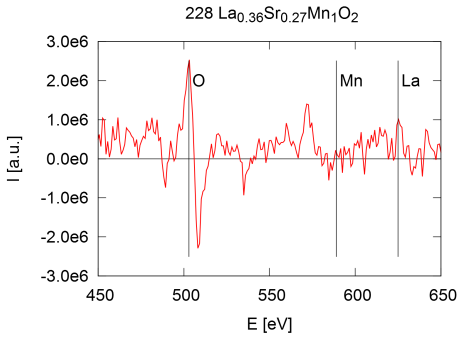

Figure 3.3: AES spectrum of sample 228: Indeterminable La/Mn ratio

3.1.1 Quartz crystal balance (QCB)

Before sample preparation and during rate calibration of the effusion cells, the main quartz crystal balance is positioned at the focus point. Changes of the Eigenfrequency of the quartz crystal, measured in Hz/s (window "Frequency trend"), are monitored vs. time (window "Rate trend"). After the change of monitored effusion cells, the quartz crystal balance needs approx. 20 minutes to thermally stabilize. Additionally, small changes in effusion cell temperatures need several minutes to show a constant new rate trend.

3.2 Auger Electron Spectroscopy (AES)

For Auger Electron Spectroscopy (AES), electrons are accelerated onto the sample, and element-specific energy-dependent scattering of sample Auger electrons is detected. Due to the affinity of electrons to multiple scattering inside a sample, the method only provides one with an information depth of less than 10 surface-near atomic layers. Hence this is a true surface tool.

While AES is a powerful tool for the determination of clean surfaces and layer thickness for metals, for the materials used in this thesis a few restrictions make it less useful. With fully oxidized samples, often electrostatic charge effects are detected instead of a stoichiometric-specific spectrum. For non-oxygen-saturated samples, the most prominent peak by far arises from the remaining oxygen signal. According to the relative Auger sensitivities of the elements table in the standard handbook [39], the element-specific peaks for La and Sr are more than one order of magnitude less prominent than for O or Ti. It should be noted that Sr energies of 65-110 eV and La energies at 59-95 eV are in the rising area of the AES signal, barely detectable in comparison with the O and Mn signal and therefore not ideal candidates for quantification just due to their energy values.

In fig. 3.3 an example for an Auger electron spectrum is shown. RBS revealed that sample 228 has a stoichiometric composition of $La_{0.36}Sr_{0.27}Mn_1O_2$; the double the amount of O vs. Mn was not quantifiable via AES, nor the La peak at all visible. Therefore for LSMO, the AES setup was not used to determine the exact stoichiometry.

3.3 Low Energy Electron Diffraction (LEED)

LEED is diffraction backscattering with electron diffraction. Electrons with energies between 25 eV and 300 eV are used to probe the crystalline structure of the sample surface. Like at AES, only the first unit cells near to the surface are probed due to multiple electron scattering inside the sample. The surface structure of $SrTiO_3$ was investigated intensively ([40] and references within).

A general problem appears for sample holders containing 2 samples (sample identification number ending on "a" or "b"). The detected spots were broadened due to the substrate surface orientation error bar of 0.3 °, leading to misorientation of the two investigated samples up to 0.6 °. Still, the important information (existence of peaks/starting energy for charging effects) can be gained, therefore the average image of 2 samples was taken.

3.4 Reflection High-Energy Electron Diffraction (RHEED)

RHEED is used to observe the surface structure and to distinguish different crystal conditions (i.e. amorphous, polycrystalline, crystalline) by grazing incidence small angle electron scattering. At the sample surface, the 3D reciprocal space points transform into continuous rods which are normal to the surface. The Ewald sphere crosses all rods contained in the projection of this sphere onto the surface. The spots observed on the RHEED detector are a projection of this Ewald sphere on a plane parallel to the surface [41]. The shape of the detected rings, stripes or dots (or no signal at all) is used to qualify the crystalline quality of the sample surface.

The electron beam hits the sample under an incident angle of 1.5°. The energy is 15 keV with a wavelength of 0.81 Å. With an area detector the grazing incident angle diffraction (GID) spots can be detected; for $SrTiO_3$ (1 0 0) with a lattice constant of 3.91 Å and Si (1 0 0) (5 Å), zero-order and minus first-order HOLZ (higher order Laue zone, explained in section 3.4) are visible.

Introduction of RHEED indexing

For further details about RHEED pattern indexing, see Peng et al. [42]. For the correct way to use brackets please refer to G. Heger, [43]. A good real space lattice visualization is shown in the supplementary material of Gustafson et al. [44].

During RHEED data acquisition, the STO substrate is oriented either so that the edge of it is parallel to the electron beam, which leads to a [1 0 0] direction of the incoming beam; the second preferred orientation is a tilt of 45° between edge of substrate and electron beam direction and called [1 1 0], see fig. 3.4a. Figure 3.4a shows the (0 0 1) lattice plane, parallel to the real space $\vec{a}_3$ axis. The incoming electron has a grazing incidence angle and is therefore nearly parallel to that lattice plane.

Due to the grazing incidence geometry, the electrons are scattered at the 0 0 0 position. Therefore, for the [1 0 0] orientation, the Laue zones are traces of (1 0 0) lattice planes, where the zero-order Laue zone (ZOLZ) crosses the 0 x 0 lattice points, the minus first-order higher-order

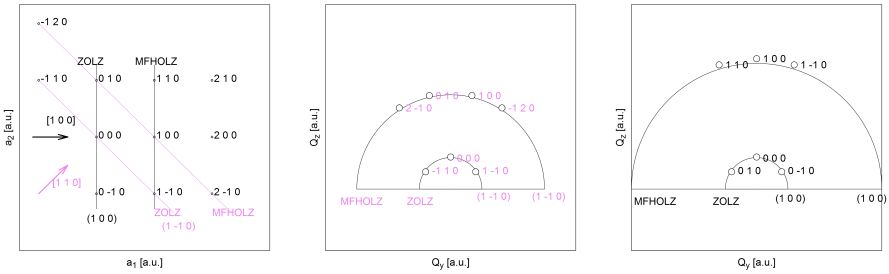

(a) real space lattice points uvw; traces of lattice planes (hkl); ($\vec{a}_1$, $\vec{a}_2$ in-plane basic vectors of unit cell; $\vec{a}$=u$\vec{a}_1$+v$\vec{a}_2$+w$\vec{a}_3$ with u,v,w integers)

(b) Corresponding RHEED detector image for [110] orientation of substrate

(c) Corresponding RHEED detector image for [100] orientation of substrate

Figure 3.4: RHEED indexing

Laue zone (MFHOLZ) crosses the 1 x 0 positions, the minus second-order higher-order Laue zone (MSHOLZ) crosses the 2 x 0 positions and so on. For a [1 1 0] orientation of electron beam vs. substrate, the Laue zones are traces of (1 -1 0) lattice planes. The ZOLZ is at x -x 0 positions, the MFHOLZ is at 1+x -x 0 positions.

In the RHEED detector image, the ZOLZ and MFHOLZ is visible for [1 0 0] and for [1 1 0] direction. In fig. 3.4b and fig. 3.4c, lattice points of fig. 3.4a are displayed to provide with a broad, basic explanation for the indexing of the RHEED spots. While in fig. 3.4b as in fig. 3.4c the specular spot is at the identical position in terms of pixel of detector, the 0 1 0 position is for [1 1 0] at MFHOLZ and for [1 0 0] at ZOLZ.

3.4.1 RHEED Intensity Oscillations

Neave et al. [45] showed that the period of the RHEED intensity oscillation matches the growth of a single GaAs, Ga_xAl_{1-x} and Ge single layer. They introduced the real space representation of formation of a single complete layer; at maximum intensity, the surface is a flat, complete layer. This flat surface is roughened by a few atoms until half of the surface is covered with atoms of the next layer; now the RHEED minimum intensity is given due to the maximum roughness. With additional atoms filling the gaps and completing the layer, the intensity rises again.

Schlom et al. [46] reported RHEED intensity oscillations for perovskite-type structures. Haeni et al. [47], utilized RHEED intensity oscillations for composition control in shuttered deposition. While initially RHEED intensity oscillations were observed during growth via MBE, for PLD setups RHEED was not available due to the high oxygen pressure of up to 0.3 mbar. Klein et al. [48] overcame that problem by differential pumping; another approach is to reduce the pressure to 10^{-5}Torr and therefore call it "Laser-MBE", as presented by Mercey et al. [49].

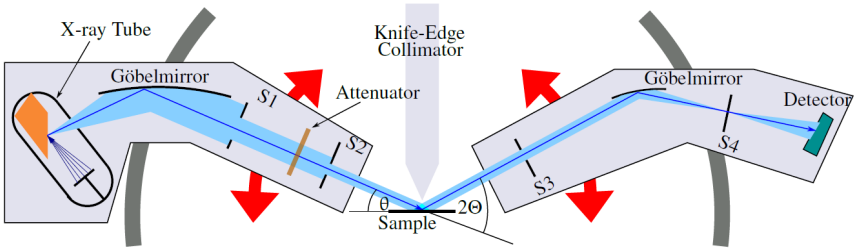

Figure 3.5: XRR sketch, taken from [51]

Table 3.1: X-ray devices used for this work

Institute location	WMI Garching	Neutron Optics MLZ, Garching	Materials Lab HZG, Garching	JCNS FZ Jülich
X-ray device	Bruker Advanced	Bruker Advanced	Panalytical	Bruker Discover
Monochromator	yes	no	no	yes/no

After sample preparation, the RHEED intensity always increases. This was observed already in the first paper and is associated with the conclusion that the onset of growth involves surface roughening [45, 50].

3.5 X-Ray Reflectivity (XRR)

Layer thicknesses and interface as well as surface roughnesses can be determined via X-ray reflectivity (XRR). The layer thickness can be compared with reflection high-energy electron diffraction oscillations to check the in-situ measurements. Additionally, the stoichiometry can be verified via determination of the scattering length density.

4 different setups were used, all utilizing a copper X-ray source with a characteristic wavelength of $Cu_{K\alpha_1}$=1.54055 Å and $Cu_{K\alpha_2}$=1.54438 Å, respectively, and all using the components in fig. 3.5. $Cu_{K\beta}$=1.39221 Å and other wavelengths as well as the major part of the Bremsstrahlung are suppressed by a Göbel mirror. Measurements were performed contingent upon availability of the used experiments in table 3.1.

3.6 X-Ray Diffraction (XRD)

X-ray diffraction experiments can determine atomic parameters like lattice constants of layer and substrate unit cells. General information on the sample quality such as epitaxial growth can be determined.

For all samples grown onto STO, the out-of-plane parameter and the crystalline layer thickness were measured via a (0 0 l) scan around the (0 0 2) substrate peak. A longer scan from (0 0 0) to (0 0 4) was performed at a few samples to check the absence of additional layer peaks indicating no additional crystallographic phase, see e.g. fig. 8.3 (p. 96). This can be performed

by a monochromatic X-ray reflectometer under high angles and was investigated in Jülich and at WMI in Garching. For diffraction, the scattering vector Q is no longer oriented towards normal of sample surface like for XRR, but towards the orientation of the crystal structure of the substrate. Due to the cubic crystal structure of STO, a simple θ-2θ scan from θ=21°to 25°can be converted into a scan around (0 0 2) and the averaged out-of-plane lattice parameter and the crystal layer thickness can be determined within a few minutes.

The crystalline layer thickness determined via XRD is less than 2 nm (2 to 5 atom layers) smaller than the total layer thickness measured via XRR, see e.g. fig. 5.6 (p. 54). This is due to the reconstructed surface, seen via LEED, which no longer has the crystal structure of the layer below.

3.7 Rutherford Backscattering Spectrometry (RBS)

To determine the layer stoichiometry, Rutherford Backscattering Spectrometry (RBS) measurements were performed.

A He ion beam of 1.4 MeV is accelerated onto the sample, the energy of the backscattered (θ=170 °) ions is detected via a silicon detector. The incoming He ion with mass m and energy E_0 is scattered elastically at an atomic nucleus of mass M. The kinematical factor k is the factor of final and incoming energy of the He ion [52]:

$$k = \frac{E_1}{E_0} = \left(\frac{\sqrt{M^2 - m^2 sin^2\theta} + m\, cos\theta}{M + m} \right)^2 \tag{3.1}$$

When the scattering takes place at the depth x inside the top few 100 nm of the sample, the difference of incoming and final energy is given as ΔE=$[S] * x$ with $[S]$ being the energy and geometry dependent energy loss factor.

The Rutherford differential scattering cross section $\frac{d\sigma}{d\Omega}$ describes the probability of a scattering process per area and time and is proportional to the squared target atomic number Z^2. Therefore the accuracy of stoichiometric information is better than 0.1 % for La, Sr and Mn; for oxygen, the RBS errorbar with 5% is relatively big [52].

3.8 Superconducting QUantum Interference Device (SQUID)

The magnetic characterization was performed with a Quantum Design MPMS-7 SQUID magnetometer, with the maximum available field of 7 T. The Superconducting QUantum Interference Device (SQUID) consists of a superconducting coil and 2 Josephson contacts, through which Cooper pairs can tunnel. For all measurements, the reciprocating sample orientation (RSO) option was used moving the sample sinusoidally through the SQUID measurement coils with a frequency of 0.5 Hz to 4 Hz. The sample (5x5mm^2) is mounted in a straw like described in [51] to provide a homogeneous diamagnetic background, which is invisible due to the RSO technique.

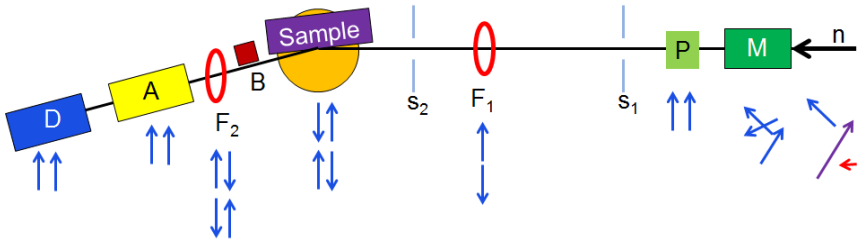

Figure 3.6: Components of a polarized neutron reflectometer: The neutron beam passes a mochochromatizer (dark green), a polarizer (light green), 2 slits (s_1 and s_2, a flipper (red circle), the sample stage (orange) including magnet, cryostat and sample (violet), a beamstop (red rectangle), a second flipper (red circle), an analyzer and is stopped by the detector (blue rectangle). For details, see text.

At constant temperature, the sample is magnetized via a magnetic field and the magnetic moment of the sample is detected. This gives rise to a hysteresis measurement M(H). Magnetic phase transitions are investigated at constant field varying the temperature, resulting in a M(T).

Due to the expected pure ferromagnetic signal of the samples, in a typical measurement only the field-cooled (FC) curve is measured. To determine the Curie temperature of the LSMO films, the field inside the SQUID is set below 0.1 Oe via fluxgate. After that, the sample is mounted at 100 Oe and room temperature, to then measure in FC mode from 370 K to 250 K. For a few samples, the measurement was performed down to 5 K.

PNR measurements were planned to be performed on ferromagnetic saturated samples. As pre-characterization for these PNR measurements, field-dependent measurements were performed at 300 K and 5 K to determine the saturation field. The range of applied field was ± 0.5 T for ± 300 K measurements and ± 1.5 T for 5 K measurements.

3.9 Polarized Neutron Reflectometry (PNR) beamlines

Via Polarized Neutron Reflectometry (PNR), the individual magnetic profile of the thin LSMO films is investigated. The neutron beam arrives at the beamline as polychromatic unpolarized beam (different colored arrows in fig. 3.6). To achieve a monochromatic beam, at the beamline TREFF@MLZ [53] the beam is scattered a pyrolytic graphite crystal with an incoming angle of 45 °. Due to an optimized neutron intrument density, the beam is scattered at a second pyrolytic graphite crystal, again with an incoming angle of 45 °, leading to a wavelength of 4.73 Å with a wavelength spread $\frac{\Delta\lambda}{\lambda}$ of 1.5 %. Between the two graphite crystals, a block of Be powder (T_{Be} below 80 K) eliminates wavelengths of higher order (4.73/2 Å, 4.73/3 Å, ...). After that, a supermirror can be moved inside the beam to polarize the neutrons (all arrows pointing in the same direction in fig. 3.6). As far away as possible from the sample, the first slit is positioned; before the sample stage, the second slit is mounted. Between the two slits, a flipper can flip the magnetic moment of the polarized neutrons (second line of arrows: Either flipper flips magnetic moment of all neutrons or flipper does not flip any magnetic moment). At the sample, neutrons are reflected and, depending on the sample properties, flipped. The sample stage (orange circle

in fig. 3.6) can translate and rotate the sample. Additionally, for the here performed measurements, a cryostate and a magnet were used to perform measurements at 5 K and 0.7 T. After the sample stage the direct beam is blocked by a beamstop to decrease the resulting background inside the detector. A flipper can flip the neutron beam. The analyzer (yellow rectangle in fig. 3.6) consists of a stack of supermirrors parallel to the scattering plane[53]; only spin-up neutrons can reach the detector (blue rectangle).

Measurements were performed at three different polarized neutron reflectometers, MR@SNS [54], TREFF@MLZ, and MARIA@MLZ [55]. At TREFF, the neutrons produced by a reactor are monochromatized by two pyrolytic graphite monochromators. This decreases the neutron intensity; measurements performed at MARIA or MR in a few hours take up to a few days at TREFF. Additionally, the direct-beam-to-background is two orders of magnitude lower at TREFF than at MARIA and MR.

At MARIA, the wavelength of the incoming neutrons is given by a velocity selector, leading to a wavelength spread $\frac{\Delta\lambda}{\lambda}$ of 10 % and a very high intensity. Instead of a flipper and a supermirror-based analyzer, MARIA is suited with a He3 analyzer. The magnet dedicated for the usage at MARIA was used at 1.2 T.

MR is operating in TOF mode utilizing the spallation source neutrons of SNS. Neutron flux and the direct beam to background signal is comparable to the one of MARIA. The magnet was used at 1.2 T, too.

3.10 Scanning Electron Microscopy (SEM), Scanning Transmission Electron Microscopy (STEM) and Energy-Dispersive X-ray spectroscopy (EDX)

Scanning Electron Microscopy (SEM) provides information about the surface topography utilizing low energy secondary electrons which are emitted from the surface. For Scanning Transmission Electron Microscopy (STEM), an electron beam is focused on a sample of preferably less than 100 nm thickness. The transmitted electrons are detected and registered over a selected range of diffraction angles, and the STEM image is formed by scanning the focussed beam over the sample. As a secondary process of the inelastic interaction between the incident high-energy electrons and the sample material, X-rays are emitted at element specific energies (recombination emission). Energy dispersive X-ray spectroscopy (EDX) provides thus access to chemical information in SEM and TEM setups. Introductions into these methods are given by Thomas et al.[56] and Williams et al. [57].

For Scanning Transmission Electron Microscopy (STEM) images, samples have to be prepared in form of very thin foils to be sufficiently electron transparent. A Focused Ion Beam (FIB) setup (FEI Helios Nanolab 400, [58]) was utilized to extract a cross-section, and Ar-ion post thinning was performed via a Baltec RES 120 [59]. During the FIB preparation, a 40 nm thin Au layer was sputtered onto the sample surface in order to enhance the surface conductivity and to avoid charging during the subsequent ion deposition processes. A 10 μm long Pt-C stripe was coated on top of the Au layer selecting the area for the extraction of the thin foil, as displayed in fig. 8.1a (p. 94). Sample material left and right of this stripe were removed by

a focussed Ga ion beam, leaving a standing cross-section lamella of a few 100 nm thickness. The lamella was attached to a liftout holder by sputtering Pt before the remaining connections between the Lamella and the rest of the sample were removed. The detached lamella was subsequently attached to a copper Omniprobe TEM-grid (Oxford Instruments, UK [60]), which can be mounted to a TEM holder. A top-view image of the Pt stripe is shown in fig. 8.1a (p. 94), a cross-section of the different layers in fig. 7.6 (p. 84).

SEM images as shown in fig. 8.1a have been recorded with the FEI Helios Nanlab system used for the TEM sample preparation. STEM images were acquired with two different instruments. Medium resolution STEM and the EDX analysis was performed with an FEI Tecnai G20 (Fei Company, Eindhoven, The Netherlands [61]) at 200 kV accelerating voltage essentially to control the success of the preparation process and to acquire information about sample defects. High-resolution STEM images have been recorded with an FEI Titan 80-300 instrument [62] at 300 kV accelerating voltage. The Titan microscope is equipped with a corrector for the strong spherical aberration (CS) of the illumination system allowing to generate electron probes of around 1 Å diameter, which essentially determines the achievable resolution of the STEM. The SEM, STEM and EDX investigations have been performed by the Ernst Ruska-Centre for Microscopy and Spectroscopy with Electrons (Forschungszentrum Jülich GmbH, Jülich, Germany).

In both STEM setups annular detectors were applied to record scattered electron intensities within angles above 80 mrad. This high-angle annular dark-field (HAADF) STEM scattering setup provides contrast proportional to the atomic number of the material traversed by the focussed electron probe, enabling so-called Z-contrast imaging [63]. By this way it is possible to distinguish the A- and B-site columns of a perovskite structure in a low-index zone axis orientation of the crystal, such as $_{38}$Sr and $_{22}$Ti in the substrate, and $_{57}$La and $_{25}$Mn in the deposited film. Likewise, the A-site columns containing $_{57}$La in the LSMO film should produce a much higher intensity than the respective $_{38}$Sr columns in the substrate. The intensity generated by the pure oxygen columns in the [100] orientation of the cubic perovskite structure is too low to be distinguished from the electron counting noise and is thus not expected to appear in the high-resolution images.

3.11 Atomic Force Microscopy (AFM)

Atomic Force Microscopy (AFM) is a scanning probe microscopy technique which can resolve features as small as an atomic lattice. The images in this work were produced in tapping mode: The tip tipped onto the surface and scanned an area in the nm^2 to μm^2 range. The AFM measurements were performed at a Agilent 5500 SPM [64]. Patrick Schöffmann described all used procedures and parameters in detail in his bachelor thesis [65].

Chapter 4

Preparation

4.1 Typical thin film growth procedure

In order to give information about the critical parameters for growing LSMO thin films, first the typical way of producing them is discussed.

Freshly filled effusion cells are very slowly heated over a few days towards the last used temperatures. Afterwards, for reaching a constant rate, the temperature is slightly adjusted, the quartz crystal balance rates are monitored intensively for a few additional days. In total, this procedure takes up two weeks after a refill (and therefore break of UHV) and at least one week after heating up the effusion cells from 500 °C again (the maximum effusion cell temperature for non-filled liquid nitrogen shielding). Both possibilities of rate stabilization, output control and temperature control, were tested in terms of usability. Because the output control (tunable 0.1 %) provides a larger errorbar onto the rates measured via quartz crystal balance, a stable temperature value adjusted towards the perfect rate every day was found to provide reproducible sample quality. The rate values start to stabilize after a complete melting. The rates rise at constant temperature due to lower filling level of the effusion cell crucibles; the difference from one day to the next is in range of approx. 5 °C to 15 °C. Additionally, the rates depend on the oxygen flow while the effusion cells are in the range of desired rates. The careful, slow heating towards the final growth rates is key to the reproducibility of sample quality. Before growth, the effusion cell rates are calibrated via quartz crystal balance until they show for minimum 30 minutes the targeted element-specific rates. All used parameters are listed in tab. 4.2 (p. 41).

After rate calibration, the quartz monitor head is moved out of the MBE center; during sample preparation, it is no longer used to monitor the rates. The main shutter is opened and the sample holder is moved down towards the focus point. The oxygen supply is opened and the oxygen plasma is ramped up to 250 W forwarded power and 0 W reflected power.

The thin film growth process itself can be divided into three parts: In the first part (ramping up and stabilization), the effusion cells are prepared to be ready to deposit material but still did not deposit anything onto the substrate, the substrate temperature is increased to reach the growth temperature and the oxygen plasma source is providing oxygen plasma onto the substrate.

The second part (sample growth) describes the time span with a constant substrate temperature at the growth temperature, while the oxygen plasma source is providing oxygen plasma onto the substrate, and the effusion cell material is deposited.

The third part (cooling down) is defined by the start of the cooling down ramping procedure, in which the substrate temperature is decreased at a constant rate, the oxygen plasma source is still providing oxygen plasma onto the substrate, and no further effusion cell material is deposited.

For all samples discussed in this work, the first and the third parts are identical: In the first part $SrTiO_3$ is heated towards 900 °C. The UHV conditions inside the chamber are changed by the oxygen plasma source which is directed onto the substrate and transforms the chamber pressure towards 10^{-5} Torr. This leads to a fully oxygen saturated substrate in contrast to oxygen vacancies for heat treatment in vacuum, see fig. C.5b and C.5c (p. 152) with additionally available oxygen plasma.

In the third part, the sample is ramped down from 900 °C to 50 °C with 20 °C/minute. At 50 °C, the oxygen plasma source is turned off, the oxygen supply is closed and the chamber pressure turns from 10^{-5} Torr to 10^{-8} Torr within minutes.

In the second part, the layer material is deposited at a rate of one perovskite unit cell per one minute and in a total deposition time of minimum 90 minutes. Before reaching the substrate surface, the evaporated effusion cell material crossed the oxygen plasma beam. Therefore, it is assumed that only oxidized effusion cell material arrives at the surface and no pure La-Sr, Sr-Mn or Mn-La interaction was taken into account. The 900 °C warm substrate is providing the incoming effusion cell material with energy.

After finished sample growth, the samples are investigated via LEED inside the buffer line. For LSMO, energies between 50 eV and 300 eV were used to perform backscattering diffraction. While LEED can be used for determination of in-plane lattice parameters in general, due to the small difference of 1% between STO and relaxed LSMO in comparison with detector pixel resolution (between neighbour spots 80 pixels at 200 eV, 130 pixels at 50 eV for sample 049), this setup cannot distinguish between relaxed and epitaxial LSMO. Instead, nearly every sample was investigated via LEED to acquire a first glimpse of sample quality. To get a very rough idea about the oxygen saturation of the layer, the lowest energy value without electrostatic charge effects was noted. Additionally, the shape of the peaks was used to identify amorphous growth (no peaks) vs. first sights of crystallization (broad blobs, e.g. in fig. 6.3b) vs. well-defined crystalline growth (sharp spots, e.g. in fig. 6.3a). Often a superstructure was observed, similar to a 4x2 structure. Since in electron diffraction only the first few surface atomic layers are studied, the standard interpretation [66] of these superstructures is a degradation of the surface layer which no longer forms a perovskite cube but reconstructs with respect to the interface towards vacuum.

4.2 Parameters used to optimize thin film oxide growth

The criteria for LSMO samples with good quality are a) flat, homogeneous films, b) with good crystalline ordering within these films, and c) a high ferromagnetic transition temperature. Additionally, the reproducibility of standard LSMO films is a crucial step to be able to tune single preparation parameters of LSMO without questioning if effects can be related to the one variation inside the investigated sample or if the observed effects are inside the general sample preparation errorbar. The final parameters are listed in tab. 4.2 (p. 41).

4.2.1 Substrate pre-treatment

For the samples described in this work, Si and STO substrates were used. After evaluating different cleaning procedures, in the end, the Si and STO substrates were heated to 1000°C inside UHV for 10 to 15 hours. The STO substrate showed after that procedure rather a blue-grey color than the previous white color [67]; after being exposed to oxygen plasma inside the MBE main chamber, the substrate turned white again indicating no longer exhibiting oxygen vacancies. For details, see section C.1.1 (p. 147).

4.2.2 Element evaporation rates

To produce LSMO, a stable oxygen plasma was necessary during sample growth which may last up to 4 hours. Due to the maximum value of 250 W for forwarded plasma given by the MBE manufacturer, and a preferred reflected plasma value of below 5 W, these conditions could be obtained by choosing an oxygen flow of 0.22 Standard Cubic Centimeters per Minute (sccm). This flow leads to an MBE chamber pressure of 1.4*10^{-5} Torr. The rates of La, Sr and Mn were determined via Quarz Crystal Balance (QCB) in absence of oxygen plasma; after ramping up the effusion cells to the targeted temperature interval, the cells were put on stable rate for a week while adjusting the cell temperature (or cell output).

After the 1-week-calibration procedure, the La rates are that stable that from one day to the next one, the effusion cell temperature is not changed (± 2 °C), while Mn has to be adjusted around 5 °C to 10 °C and Sr from 5 °C to 15 °C. Before the daily calibration, the La getter effect was awaited: Within 5 minutes, the MBE chamber pressure falls 1 to 2 orders of magnitude. This is interpreted as the effect of the LaO cap inside the La effusion cell crucible from the last sample growth evaporating or cracking and thus the now pure La starting to react as the getter material.

To prove the $La_{2/3}Sr_{1/3}Mn_1O_3$ stoichiometry, after sample preparation the sample was investigated via XRR to determine if the total layer thickness and sample roughness qualified the sample for RBS measurements. If so, the samples stoichiometry was checked via RBS. The so gained information was used in an iterative process to optimize the effusion cell rates until the nearly stoichiometric sample 115 was produced; the next trial was performed onto STO, where immediately RHEED intensity oscillations were visible.

For $La_{2/3}Sr_{1/3}Mn_1O_3$, the following relation was used as a starting point for stoichiometric growth with m standard atomic weight and δf change of frequency [Hz/s]:

$$\frac{3}{2}\frac{\delta f_{La}}{m_{La}} = \frac{\delta f_{Mn}}{m_{Mn}} = \frac{3}{1}\frac{\delta f_{Sr}}{m_{Sr}} \tag{4.1}$$

leading to δf_{La}=δf_{Mn}*1,6856 and δf_{Sr}=δf_{Mn}*0,5316. In the end, following frequency change values were used: δf_{Sr}=0.653 Hz/s, δf_{Mn}=0.0825 Hz/s, and δf_{La}=0.1199 Hz/s, with an accuracy of 0.001 Hz/s.

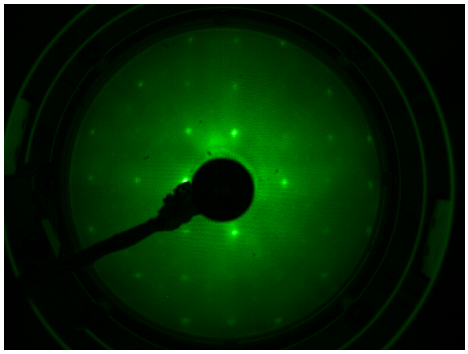

(a) LEED of sample 049 (900 °C)

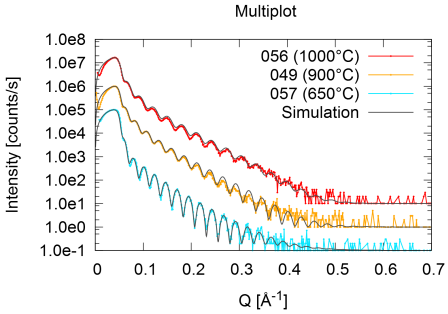

(b) XRR of samples 057 (650 °C), 049 (900 °C), 056 (1000 °C)

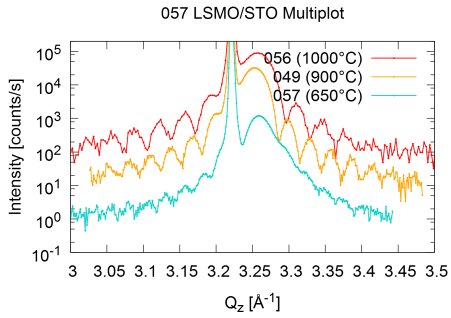

(c) XRD of samples 057 (650 °C), 049 (900 °C), 056 (1000 °C)

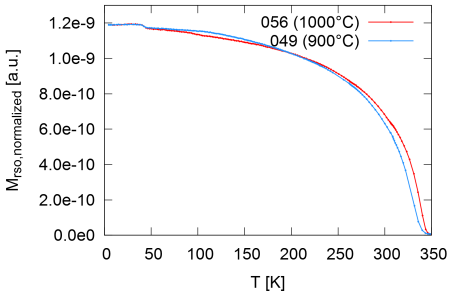

(d) SQUID of samples 049 (900 °C), 056 (1000 °C) FC

Figure 4.1: LEED, X-Ray measurements and SQUID FC measurements to determine structural quality; for clarity, X-ray measurements are shifted in y

Table 4.1: Parameters and errors for XRR fits of samples 049, 056, 057; for 049 and 056 no capping layer was necessary

	Sample name	049 (900 °C)	056 (1000 °C)	057 (650 °C)
Capping layer	delta [10^{-6}Å^{-2}]			10.6 (1.0)
	thickness [Å]			38.9 (3.9)
	roughness [Å]			24.7 (2.8)
LSMO layer	thickness [Å]	229.0 (2.6)	198.8 (2.0)	251.3 (1.4)
	roughness [Å]	5.5 (0.5)	4.9 (0.3)	6.5 (1.4)
STO substrate	roughness [Å]	3.4 (4.5)	4.9 (3.0)	3.3 (2.3)

4.2.3 Growth temperature

In thin film preparation, the substrate temperature during film growth is an important parameter. For thin film manganite growth the values in literature vary [68–70]. Literature temperature values used by other groups might even be restricted by the oven material; if a sample heater will crack at a temperature of 550 °C, the samples can only be produced at temperature values far below 550 °C. For LSMO thin films grown on STO, room temperature deposition leads to amorphous growth. With increasing temperature, a crystalline structure can be observed while a too high temperature will lead to interdiffusion (intermixing of substrate and layer material). At very high temperatures (> 2080 °C), the substrate will melt.

Changing the substrate temperature also influences the stoichiometry. High temperature during growth can give raise to oxygen deficiencies. Additionally, the sticking coefficients for the elements vary with temperature. Taking as a starting point the known values for fabricating LSMO in Jülich (JCNS-2), in order to achieve a reliable stoichiometry, samples were produced at three different temperatures, 650 °C (sample no. 057), 900 °C (no. 049), and 1000 °C (no. 056). All parameters except the substrate growth temperature were identical, e.g. after growth the samples were cooled down at a rather slow rate of 20 K/min in the same oxygen plasma at 10^{-5} Torr. For all three samples, rates of Sr, La and Mn effusion cells were calibrated before growth via QCB towards identical rates. Oxygen plasma was checked for stability during growth and cooling-down procedure. The effusion cell material was deposited for all three samples for 90 minutes. After choosing a proper temperature, the stoichiometry was further optimized.

For this sample series, RHEED was not performed during sample growth. LEED after growth of sample 049 in fig. 4.1a shows well-defined spots. XRR and XRD measurements were performed to evaluate the growth-temperature dependent structural quality. The XRR data in fig. 4.1b show a favorite preparation temperature of 900 °C due to the lower roughness compared to 650 °C and higher total layer thickness compared to 1000 °C. For 1000 °C, the layer thickness is significantly thinner (199 Å vs. 229 Å, see tab. 4.1), indicating desorpting material at a too warm substrate. For 650 °C a suitable simulation of the measured graph can only be performed with an additional capping layer with a scattering length density of 55 % of a 38Å thick layer with a roughness of 24Å which can be interpreted as surface droplets covering only half of the surface area. In combination with the tiny crystal truncation rod oscillations in the XRD pattern in fig. 4.1c, 650 °C is too low. For XRD in fig. 4.1c, 900 °C and 1000 °C both seem to be suitable. With respect to the reduced layer thickness for 1000 °C in XRR, it was opted to continue with 900 °C.

The variations of layer thicknesses for different substrate temperatures at equal quartz crystal rates for the same elements and deposition times emphasized the need to first choose a temperature and then to optimize the stoichiometry.

The magnetization vs. temperature of the 900 °C and 1000 °C grown samples were measured via SQUID, see fig. 4.1d. The Curie temperature as well as the magnetic moment is identical within the errorbar. T_C amounts to ~340 K. For Sample 057 the signal was lost during cooling down-procedure. More important than a high Curie temperature was a single phase observation of the well-defined Curie temperature. This single magnetic phase is given for both, 900 °C and 1000 °C. The kink around 50 K was explained to originate from the para-to-ferri-magnetic transition of oxygen [71].

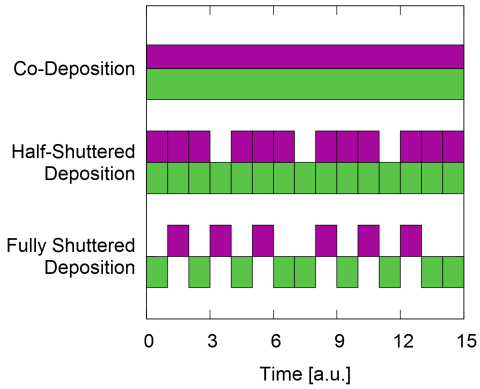

Figure 4.2: Production produces for nominally $(LS)_4M_3O$ via MBE. Green represents opened La and Sr shutters, violet represents opened Mn shutter. Note that for co-deposition, the violet rectangle should be shorter than the green one

4.2.4 Growth deposition mode

Three different types of deposition methods have been pursued in this work. There is co-deposition, for which all used effusion cell shutters open and close simultaneously, as visualized in fig. 4.2. In this figure, green is visualizing the shutter movements of the A material effusion cells and B is represented by the purple areas. Given perfect rates to achieve the $A_1B_1O_3$ stoichiometry, the RHEED pattern does not change from the original perovskite structure. Minor differences in stoichiometry will lead for LSMO to AB commutation [1]. Larger off-stoichiometry gives rise to violation of the perovskite structure and can end in crystalline, non-epitaxial thin films or amorphous layers(see e.g. fig. 6.4b). Previous work at the off-stoichiometric LSMO series was performed at the MBE setup in Sorrento by Orgiani et al. ([1, 72–74]).

Shuttered deposition makes use of the independent element evaporation of effusion cells for MBE growth. For assumed atomic-layer-by-layer (ALL-MBE) growth or fully shuttered growth mode, the perovskite unit cell is sliced into an AO layer and a BO_2 layer; for LSMO the La and Sr shutters simultaneously open or close and alternatively with the Mn shutter while the oxygen plasma shutter is constantly open.

To realize different stoichiometries after growth of several stoichiometric ABO_3 layers the material for one additional AO or BO_2 layer is introduced using additional opening time of the A or B effusion cells. For half-shuttered growth, all effusion cells are opened to grow the perovskite part; only to introduce the off-stoichiometry, the A (or B) shutter is closed, the B (or A) shutter remains open the whole time. With shuttered growth and A-overdoping, the so-called Ruddlesden-Popper series has been produced for $SrTiO_3$ by other groups [8].

Table 4.2: Used MBE parameters for $La_{2/3}Sr_{1/3}MnO_3$ growth

Substrate material	$SrTiO_3$
Substrate pre-treatment	heating in UHV at 1000 °C for min. 8 h
Effusion cell calibration time	1 week
La rate	0.1199 Hz/s ±0.001 Hz/s
Mn rate	0.0825 Hz/s ±0.001 Hz/s
Sr rate	0.0653 Hz/s ±0.01 Hz/s
Day-to-day cell temperature variation	5-15 °C
Growth rate	1 u.c./min.
Heat up rate	50 K/min
Cool down rate	20 K/min.
Substrate temperature	900 °C
Preparation pressure	10^{-5} Torr (98 % O_2)
Oxygen flow	0.22 sccm
Effusion cell equilibrium time	1 week

4.2.5 First RBS-proven stoichiometric sample (#134)

15 samples were investigated via RBS. The first sample with RBS-proven correct stoichiometry of $La_{0.68}Sr_{0.32}Mn_1O_3$ is sample 134 (fig. 4.3f). The fine tuning of effusion cell stabilization took more than 6 hours, during which the effusion cell temperatures deviated less than 5 °C from the final values while providing a constant rate, see fig. C.1a. A RHEED image was taken after sample growth (Fig. 4.3a). Though the beam was not perfectly focussed, the RHEED picture already shows crystalline order. The stripe-shaped aura around the bright spots inside this image is related to a really smooth, but not ideal flat surface [75].

LEED (fig. 4.3b) shows well-defined spots indicating a crystalline surface structure. Superstructural peaks are visible, revealing a surface reconstruction. The LEED signal is lost at 75 eV, implying an ok oxygen saturation (see section 5.2).

The sample was further investigated via X-Ray reflectivity and diffraction. The total layer thickness is 363.6 Å while 7.6 Å rough, the crystalline thickness was determined to be 344 Å (roughness 6 Å) with an out-of-plane lattice parameter of 3.852Å. Assuming epitaxial growth, therefore in-plane parameters given by the $SrTiO_3$ substrate, the unit cell volume is determined to be 58.76 $Å^3$, which is 0.4 $Å^3$ or 0.7 % larger than ICSD [30] bulk value for LSMO and therefore in good agreement. This proves that the plasma collapse during sample preparation in fig. C.1b has no impact onto the sample quality concerning oxygen saturation. The kink in the field-cooled magnetometry measurement in fig. 4.3e is at the STO cubic-to-tetragonal transition temperature [76].

4.3 RHEED intensity oscillations visualization

If regions of interest inside the RHEED detector image are integrated and displayed vs. time, changes of the crystallographic structure can be observed. In case of very flat surfaces and

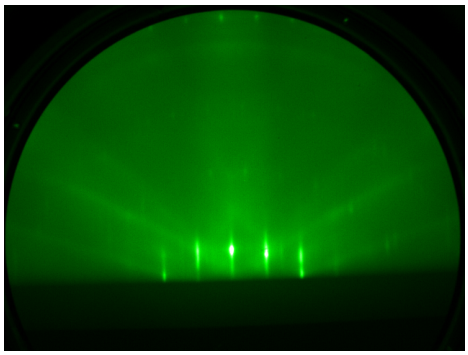

(a) RHEED of sample 134ab after growth, not perfect adjusted

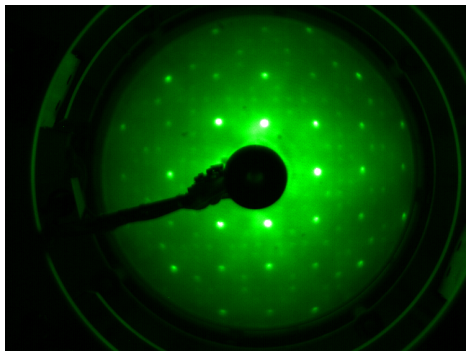

(b) LEED at 200 eV of sample 134ab

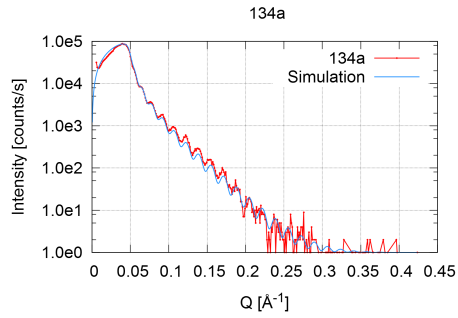

(c) XRR data and fit of sample 134a

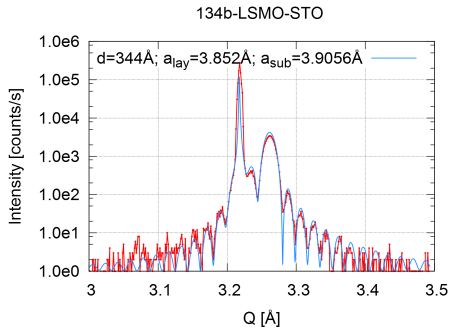

(d) XRD data and simulation of sample 134a

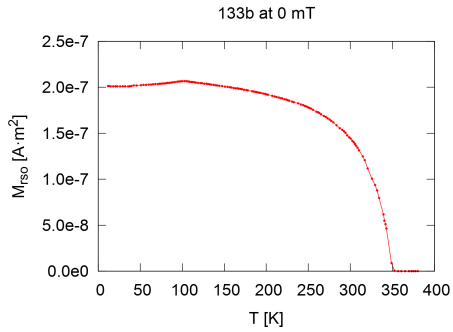

(e) Field-cooled measurement of sample 133 (produced identically as sample 134)

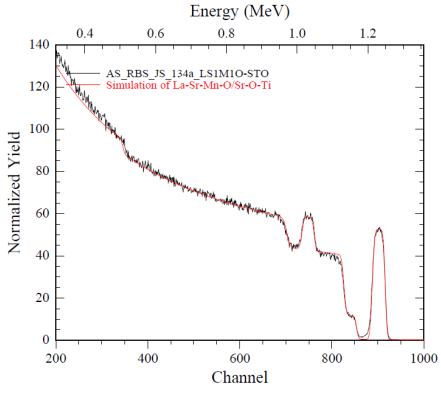

(f) RBS of sample 134a

Figure 4.3: Structural, magnetic and stoichiometric characterizations of sample 134ab (LSMO)

epitaxial growth, it is feasible to observe atomic-layer-by-atomic-layer growth via RHEED intensity oscillations. For most samples in this work, the RHEED oscillations were observed for the specular spot and for other lattice reflexes. The behavior of these spots was then used to modulate and monitor the stoichiometry by shuttered growth.

In fig. 4.4, data acquisition and visualization is displayed. Fig. 4.4a shows a screenshot of the RHEED pattern during growth with the marked areas used for the integrated intensities, below the corresponding column number inside the RHEED logfile for the marked areas is noted.

For further analysis, the RHEED intensity was compared to the opening times of (La/Sr) and Mn shutters. These opening times were controlled via a recipe and therefore double documented via the saved recipe and the MBE logfile. During preparation, the RHEED data recording was started shortly before sample preparation recipe and the time difference was noted.

Column 4 of the RHEED recording is monitoring the whole specular spot, column 2 the upper part of the specular spot. Due to an intensity-saturated monitor, the fringes of column 4 are capped from the top. In fig. 4.4b the intensity of column 4 is plotted vs. time. The information from the recipe was used to generate rectangles in the background. The green rectangles show the opening times of the (La/Sr) shutters, while the Mn shutter opening times are symbolized via purple rectangles.

During the interval of one violet and one green rectangle, one LSMO unit cell is evaporated; if there are two green rectangles, the second one is supposed to insert a one atom high LSO rocksalt structure introduced in section 2.1.1 (p. 16). The RHEED intensity oscillations appear to be influenced by a double-opening of La/Sr; there is a intensity dip at these positions.

When comparing the measured oscillations with the shutter motions, a correlation seems to exist. Still, a detailed comparison is difficult. Therefore, a second type of visualization was used.

For the second visualization in fig. 4.4c, after every 14 effusion cell shutter movements (14*70 s = 980 s) a line break was introduced via subtracting 980 s in time and 70 a.u. in intensity. In fig. 4.4d, the axes of fig. 4.4c are relabeled to emphasize the relation between RHEED intensity changes and shutter movements.

Again, the MBE recipe was used to display the effusion cell shutter opening times, (La/Sr) via green rectangles and Mn via purple rectangles. The same line break procedure used for the RHEED data was applied on the rectangles. With the line break visualization, it is far easier to determine the impact of shutter movements on the RHEED intensity during whole deposition. In fig. 4.4c, the first obvious observation is the similar behavior in all lines; all lines in a specific purple or green column show the same characteristics after line 2, shutter interval 2. The sudden decrease after switching from Mn (purple) to La/Sr (green), the additional bumps in the La/Sr deposition, can now be detected and taken under further investigation in chapters 5 and 6.

Therefore, RHEED intensity oscillations are correlated to deposition of Mn and La/Sr periods. This shows the relation of the deposited material to the crystalline sample quality and it is assumed that the RHEED intensity oscillations are a suitable surveillance method for the vertical local stoichiometry.

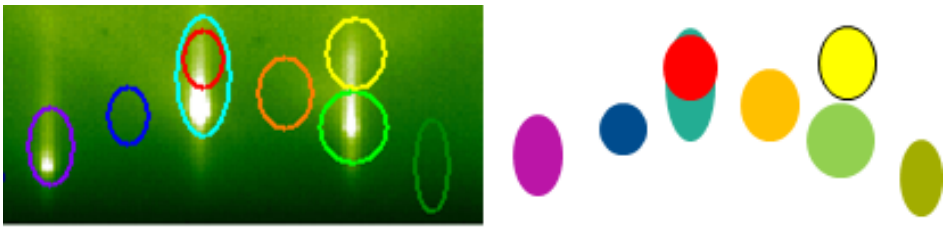

(a) Screenshot of RHEED area detector during growth of sample 291 ($(LS)_4M_3O$); a posteriori evaluation of the marked areas rendered the most significant area where the dependence of intensity changes and deposition can be evaluated

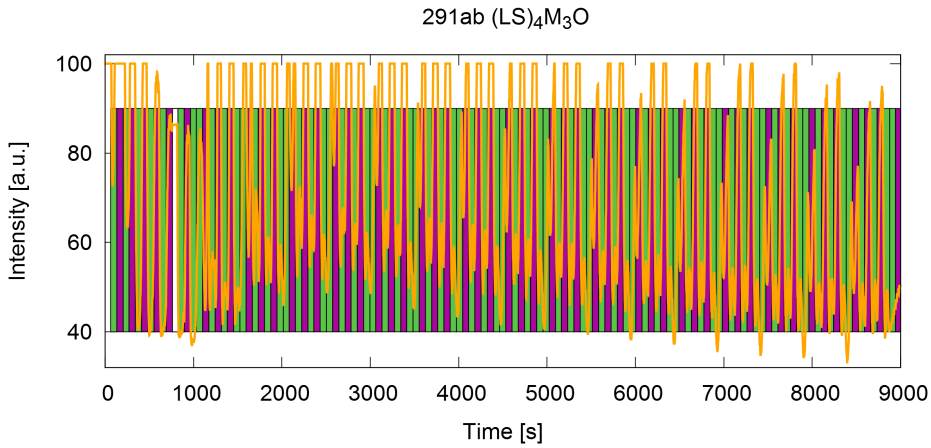

(b) Intensity of the specular spot (turquoise oval); MBE recipe visualization displayed in background; green area: time interval of opening La/Sr shutters; violet: time interval of opening Mn shutter

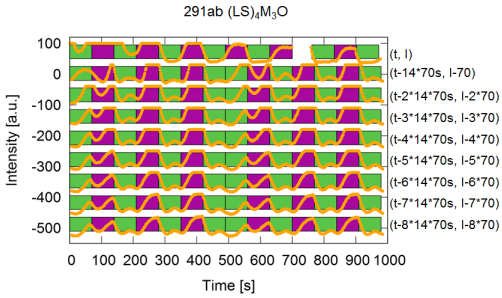

(c) Line break representation of fig. 4.4b: The first line is identical to the first 1000 s in fig.4.4b. Starting from the 2nd line, the intensity as well as the MBE recipe visualization is shifted along the time axis about 14*70 s and along the intensity axis around 70 a.u.

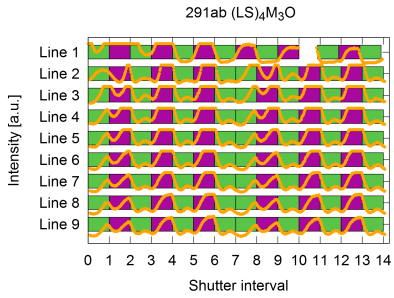

(d) Axis relabeling of fig. 4.4c, now time axis converted into MBE recipe shutter openings

Figure 4.4: Different visualizations of RHEED intensity oscillations of sample 291 ($(LS)_4M_3O$)

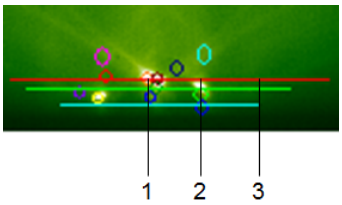

(a) RHEED detector screenshot before growth of sample 296; line cut of line 1-3 with red line corresponds to line 1-3 in fig. 4.5c

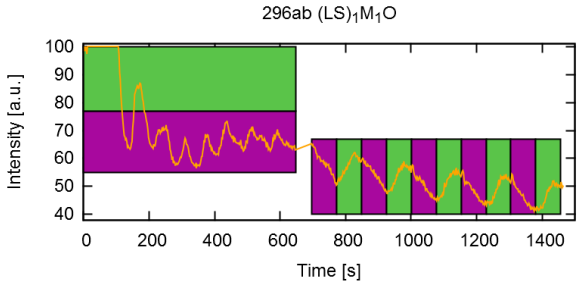

(b) RHEED intensity of specular spot; 0-646 s: Co-deposition; 698-1460 s: Shuttered deposition

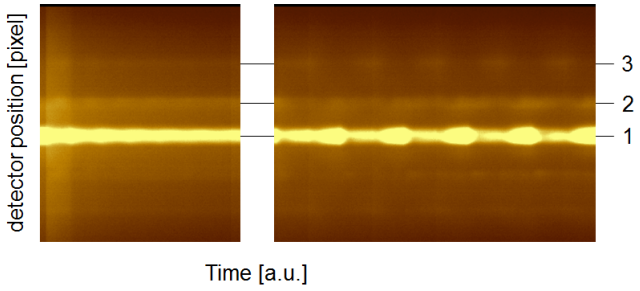

(c) Intensity along the red line of fig. 4.5a vs. time from 0..1400 s (left-hand side: Co-deposition; righ-hand side: Shuttered deposition)

Figure 4.5: Calibration procedure for shuttered growth deposition

4.3.1 RHEED-assisted stoichiometry calibration procedure

Before sample preparation via shuttered growth, the rates of the effusion cells for La, Sr and Mn were carefully calibrated as described in section 4 (p. 35).

After quartz crystal calibration, 5 to 7 unit cells of co-deposited LSMO were grown on a calibration sample to determine via RHEED the time span to grow one unit cell, see the first 646 s of fig. 4.5b. This time varied from one to the next day from 75 to 78 seconds. Then, via recipe 5 unit cells of LSMO were grown via the shuttered growth technique to test if the RHEED intensity oscillations appeared for the used shutter opening time, see fig. 4.5b starting at 698 s. The stoichiometry of La:Sr cannot be verified by this method.

Via the RHEED setup, aside from integrated areas (circles marked in fig. 4.5a) line scans can be performed, too. In fig. 4.5c the intensity of the red line in fig. 4.5a is displayed vs. time. The bright intensity (marked by line 1) is the position of the specular spot. Other spots at this line oscillate, too, but are phase-shifted, e.g. the feature marked by line 3. This proves that the RHEED intensity oscillations are produced by crystalline changes and are not a crosstalk artifact of the shutter movements and the RHEED electron beam.

Chapter 5

$La_{2/3}Sr_{1/3}MnO_3$ codeposition

In the following, the way to achieve the correct stoichiometry is presented. In the next step, the boundary conditions have been investigated, i.e. how precisely a sample can be reproduced.

The series of samples 156-168 determined the boundary conditions how precisely a sample can be reproduced while attempting to get exactly the same sample. Further, sample 196a verified epitaxial growth for the growth parameters of tab. 4.2.

5.1 Structural reproducibility (#156-168)

To evaluate if samples with identical rate settings and identical deposition parameters differ and how much twin samples (two samples in one sample holder, prepared at the same time) vary, i.e. if there is a spacial variation of the sample quality, 6 twin samples were produced. For these samples, the sample preparation parameters, substrate growth temperature, optimized rates for La, Sr and Mn, the oxygen flow and the deposition time of sample 134 were used to grow $La_{2/3}Sr_{1/3}Mn_1O_3$ via co-deposition.

In fig. 5.1, the RHEED intensity was measured during growth in [1 0 0] orientation for sample 159. During growth, oscillatory behavior (see section 3.4.1) of the intensity of the spots was observed and therefore multiple screenshots were taken in addition to the integrated intensity vs. time file. From fig. 5.1a to fig. 5.1b to fig. 5.1c, dots transform into stripes and then back into dots. The dot-to-stripe-to-dot transformation indicates in agreement with [45] and [47] that during one intensity oscillation one single perovskite cell is grown.

From fig. 5.1a to fig. 5.1g, the total detector (background as well as spots) becomes darker. This is typical for growth of here presented samples. One approach is that the crystalline structure of a layer is never as good as the one of a substrate and therefore a decrease of the reflected intensity at the beginning of the scan is probable. Another idea is that this effect could arise from the amount of oxygen which has different influence on the performance of the RHEED gun and the electron beam over time. This is supported by the observation that after preparation, when the oxygen is removed from the chamber, the monitored intensity of the whole detector rises drastically.

The area inside the red circle around the specular spot was integrated and displayed in dependence of time. In fig. 5.2, a section of this integrated intensity is displayed vs. time. Inside, the data points of the screenshots are marked.

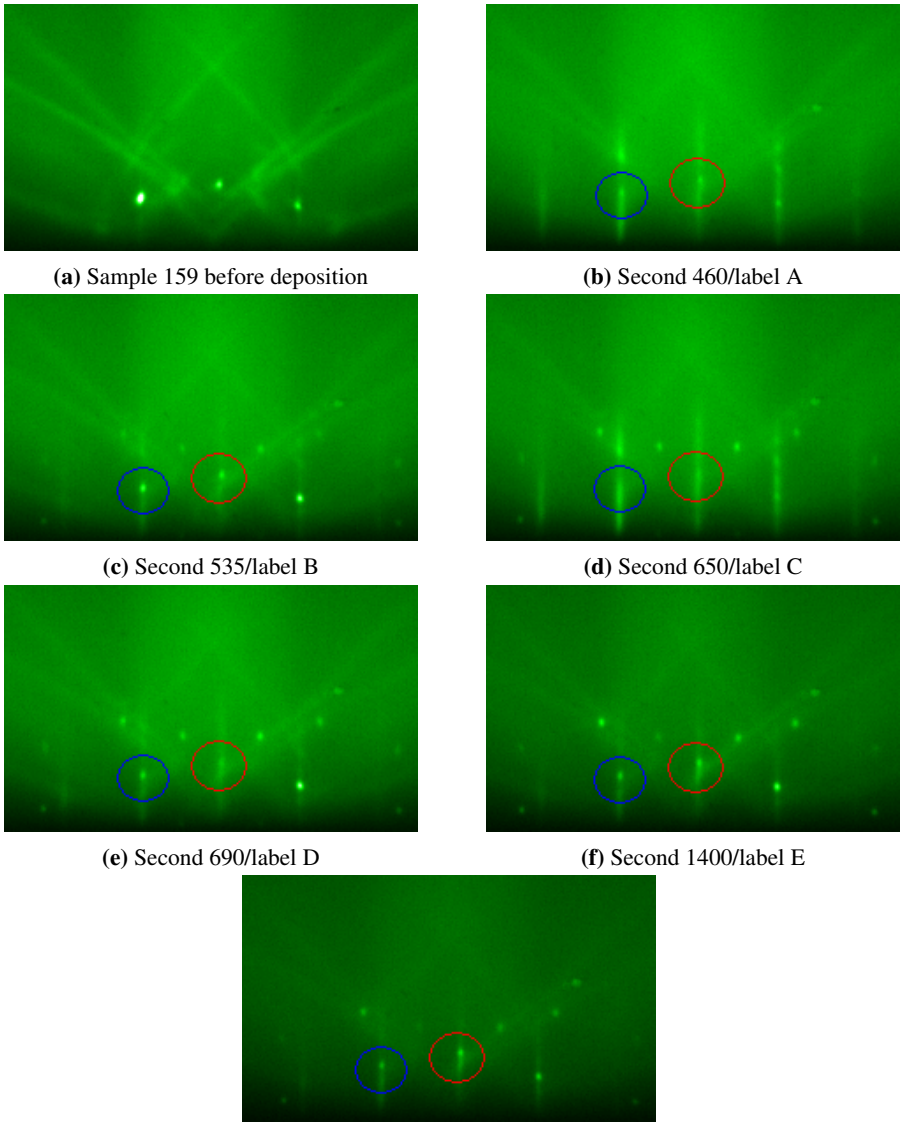

(a) Sample 159 before deposition

(b) Second 460/label A

(c) Second 535/label B

(d) Second 650/label C

(e) Second 690/label D

(f) Second 1400/label E

(g) Second 2170/label F

Figure 5.1: RHEED screenshots and the corresponding data points in the RHEED intensity vs. time graph during growth for sample 159. The RHEED background becomes significantly darker with time; this is not only an effect of the displayed specular spot and due to worsened reflectivity. The area of the red circle is integrated and displayed vs. time in fig. 5.2, see text for detailed explanation

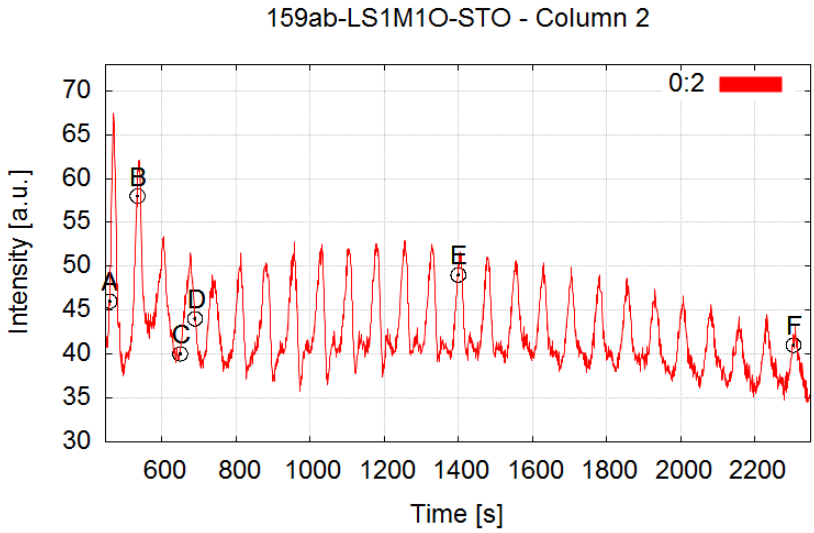

Figure 5.2: Intensity variation of the specular spot vs. time with highlighted positions for screenshots in fig. 5.1

The stripes-dots-stripes behavior of the RHEED patterns causes the effect that depending on which area is integrated exactly, the intensity can increase or decrease when the specular reflex is transforming towards a dot again. Therefore, in this work the RHEED intensity is monitored wheter it is changing according to MBE recipe but the changes themselves are not evaluated further.

During the production of this sample series, RHEED settings were optimized and therefore RHEED data details of different samples are not comparable. To quantify the reproducibility, XRD measurements were performed, see fig. 5.3. For all samples, due to the high sample quality leading to well-pronounced fringes, the out-of-plane lattice parameters and crystalline layer thickness could be determined, see tab. 5.1. The lower intensity of sample 165a and 166a is related to shorter XRD measurement times and not related to the sample quality. Fig. 5.3b shows that lattice parameter and layer thickness differ not much for the different samples, but there is no further correlation like that a bigger lattice constant is correlated with a higher layer thickness.

The STO-like LSMO patterns observed in fig. 5.4 for electron energies at 200 eV are well-known (see, for example, ref. [77] and references within). The quality of LEED spots is not completely related to the lattice parameter in fig. 5.3b extracted from XRD patterns in in fig. 5.3. Via XRD, a crystalline layer thickness average of 271 Å $\pm$ 10 Å was determined and an averaged lattice parameter of 3.849 Å $\pm$ 0.006 Å. The most blurred LEED spots for sample 165ab directly correlate to the very large difference of lattice parameters for 165a and 165b. For an enhanced background signal, visible in LEED for 159ab, 166ab and 168ab, neither the lattice parameter nor the thickness fringes show any atypical behavior, leading to the explanation that the background originates from bad LEED adjustment. The very small deviation of the lattice parameter inside this sample batch shows that reproducible sample quality was achieved, but

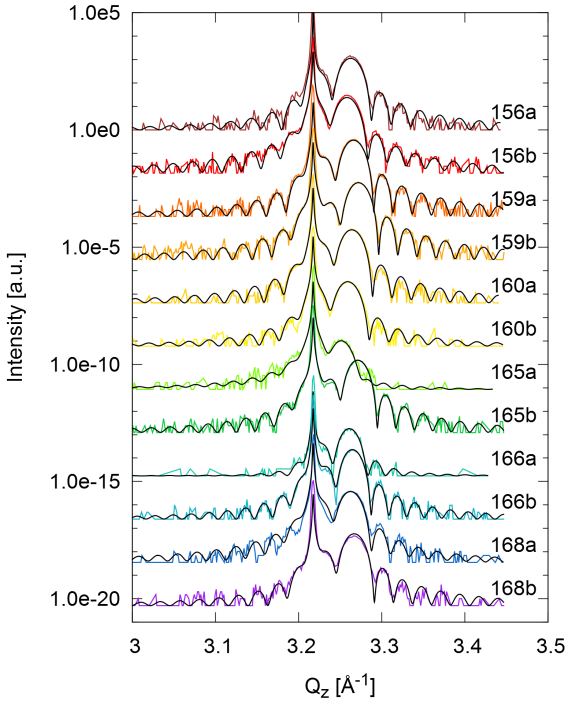

(a) XRD data and simulation of samples 156-168 around the (0 0 2) substrate peak, for clarity shifted in intensity

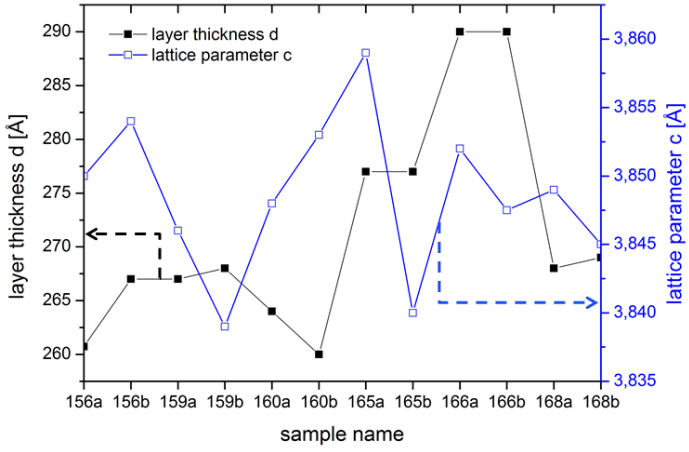

(b) Lattice parameters and crystalline layer thicknesses used as input for the simulations in fig. 5.3a with average layer thickness of 271 Å (error bars for d 1 Å, for c 0.001 Å

Figure 5.3: 156 - 168: Diffraction around (0 0 2) substrate peak to compare crystalline quality

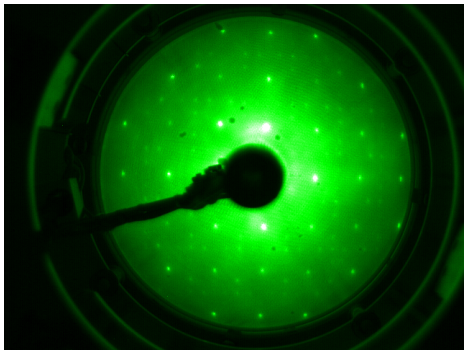

(a) 156ab

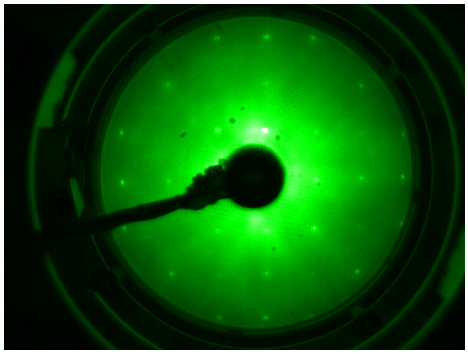

(b) 159ab

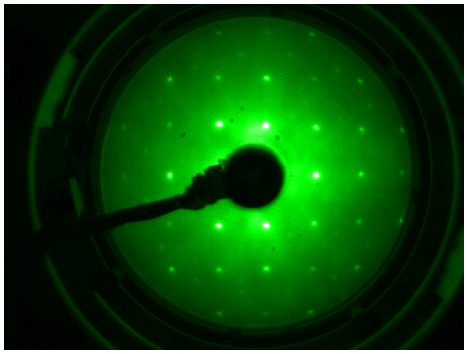

(c) 160ab

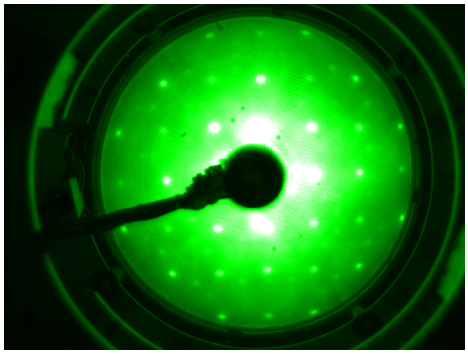

(d) 165ab

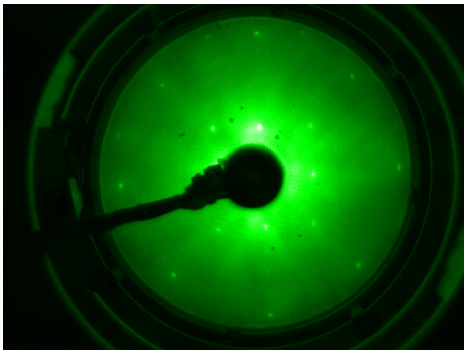

(e) 166ab

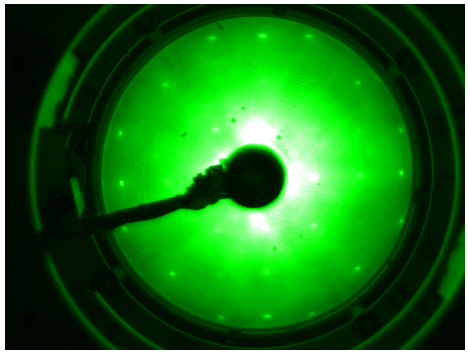

(f) 168ab

Figure 5.4: LEED at 200eV for samples 156 - 168. Due to a single-crystalline surface, all samples show the existence of well-defined spots and identical in-plane parameters (within the systematic errorbars of the LEED acquisition)

Table 5.1: 156-168: Parameters for XRD fits (c out-of-plane lattice parameter, d crystalline layer thickness; error bars for d 1 Å, for c 0.001 Å

Sample name	sample a		sample b	
	c [Å]	d [Å]	c [Å	d [Å]
156	3.850	261	3.854	267
159	3.846	267	3.839	268
160	3.848	264	3.853	260
165	3.859	277	3.840	277
166	3.852	290	3.848	290
168	3.849	268	3.845	269

Table 5.2: 134,196: Parameters for XRD fits (c out-of-plane lattice parameter, d crystalline layer thickness; error bars for d 1 Å, for c 0.001 Å

Sample name	c [Å]	d [Å]
134b	3.851	345
196a	3.848	310

still for every sample XRD should be performed because the lattice parameters could not be directly concluded from the LEED characteristics.

In the logfiles during growth in fig. C.4, a short increase of the reflected oxygen plasma power was detected during growth of sample 168, and a long increased reflected oxygen plasma value was measured during growth of sample 159. For these samples, no enhanced out-of-plane lattice parameter was measured, which proves the full oxygen saturation of these samples.

5.2 Influence of oxygen vacancies

In transition metal oxides, oxygen vacancies are responsible for a huge variety of fascinating physical effects. In $La_{0.7}Ca_{0.3}MnO_3/SrTiO_3$, oxygen defects give rise to large photoconductivity [78], oxygen deficient ferroelectrics exhibit a metallic-like to nonmetallic transition [79], and in $KTaO_3$ thin films a polarized state could be induced [80]. In STO permanent magnetic moments can be induced by oxygen vacancies [81].

The lattice parameters for stoichiometric LSMO thin films on STO substrates can deviate from

Table 5.3: Parameters for XRR fits with d layer thickness and σ layer roughness

Sample name		134b	196a
LSMO layer	d [Å]	363.6	329.6
	d error [Å]	1.2	1.0
	σ [Å]	7.6	6.4
	σ error [Å]	0.1	0.2
STO substrate	roughness [Å]	5.7	2.5
	roughness error [Å]	1.6	2.3

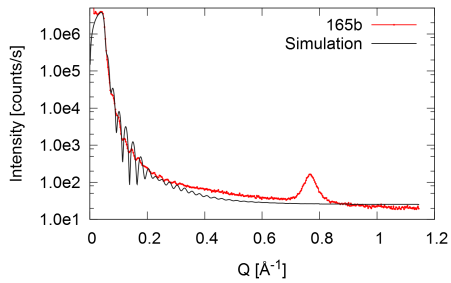

(a) XRR of sample 165b after post-annealing: Extremely rough surface

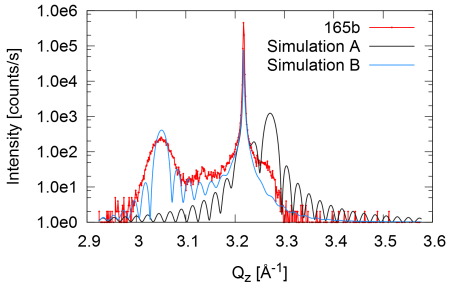

(b) XRD of sample 165b after post-annealing: Shifted layer lattice parameter

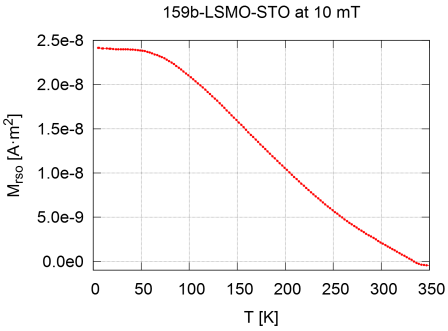

(c) Magnetic characterization of post-annealed sample 159b: Smeared out Curie temperature

Figure 5.5: Influence of post-annealing at 1000 °C in UHV on structural and magnetic properties of LSMO films

fully strained LSMO (3.83 Å) to fully relaxed LSMO (3.87 Å). Orgiani et al. [82] explained a lattice deviation from the 3.83 Å up to 3.88 Å via artificially introduced oxygen vacancies. They reported for the LSMO/STO system that post-annealing increases the out-of-plane lattice parameter while decreasing the metal-insulator transition temperature. In the most oxygen-depleted film, they estimated the amount of oxygen vacancies to be one oxygen vacancy over 24 unit cells. Schlueter et al. [83] reported for post-annealed films an increased roughness.

Two samples were post-annealed for 12 hours at 1000 °C in UHV. One sample was investigated structurally, for the other one the magnetic properties were determined.

The XRR measurement in fig. 5.5a could only be fitted with two capping layers, and that fit is still not very reliable; capping layer thickness values are smaller than the according roughnesses, and the peak in the rear part was not taken into account. The main outcome is that post-annealed samples are rough, which is in agreement with the observation of Orgiani et al. [83].

The XRD data in fig. 5.5b are simulated twice: For simulation A (black curve), the parameters were used from the fit for the same sample before post-annealing in fig. 5.3a. For simulation B (blue curve), the layer thickness of 277 Å was taken from simulation A, but the out-of-plane lattice parameter was now assumed to be 4.12 Å instead of 3.84 Å. The STO peak was at the

Table 5.4: Parameters for XRR fits with d layer thickness and σ layer roughness used in fig. 5.5a

Sample name		165b
Capping layer 2	SLD-δ [10^{-6}Å^{-2}]	16 (23)
	d [Å]	2 (149)
	σ [Å]	168 (20)
Capping layer 1	SLD-δ [10^{-6}Å^{-2}]	16 (10)
	d [Å]	40 (168)
	σ [Å]	3 (388)
LSMO layer	d [Å]	200 (58)
	σ [Å]	9 (56)
STO substrate	σ [Å]	*-7.00000e-05 (9300)*

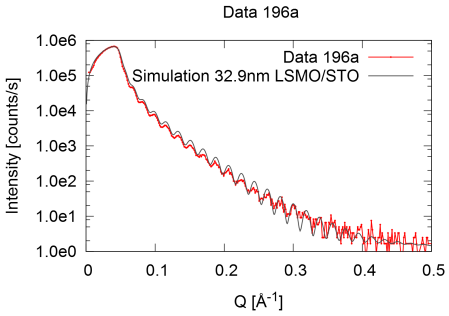

(a) XRR measurement, fitted without additional capping layer

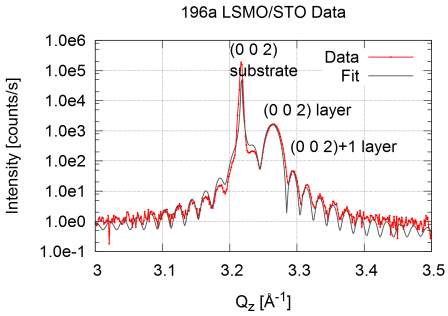

(b) XRD scan of (0 0 2) peak including fit

Figure 5.6: Structural investigation of sample 196a: Total layer thickness is 1.9 nm larger than crystalline layer thickness

expected position for fully saturated $SrTiO_3$. In contrast to the total layer thickness (gained via XRR), here the crystalline layer thickness cannot be determined due to the absence of the layer fringes.

The magnetic field-cooled curve in fig. 5.5c shows no longer a well-defined the spontaneous magnetization temperature like the measurements in fig. 4.1d (p. 38). This curve cannot be described by the formalism of Ku'zmin [84].

The high sample roughness is induced by the post-annealing process itself. The smeared-out magnetic transition temperature as well as the drastically enhanced out-of-plane lattice parameter are caused by the oxygen vacancies.

5.3 Verification of epitaxy (#196a)

Within the field of thin oxide films, epitaxial growth is a desired property and not necessarily a given. For this work, several layers of approximately 250 Å LSMO/STO were produced

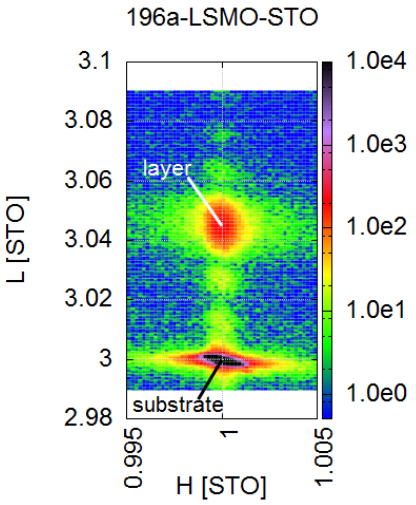

(a) XRD map around (1 0 3) substrate peak - epitaxial layer growth due to identical in-plane parameter of substrate and layer

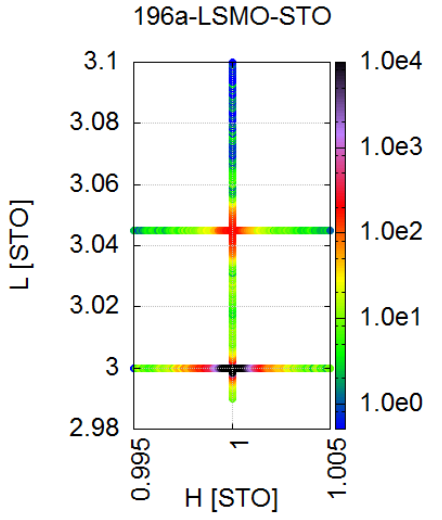

(b) line scans of region of fig. 5.7a. Position, size and shape of layer as well as substrate peak can be identified

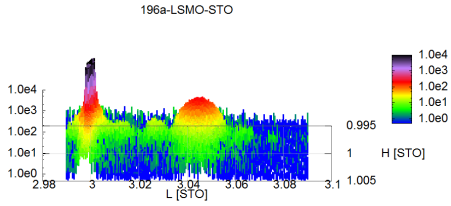

(c) rotated view of fig.5.7a, to compare with fig. 5.7d

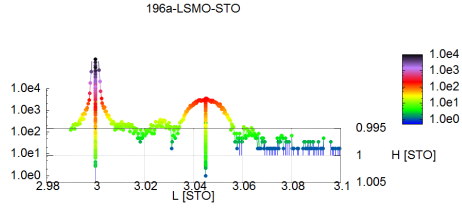

(d) rotated view of fig.5.7b - no further information via map, compared to line scans; layer fringes already visible in line scan

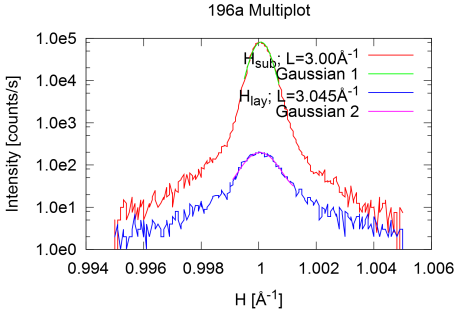

(e) Line scans along H through substrate and layer peak

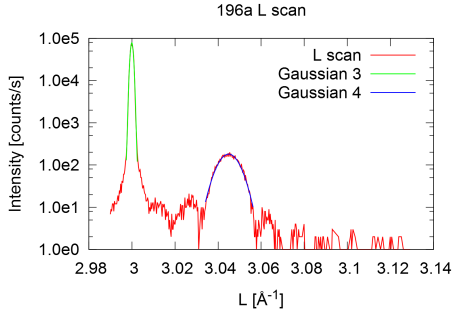

(f) Line scan along L through substrate and layer peak

Figure 5.7: 4-circle measurements of (1 0 3) peak of a LS_1M_1O sample; all intensity scales in [counts/s]

via co-deposition. If the layers show well-defined fringes in a pure out-of-plane XRD scan around the layer peak with a crystalline layer thickness in order of the total layer thickness, they are assumed to grow epitaxially, without any relaxation behavior. To verify this, the in-plane lattice parameters for one representative sample were measured in detail via reciprocal space map (RSM). This measurement was performed at the four circle diffractometer at WMI, Garching.

A good visualization program to display all accessible reflexes for Bragg geometry and show reciprocal-space scans with correspondent movement in real space is XVis [85], a good introduction in thin film diffraction is given by Fewster [86].

To characterize the in-plane lattice parameter, the (1 0 3) reflex was measured, see fig. 5.7a; for L=2.99..3.09 reciprocal lattice units (r.l.u.), H was scanned from 0.995 r.l.u. to 1.005 r.l.u.. In this geometry, the out-of-plane lattice constant can be distinguished via the l component of the layer, while for the in-plane lattice constants one assumes, that if a (non-)epitaxial growth exists in one in-plane lattice direction, the other one will show (non-)epitaxial growth, too. So, via characterization of h or k, the here investigated a and b lattice constants of tetragonal or pseudo-cubic LSMO onto cubic STO (0 0 1) are investigated simultaneously.

Before a time-consuming RSM investigation is performed, a pure out-of-plane scan should be performed from minimum (0 0 1) to (0 0 3) to identify existence of additional crystalline phases. Here, already amorphous growth can be excluded if aside from the substrate peak a layer peak is detected.

In fig. 5.6a, the XRR fit provides with total layer thickness of 328 Å and top roughness of 6.4 Å, SLD is assumed to be bulk LSMO ($18.03*10^{-6}Å^{-2}$). To determine the crystalline contribution of that layer thickness, a pure out-of-plane XRD scan was performed. In the insert of fig. 5.6b, only the substrate peaks and expected layer peaks are visible. The absence of additional peaks indicates a single phase growth. To determine growth quality, the (0 0 2) peak was fitted using the algorithm of Fullerton et al. [87] and a fully strained film was assumed. Additionally, the crystalline layer thickness was determined to be 310 Å, which is 18 Å thinner than the total layer thickness. This is approximately 4 unit cells of LSMO material and could be the reconstructed layer material.

Fig. 5.7a shows the Reciprocal Space Map (RSM) of (1 0 3) peak of STO. The substrate position was calculated and sample aligned; the LSMO position was calculated with respect to out-of-plane scan and immediately found at expected position during aligning. Additional Bragg fringes around the layer peak were found, despite the fact that at an asymmetric position (such as the investigated (1 0 3) position) it is not common to detect these oscillations, proving the high quality of this film.

To test a faster quantification procedure of the epitaxy, line scans of fig. 5.7b through substrate and layer maximum in H and L were performed and Gaussian fits were performed to identify the exact positions of substrate and layer, see fig. 5.7e and 5.7f. To emphasize the analogy in information of lines scans and RSM, both, RSM and line scan were displayed in the identical 3D representation in fig. 5.7c and 5.7d; in both graphs, even the additional fringes are clearly visible.

The Gaussian fits of the line scans in fig. 5.7e and 5.7f reveal for H values of substrate and layer 1.00007 reciprocal lattice units [r.l.u.] of $SrTiO_3$ and 1.00005 r.l.u., with a pixel size of 0.0001 r.l.u., therefore the in-plane lattice parameter of the LSMO film matches exactly the

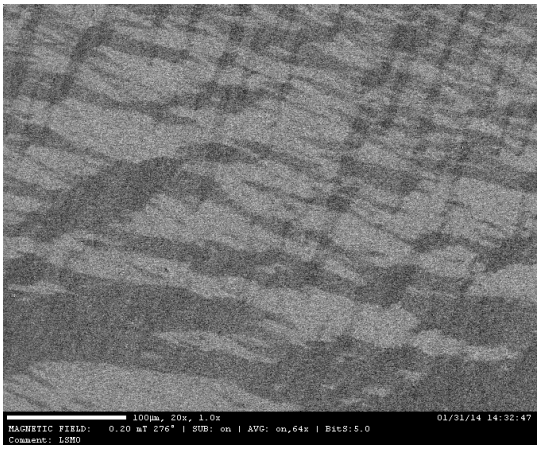

(a) MOKE microscopy image at coercitive field (0.8 mT); the scale bar is 100 μm long

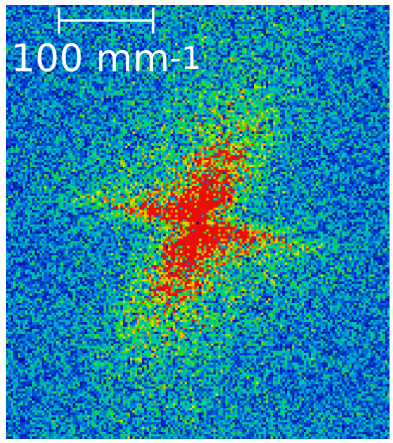

(b) Fourier transformation of fig. 5.8a

Figure 5.8: MOKE image of sample 196b

underlying STO substrate, i.e. the LSMO is growing epitaxially. For the L scan, the Gaussian fit shows the perfect alignment of the substrate (L=2.99993 r.l.u.) and reveal the layer position to be at 3.04491 r.l.u., or an out-of-plane lattice parameter of 3.8474 Å, respectively. Assuming a tetragonal unit cell, the unit cell volume is 58.67 Å^3. Compared to the ICSD [30] bulk reference value of 58.37 Å^3, this is a deviation of 0.5 %. The c/a ratio of 0.985 was expected for epitaxial LSMO onto STO. Especially the fitting values for the L scans confirm the tetragonal crystal structure and epitaxial growth of the LSMO films, the unit cell volume the correct oxygen stoichiometry (see section 5.2).

5.4 LSMO domain configuration (#196a)

Via offspecular neutron reflectometry, domain structures around 1 μm can be investigated [26, 88]. MOKE microscopy [89] was performed to determine the typical domain size inside the LSMO films to evaluate the usage of off-specular neutron reflectometry on these samples. The measurement of the MOKE microscopy image was performed at the Institute for Materials Science at Kiel University.

LSMO has a small coercive field at room temperature. For sample 196b, this small field is 0.8 mT. To achieve the domain state configuration shown in fig. 5.8a, the sample was demagnetized in a decreasing alternating magnetic field. The sample possesses two in-plane easy axes, of which one axis is a little bit easier. The magnetic field is oriented along the harder in-plane axis to get a magnetization along both axes. Indeed, domains could be identified. The existence of two in-plane easy axes shows the high quality of the well-defined sample.

The contrast is longitudinal. The easy directions of the sample are slightly tilted with respect to the sensitive axis, hence there exist 4 contrasts. In fig. 5.8a are many 90 ° domain walls and a few 180 ° walls. The domain size distribution is very broad; the Fourier transformation in

fig. 5.8b confirms the existence of two easy axes, but no distinct typical domain size leading to no homogeneous lateral structure. For this reason, the off-specular area of the PNR data was investigated further.

Chapter 6

Shuttered deposition

Shuttered deposition is needed for the production of stoichiometric samples away from LS_1M_1O. After using the shuttered growth technique to produce LS_1M_1O in section 6.1, the maximum for additional atomic layers in LSMO is tested with still crystalline ordered layers in section 6.2. In section 6.3 the stoichiometric gradients are produced and characterized.

6.1 Pure LSMO (#301): RHEED changes related to shutter intervals

Sample 301b was prepared with identical opening times of the (La/Sr) shutters and the Mn shutter, resulting in a nominal stoichiometry of $(LS)_1M_1O$. The recipe is visualized in fig. C.2d. The RHEED linebreak visualization in fig. 6.1a shows that the RHEED intensity oscillations are perfectly synchronized with the underlying opening and closing times of the shutters. Regarding the phase shift of the intensity (intensity maximum in middle of green rectangles instead of green/violet boundary), in fig. 5.1 in section 5.1 it is shown that the exact position of the integrated RHEED intensity area leads to different time values for intensity maxima inside the perovskite unit cell growth.

LEED images in fig. 6.1b reveal sharp spots at expected STO positions, and additional spots caused by surface reconstruction. Charge effects give a lower limit of useful images at 125 eV, which is an increased but still normal value for a fully oxygen saturated sample, see section 5.2.

The amount of deposited material was cross-checked via the number of MBE opening intervals and therefore assumed perovskite unit cells $N = d/c$ with d total layer thickness, c out-of-plane lattice parameter. For sample 301a, a total layer thickness of 233.3 Å (fig. 6.1c) divided by a lattice constant of 3.824 Å (fig. 6.1d) gives N=61, compared to the recipe calling for deposition of 62 unit cells of LSMO. This is a perfect correlation.

Sample 301 has a very small lattice constant, even smaller than fully strained epitaxial films of $La_{0.67}Sr_{0.33}M_1O_3$ (see section 5.1). The sharp double peak for sample 301a at Q_z=3.23 Å in fig. 6.1d indicates a twinned substrate. Nevertheless, the out-of-plane lattice parameter as well as the layer thickness are identical for sample 301a and 301b, see the fitting parameters in tab. 6.1.

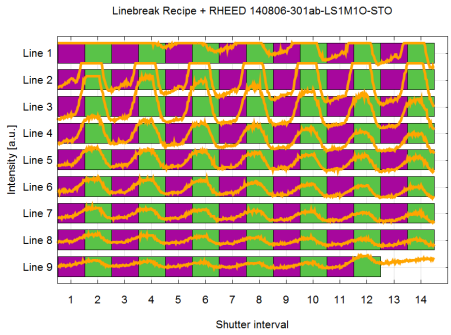

(a) Linebreak representation of RHEED intensity of sample 301ab (LSMO)

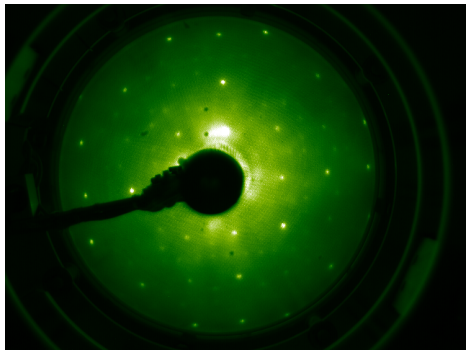

(b) LEED performed at 200eV of sample 301ab (LSMO)

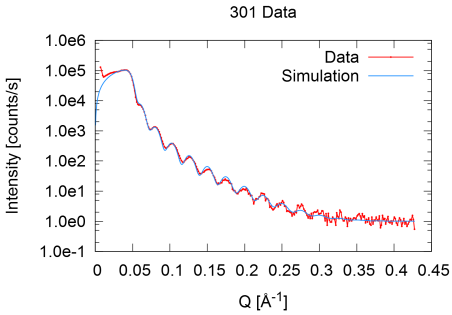

(c) XRR data and fit of sample 301a (LSMO)

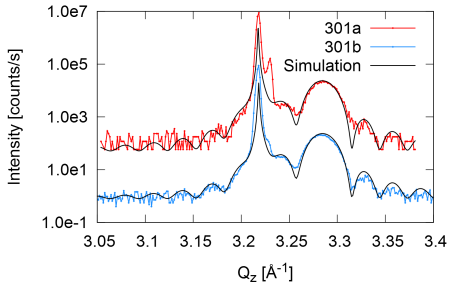

(d) XRD data and simulation of sample 301a (LSMO)

Figure 6.1: RHEED linebreak, LEED, XRR and XRD for sample 301ab

The capping layer thickness for sample 301a is 5 orders of magnitude lower than the capping layer roughness. This gives rise to fitting artifacts like the high error bar on the substrate roughness, see tab. 6.2.

6.2 Determination of maximum doping level: LS_3M_2O (#292) and LS_2M_1O (#288)

Introducing an additional atomic layer after a certain number of unit cells disturbs the crystallographic structure and therefore it is likely that the sample quality is influenced negatively.

Table 6.1: Parameters for XRD fits

Sample name	301a	301b
lattice parameter [Å]	3.824 (0.001)	3.824 (0.001)
layer thickness [Å]	212 (1)	212 (1)

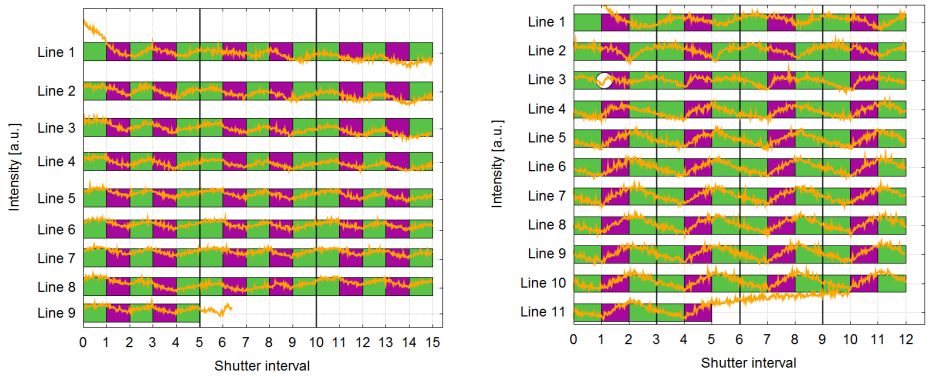

(a) Linebreak representation of RHEED intensity of sample 292 ($(LS)_3M_2O$)

(b) Linebreak representation of RHEED intensity of sample 288 ($(LS)_2M_1O$)

Figure 6.2: LS_3M_2O and LS_2M_1O: RHEED linebreak visualization

In preparation for the stoichiometric gradients, $(LS)_{n+1}M_nO_{3n+1}$ thin films were grown. For n equals 1 and 2 (LS_2M_1O and LS_3M_2O), the samples are presented here.

The corresponding RHEED intensity time graphs of samples are shown in fig. 6.2a and fig. 6.2b. Like described in section 5.1, the RHEED intensity changes are dependent on the integrated area of the detector image, but for both samples, the RHEED intensity shows a clear dependence of the oscillations from the shutter opening intervals involved in the MBE recipe. In fig. 6.2b the RHEED intensity is uncorrelated during the first 25 shutter movements (marked by a white circle).

XRR patterns in fig. 6.4a show a similar total layer thickness (see tab. 6.2); this was intended by both MBE recipes having the same amount of shutter movings, see fig. 6.2. For LS_3M_2O, the additional peak at Q_z=0.621 Å corresponds to a real space structure of 10.113 Å, which can be explained as 2.5*4.045 Å, 2 times the ABO_3 structure and one additional AO layer, which coincides with the stoichiometry implicated via recipe. XRD measurements in 6.4b show well-defined fringes for LS_3M_2O (fitting parameters: d=252(1) Å, c=3.805(1) Å), but a complete absence of crystalline structure for the LS_2M_1O film. This is somehow expected; every additional monolayer introduces a rocksalt crystal structure inside the perovskite layer. This change of crystallographic structure gets more challenging for smaller amount of buffering perovskite cells in between. This explains the better defined LEED spots for LS_3M_2O (fig. 6.3a) than for LS_2M_1O (fig. 6.3b), too. The growth parameters in tab. 4.2 work for LS_3M_2O, but no longer for LS_2M_1O; obviously, a limit for the LSMO structure via these parameters was found. Therefore, in all following samples was set in that way that the maximum doping in terms of the minimum number of perovskite unit cells before an additional atomic single layer was set such that after 2 unit cells one additional layer can be introduced.

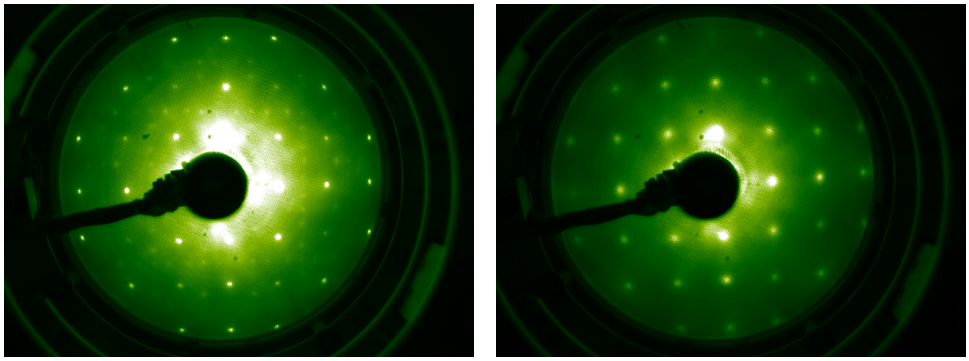

(a) LEED 200eV of sample 292ab ($(LS)_3M_2O$) **(b)** LEED 200eV of sample 288ab ($(LS)_2M_1O$)

Figure 6.3: LEED performed at samples 292ab and 288ab

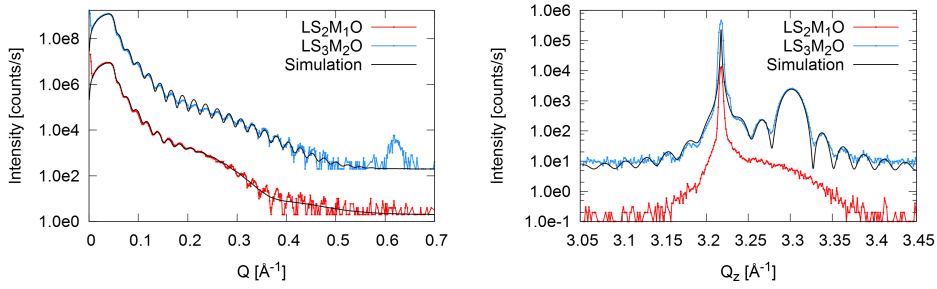

(a) XRR data and fits of samples 288ab ($(LS)_2M_1O$) and 292ab ($(LS)_3M_2O$) **(b)** XRD data and simulations of samples 288ab ($(LS)_2M_1O$) and 292ab ($(LS)_3M_2O$)

Figure 6.4: Structural investigations of samples 288ab ($(LS)_2M_1O$) and 292ab ($(LS)_3M_2O$): X-ray measurements (fitting parameters see tab. 6.2 and 6.1

Table 6.2: Parameters for XRR fits with d layer thickness and σ layer roughness

Sample name		301a	288a	292a
Capping layer	SLD-δ [10^{-6}Å^{-2}]	10.63 (1.92)	15.06 (0.22)	8.68 (1.33)
	d [Å]	0.0002 (-)	23.8 (0.4)	15.1 (1.9)
	σ [Å]	31.6 (6.8)	7.1 (0.2)	4.4 (0.5)
LSMO layer	d [Å]	243.2 (7.3)	240.8 (0.8)	243.6 (2.1)
	σ [Å]	5.7 (3.0)	3.1 (0.6)	11.1 (1.0)
STO substrate	roughness [Å]	7.7 (7.5)	9.7 (0.5)	4.9 (0.6)

6.3 Preparation of Gradient Series (#230, #224, #233)

Due to the clear response of the RHEED intensity signal on the MBE recipe-indicated effusion cell shutter opening intervals, it was assumed that the control of the local vertical stoichiometry is feasible, especially for stoichiometries varying from LS_1M_1O. Therefore, the production of stoichiometric gradients started using the parameters from table 4.2 with the aim to produce samples with different MnO gradients with respect to the film thickness.

For sample 230b (top Mn excess), (La/Sr) shutters and the Mn shutter were opened in order to evaporate more Mn at the top and bottom of the sample than in the middle of the layer, changing the recipe stoichiometry from $(LS)_2M_3O$ to $(LS)_8M_9O$ back to $(LS)_2M_3O$ from substrate to vacuum, see fig. 6.5g.

Sample 224 (top Mn excess) was produced via introducing more additional MnO layers towards top, changing from $(LS)_8M_9O$ at substrate to $(LS)_2M_3O$ at the surface.

For sample 233 (centered Mn excess), more Mn was deposited for around half of the deposition time of the sample growth, therefore recipe stoichiometry varied from $(LS)_8M_9O$ to $(LS)_2M_3O$ back to $(LS)_8M_9O$, from substrate to vacuum.

Sample 230ab (top Mn excess, fig. 6.5a) shows far less prominent RHEED intensity oscillations than sample 301a. The reason is that the settings were not fully optimized at the time of sample fabrication. Still, for all gradient samples (fig. 6.5e, 6.5c) the RHEED oscillations occur concurrently with the opening intervals of the effusion cell shutters.

LEED performed on sample 230b in fig. 6.6a shows an image far darker and cloudier, but with visible spots at every second position, without any surface reconstruction. In comparison with the other LEED images in fig. 6.6, too, the spots inside that image look less well-defined than for the rest. Compared to sample 224 (top Mn excess, fig. 6.6b) and 233 (centered Mn excess, fig. 6.6c), the LEED image of 230 (edged Mn excess) has a lower quality, which could be explained by a) defocused LEED settings or b) worse sample quality for sample 230 in comparison with the other images in fig. 6.6.

XRR data and fits are shown in fig. 6.7a. For the fit, a simple model consisting of an LSMO layer on top of a STO substrate did not describe the measured data and showed the typical discontinuities caused by a rough surface [27]. Therefore, for a first analysis (via the software "Plot-Script"), a capping layer was introduced with a small layer thickness, a roughness value larger than the layer thickness and a real part of scattering length density 80 % of the value of LSMO in order to simulate particles covering half of the surface. The resulting fitting parameters are listed in tab. 6.3. All samples have a small substrate roughness.

In fig. 6.7b, Sample 230 (edged Mn excess) has the largest lattice constant compared with the rest of the batch, indicating a low oxygen saturation. For fitting details, see tab. 6.4.

Additionally, for sample 230b a total layer thickness of 223.5 Å divided by a lattice constant of of 3.86 Å gives 57.9 unit cells. The MBE recipe calls for 70 unit cells of LSMO and 13 monolayers of MnO which is far more material than seen here although the RHEED intensity in fig. 6.5b follows clearly the effusion cell shutter movings. The observation of this difference is discussed in chapter 9.

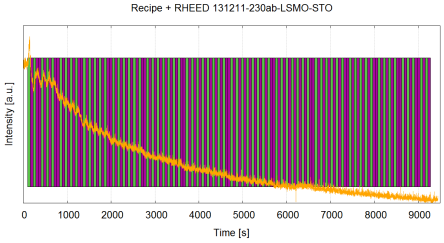

(a) 230ab: RHEED intensity incl. recipe

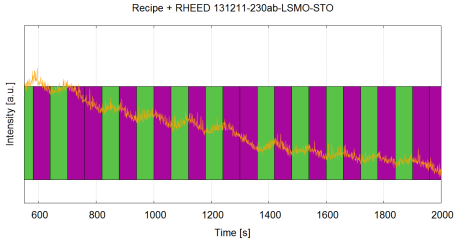

(b) 230ab: Detail of fig. 6.5a

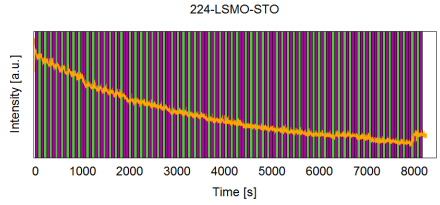

(c) 224ab: RHEED intensity incl. recipe

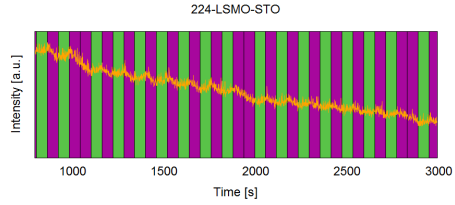

(d) 224ab: Detail of fig. 6.5c

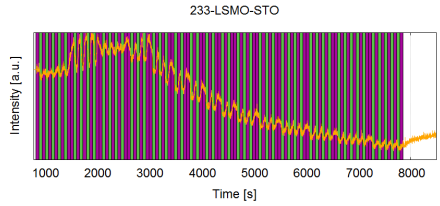

(e) 233ab: RHEED intensity incl. recipe

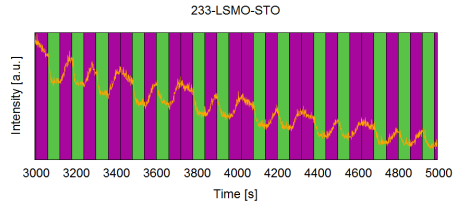

(f) 233ab: Detail of fig. 6.5e

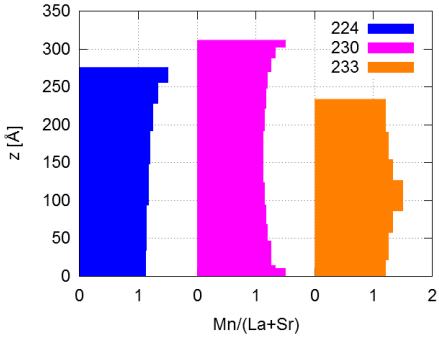

(g) Gradient samples: Nominal Mn excess stoichiometry as function of sample height

Figure 6.5: RHEED+recipe for gradient samples as described in fig. 4.4 (p. 44

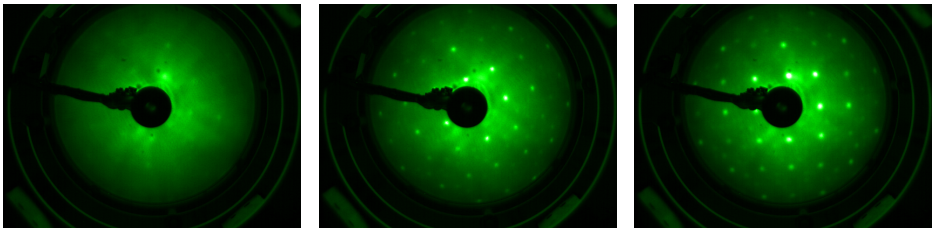

(a) LEED performed at 200 eV of sample 230ab (edged Mn excess)

(b) LEED performed at 200 eV of sample 224ab (top Mn excess)

(c) LEED performed at 200 eV of sample 233ab (centered Mn excess)

Figure 6.6: LEED measurements of the stoichiometric gradient samples 230ab, 224ab and 233ab

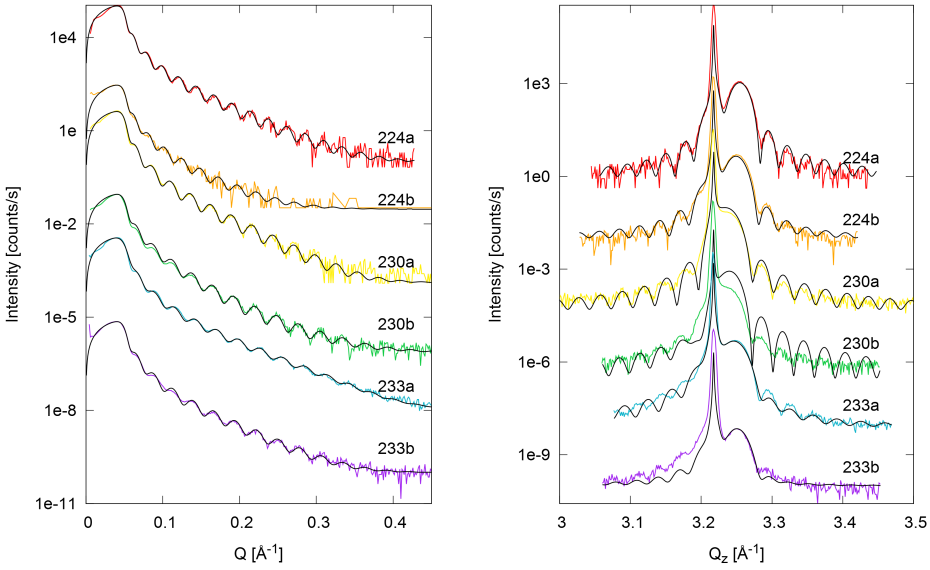

(a) XRR data and fits of the stoichiometric gradient samples

(b) XRD data and simulations of the stoichiometric gradient samples

Figure 6.7: Structural characterization of stoichiometric gradient samples via XRR and XRD; measurements shifted in intensity for clarification

Table 6.3: Parameters for XRR fits with d layer thickness and σ layer roughness used in fig. 6.7a

Sample name		224a	224b	230a	230b	233a	233b
Capping layer	SLD-δ [10^{-6}Å^{-2}]	14.48	14.42	12.44	22.23	13.44	15.23
	SLD-δ error [10^{-6}Å^{-2}]	0.79	2.62	1.31	11.21	1.29	3.53
	d [Å]	$2 * 10^{-05}$	10.7	0.0001	8.1	1.0	17.8
	d error [Å]	11.5	22.9	9.9	12.1	10.8	22.0
	σ [Å]	5.2	5.5	5.7	8.1	4.5	5.2
	σ error [Å]	0.6	1.8	0.9	1.7	0.7	1.0
LSMO layer	d [Å]	257.4	236.6	224.3	209.6	212.2	200.5
	d error [Å]	11.8	22.9	9.8	9.6	10.7	22.3
	σ [Å]	30.7	23.3	25.3	2.9	20.9	13.4
	σ error [Å]	5.6	8.3	3.8	9.6	3.6	10.5
STO substrate	roughness [Å]	4.4	5.1	5.4	4.9	5.9	5.3
	roughness error [Å]	3.1	6.5	3.1	3.0	3.5	1.6

Table 6.4: 224, 230, 233: Parameters for XRD fits used in fig. 6.7b (c out-of-plane lattice parameter, d crystalline layer thickness; error bars for d 1 Å, for c 0.001 Å)

Sample name	a		b	
	c [Å]	d [Å]	c [Å]	d [Å]
224	3.858	234	3.862	222
230	3.875	205	3.875	210
233	3.860	190	3.858	210

Chapter 7

Analysis of samples with nominally graded stoichiometry

7.1 PNR fitting

7.1.1 PNR fitting: MBE recipe-based model

The gradient samples were investigated via PNR to measure the stoichiometric gradient influence on the magnetic profile to determine the effect of the Mn-enriched structures onto the LSMO film. Measurements were performed in magnetic saturation at 5 K and 1.2 T (after field-cooling at 1.2 T) to determine the maximum magnetization in these layers and additionally in saturation at 300 K and 0.1 T to measure the potential proximity effects of section 2.1.

A good fit has a reasonable low amount of parameters, follows the finge damping and the SLD profile makes sense in terms of physics.

While XRR gives the total layer thickness and density, the PNR data show for LSMO and STO the magnetic profile but not the total layer thickness due to nearly identical nuclear SLD, see fig. 2.5 on page 21. Additionally, neutrons in comparison with X-rays provide with less intensity, therefore less Q range. So X-rays give a more detailed information on the nuclear structure, but lack in magnetic information. Therefore, PNR and XRR data were fitted simultaneously via GenX [90].

In fig. 6.5g, the theoretical local stoichiometries are displayed, which have been implemented in the MBE growth recipes. This local stoichiometry information was used to construct a model sample for simulation for the combined neutron and X-ray fit via the model in fig. 7.1a. This model takes the maximum and minimum concentration in fig. 6.5g as concentration for a layer. In fig. 6.5g, one sees the exponential increase/decrease of the concentration. This is taken into account via the exponential-rather than a standard Gaussian type of roughness of the different layers; combined with roughness σ for the lower layers of the same order of magnitude as the layer thickness to simulate the stoichiometric gradient with the least number of parameters possible to replicate that shape. The resulting stoichiometry was checked via the SLD profile visualization in the GenX program; since Mn has a negative SLD, the inverted profile of fig. 6.5g was the required outcome for the SLD profiles. The recipe-based stoichiometry was fixed, and only roughness, magnetization and density of the capping layer was fitted. The fitted neutron data are shown in fig. 7.1 and 7.2; the inserts show the corresponding XRR fit.

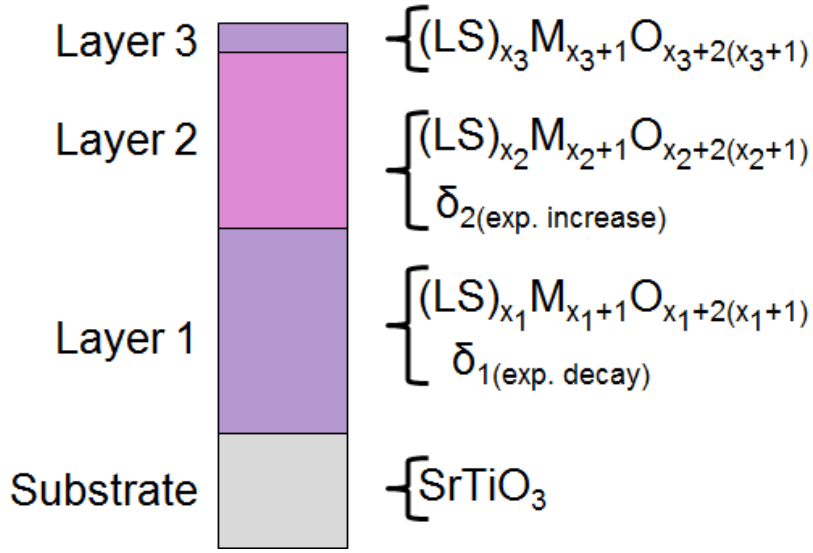

(a) Recipe-based model: Based on recipe x is creating the maximum or minimum Mn excess; stoichiometry process between these extrema is realized by exponential roughness forming the profiles of fig. 6.5g (p. 64)

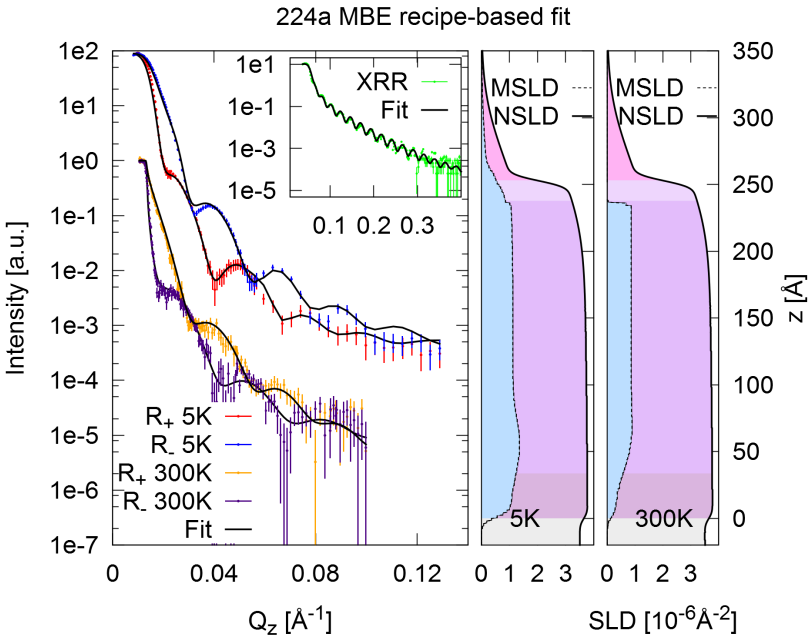

(b) Sample 224a (top Mn excess), 5K measured at MARIA@MLZ, 300K at MR@SNS: Mn negative SLD - reduced SLD on top indicates more Mn on top because of negative nuclear SLD of Mn

Figure 7.1: Recipe-based neutron fits: 300K and 5K with identical nuclear sublayer thicknesses, magnetic SLD varied (inserts show XRR data and fits)

Table 7.1: Parameters for 224 PNR fit - recipe-based model (Fit 11a, FOM: 9.9888e-02)

	Sublayer	d ($d_{errorbar}$) [Å]	σ ($\sigma_{errorbar}$) [Å]	LS:M	O conc.	Magnetism
NSLD	top	14.974 (-4e-03, 5e-03)	39.998 (-8e-03, 2e-03)	1:1.5	3.962 (-2e-03, 8e-03) -	
	$LSMO_2$	0	3.7307 (-7e-04, 3e-04)	1:1.5	3.00003 (-0.3e-04, 9.7e-04)	-
	$LSMO_1$	253.14(-4e-02, 6e-02)	126.557 (-6e-03, 3e-03)	1:1.125	2.43754 (-0.4e-04, 1.6e-04)	-
	Substrate	-	3.9299 (-5.1e-03, 0.1e-03)	-	-	-
MSLD 5K	M_3	18.127 (-6e-03, 3e-03)	7.174 (-4e-03, 6e-03)	-	-	2.0294 (-1.2e-03, 0.6e-03)
	M_2	169.73 (-4e-02, 6e-02)	0.775 (-5e-03, 5e-03)	-	-	2.464 (-4e-03, 6e-03)
	M_1	28.385 (-5e-03, 5e-03)	18.491 (-1e-03, 8e-03)	-	-	3.499 (-9e-03, 1e-03)
	M_0	36.898 (-8e-03, 2e-03)	17.636 (-6e-03, 3e-03)	-	-	2.2598 (-9.8e-03, 0.2e-03)
	Substrate	-	3.9299 (-5.1e-03, 0.1e-03)	-	-	-
MSLD 300K	M_3	18.127 (-6e-03, 3e-03)	7.174 (-4e-03, 6e-03)	-	-	0.000176 (-5e-06, 4e-06)
	M_2	169.73 (-4e-02, 6e-02)	0.775 (-5e-03, 5e-03)	-	-	1.892 (-2e-03, 3e-03)
	M_1	28.385 (-5e-03, 5e-03)	18.491 (-1e-03, 8e-03)	-	-	2.214 (-4e-03, 6e-03)
	M_0	36.898 (-8e-03, 2e-03)	17.636 (-6e-03, 3e-03)	-	-	0.602 (-2.2e-03, 0.8e-03)
	Substrate	-	3.9299 (-5.1e-03, 0.1e-03)	-	-	-

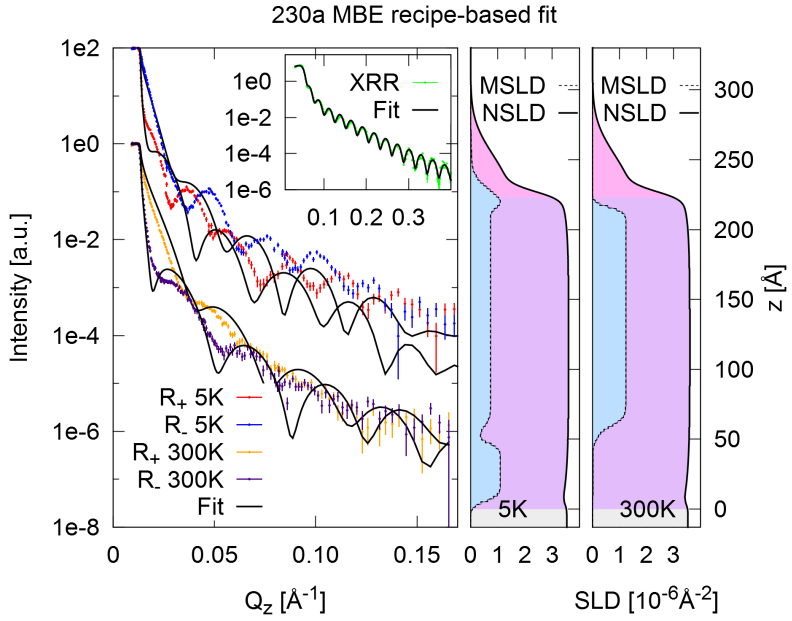

(a) Sample 230a (edged Mn excess): 5K and 300K measured at MR@SNS

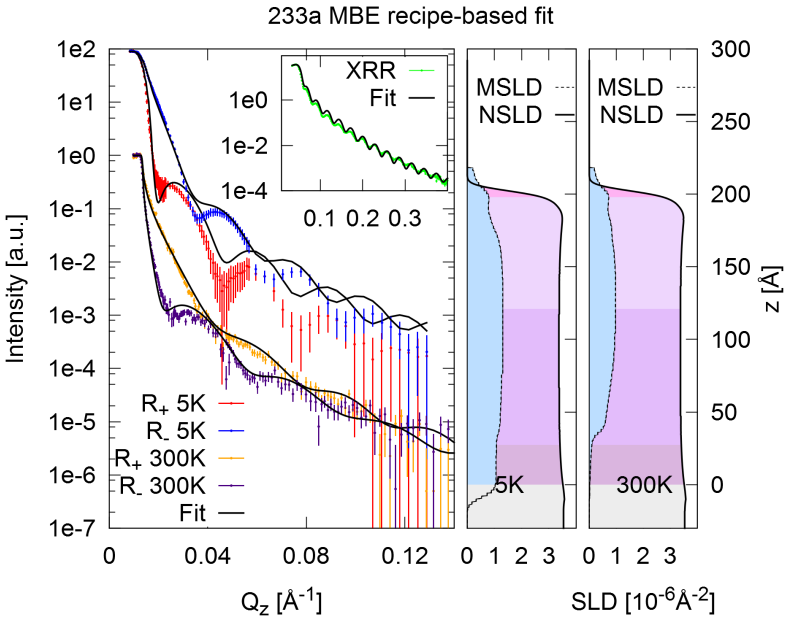

(b) Sample 233a (centered Mn excess): 5K measured at MARIA@MLZ, 300K at MR@SNS

Figure 7.2: Recipe-based neutron fits: 300K and 5K with identical nuclear sublayer thicknesses, magnetic SLD varied (inserts show XRR data and fit)

Table 7.2: Parameters for 233 PNR fit - MBE recipe model (Fit 05; FOM: 1.2973e-01)

	Sublayer	d ($d_{errorbar}$) [Å]	σ ($\sigma_{errorbar}$) [Å]	LS:M	Magnetism
NSLD	top	8 (-0.3e+01, 2.6e+01)	3.3 (-3e-01, 2e+01)	1:1.125	-
	$LSMO_3$	0	5 (-2, 4)	1:1.125	-
	$LSMO_2$	204.0 (-1e+01, 3e+01)	20.4	1:1.5	-
	$LSMO_1$	0	20.4	1:1.125	-
	Substrate	-	3.992 (-2.000e+00, 0.004e+00)	-	-
$MSLD_{5K}$	top	22 (-0.06e+02, 1.07e+02)	23 (-2.0e+01, 0.7e+01)	-	2.7 (-2.7e+00, 0.3e+00)
	M_3	116 (-1e+01, 3e+01)	3 (0, 3e+01)	-	2.89 (-2.83e+00, 0.06e+00)
	M_2	22 (-0.06e+02, 1.07e+02)	28 (-2.5e+01, 0.2e+01)	-	2.6 (-2.6e+00, 0.4e+00)
	M_1	44 (-4e+01, 4e+01)	3.03 (-0.001e+01, 2.660e+01)	-	2.3 (-2.3e+00, 0.6e+00)
	Substrate	-	3.992 (-2.000e+00, 0.004e+00)	-	-
$MSLD_{300K}$	top	22 (-0.06e+02, 1.07e+02)	23 (-2.0e+01, 0.7e+01)	-	2.4 (-2.4e+00, 0.6e+00)
	M_3	116 (-1e+01, 3e+01)	3 (0, 3e+01)	-	2.2 (-2.2e+00, 0.8e+00)
	M_2	22 (-0.06e+02, 1.07e+02)	28 (-2.5e+01, 0.2e+01)	-	0.9 (-0.9e+00, 2.1e+00)
	M_1	44 (-4e+01, 4e+01)	3.03 (-0.001e+01, 2.660e+01)	-	0.026 (-0.02e+00, 2.95e+00)
	Substrate	-	3.992 (-2.000e+00, 0.004e+00)	-	-

Table 7.3: Parameters for 230 PNR fit - MBE reciple model (Fit 05) - FOM: 1.8686e+03

	Sublayer	d ($d_{errorbar}$) [Å]	σ ($\sigma_{errorbar}$) [Å]	LS:M	Magnetism
NSLD	top	26.2774 (-3e-04, 6e-04)	20.0002 (-0.2e-03, 2.8e-03)	1:1.5	-
	$LSMO_3$	0	4.736 (-6e-03, 4e-03)	1:1.5	-
	$LSMO_2$	223.08 (-0.06e+00, 6.33e+00)	22.3	1:1.125	-
	$LSMO_1$	0	22.3	1:1.5	-
	Substrate	-	3.4796 (-6e-04, 4e-04)	-	-
$MSLD_{5K}$	top	12.7697 (-9.5-03, 0.2e-03)	8.128 (-8e-03, 2e-03)	-	2.923 (-3e-03, 7e-03)
	M_3	156.414 (-4e-03, 4e-03)	3.005 (-5e-03, 5e-03)	-	1.625 (-5e-03, 5e-03)
	M_2	12.764 (-4e-03, 4e-03)	5.02 (-2e-02, 3e-02)	-	0.6555 (-5e-04, 5e-04)
	M_1	41.067 (-7e-03, 3e-03)	3.027 (-7e-03, 3e-03)	-	2.40002 (-0.2e-04, 3.7e-04)
	Substrate	-	3.4796 (-6e-04, 4e-04)	-	-
$MSLD_{300K}$	top	12.7697 (-9.5-03, 0.2e-03)	8.128 (-8e-03, 2e-03)	-	0.00141 (-0.1e-04, 1.9e-04)
	M_3	156.414 (-4e-03, 4e-03)	3.005 (-5e-03, 5e-03)	-	2.7267 (-4.3e-03, 0.1e-03)
	M_2	12.764 (-4e-03, 4e-03)	5.02 (-2e-02, 3e-02)	-	0.30006 (-0.4e-04, 1.345e-04)
	M_1	41.067 (-7e-03, 3e-03)	3.027 (-7e-03, 3e-03)	-	0.02498 (-7e-05, 2e-05)
	Substrate	-	3.4796 (-6e-04, 4e-04)	-	-

Sample 224a (top Mn excess) was modeled according to the recipe used in fig. 6.5c (p. 64). The fit needed to be equipped with additional oxygen concentration parameters for each sublayer, and an additional capping layer for a successful fit. The fit result is displayed in fig. 7.1b, the used parameters are shown in tab. 7.1. The grey part in the SLDs represents the substrate.

The capping layer has an alike layer thickness (inside the errorbars) compared to the one used for the Plot-Script simulation, see tab. 6.3. The small difference is partly an effect of the different technique of simulating the layer structure of GenX ("slicing"), but also related to the now included neutron data. Additionally, the roughness is 2.66 times higher than the thickness. While every sublayer has a higher magnetization at 5K than at 300K, at 300K the capping layer seems to be more magnetic than the layer directly underneath. The oxygen concentration is extremely low in the fit; the 2nd layer has an oxygen concentration of 2.44 oxygen atoms per unit cell instead of 3.25, the expected value for the saturated sample due to the additional MnO_x layers. A so drastically reduced oxygen concentration seems not likely with respect to the via XRD determined lattice parameters in tab. 6.4, but the resulting fit in fig. 7.1b simulates the data well.

Sample 230a (edged Mn excess) was modeled in fig. 7.2a according to the MBE recipe via a bottom layer with an exponential decaying roughness and zero thickness, then layer 2 with the total layer thickness and layer 3 again zero thickness, but the exponential roughness type pointing inside the top layer, see tab. tab:233afit05. In agreement with the first analysis XRR fit parameters in tab. 6.3, an additional capping layer was modeled. This approach did not work at all. The main issue, which could not be simulated properly, was the additional kink in the R_- channel at 0.02Å^{-1} at 5 K. The total layer thickness gained by XRR data is consistent with the PNR data for 300 K, but for 5 K, significantly higher layer thickness is needed. The substrate is undergoing a phase transition from cubic to tetragonal near 110 K, which transforms the lattice parameters by 0.2 % [91]. Even if every single unit cell inside the substrate transformed into elongating towards "longer out-of-plane, shorter in-plane" to have the maximum impact onto the thin film on top, this could not explain the approximately 30 % thicker thin film measured at 5 K.

Sample 233 (centered Mn excess) should contain more Mn in the middle of the layer. Again, the neutron data at 5 K in fig. 7.2b could not be fitted via the parameters in tab. 7.2; the magnetization and total layer thickness match roughly. For R_+ at the first minimum the fit is below the data, on the second minimum the fit is above the date. For R_- additionally the minimum Q_z positions do not fit, they are out of phase. Again, the 5 K fitting should be straight forward.

Obviously the recipe-based models do not fit the neutron data for sample 230 and 233. For sample 224 (top Mn excess) a drastically reduced oxygen concentration had to be introduced. Searching for an alternative description, the model of sample 224, i.e. with LS_1M_1O at the substrate and increasing MnO content towards the surface can be tried for the other samples, since the only non-fitted parameter so far was the sample stoichiometry.

7.1.2 PNR fitting: Surface particle model

Scattering methods provide with information of the whole sample. In specular reflectivity geometry, the out-of-plane information is depth-resolved while the in plane information is averaged. To show the influence of different local features in a thin film sample, sketches are given

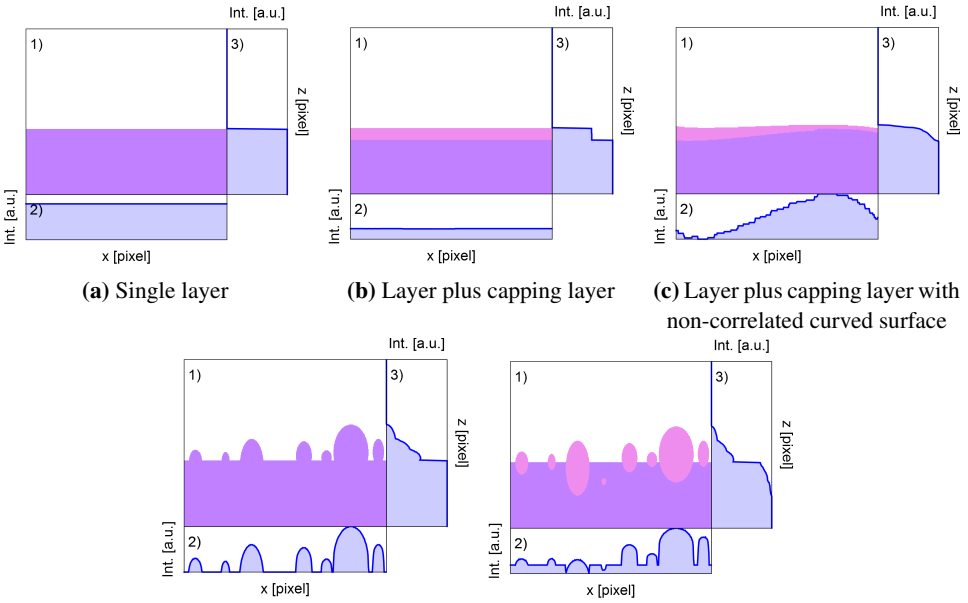

(a) Single layer

(b) Layer plus capping layer

(c) Layer plus capping layer with non-correlated curved surface

(d) Layer with droplets consisting of same material

(e) Layer with droplets consisting of different material

Figure 7.3: Visualization of thin film cross section; comparison of different local informations; 1) Visualization itself, 2) averaged density for each column, 3) averaged density for each row

in fig. 7.3. For clarification, the substrate was not taken into account but only the layer was considered. The material density is summed up in x and z direction.

In fig. 7.3a, a perfect layer is displayed. The interface layer/vacuum is flat; the sum-up over z shows a clear step function, while the sum-up over x is constant. In fig. 7.3b, a second layer with a smaller density is on top of the original layer, leading to a second step in averaged z with a still constant averaged x value. For fig. 7.3a and 7.3b, the Parratt algorithm [25] is applicable to be able to compare it with scattering methods due to a non-existing roughness and distinguishable layer densities.

In fig. 7.3c to 7.3e, the top and bottom layer show different kinds of uncorrelated roughness. While in fig. 7.3c the top layer material preferentially fills the holes of the bottom layer, fig. 7.3d shows a high surface roughness and in fig. 7.3e droplets of the top layer material are embedded in the bottom layer. While the averaged x curves look very different, a clear distinction between the different local features inside the visualizations is no longer that easy, if only the averaged profile information is available. In this case for the top layer the roughness is in the same order of magnitude as the thickness, the Parratt formalism is no longer applicable; via slicing which was introduced in section 2.2.2, one can fit the reflectivity profiles. However the local features in fig. 7.3c, 7.3d and 7.3e cannot be distinguished with specular reflectometry.

To test whether more MnO could be on top of every sample - a rather unlikely event which would contradict the recipe-based stoichiometry and observation of RHEED intensity oscillation - the surface particle model was applied onto sample 230 (edged Mn excess) and 233

(centered Mn excess). This model is visualized in fig. 7.4a. For every sample a bottom layer at the substrate has a stoichiometry of LS_1:M_1, a rising MnO content towards the surface is implemented via layer 2 with more Mn than inside the bottom layer and layer 3 with even more Mn than in layer 2. The capping layer is considered as constant in fig. 7.4a in order to emphasize the rather different structure below the capping layer inside the simulation.

The surface particle model was used to fit sample 233a (centered Mn excess) in fig. 7.4b, the corresponding fitting parameters are shown in fig. 7.7. The trend of the scattering length density has now opposite behavior to that of before; instead of a higher nuclear scattering length density (NSLD) for the film surface, the NSLD decreases in the top region. This is due to the different Mn content compared to the values used in fig. 7.2. Again, the fit shows a higher magnetization at 5 K than at 300 K.

For sample 230a (edged Mn excess) in fig. 7.4c, the total layer thickness of neutron data at 5 K and of X-ray data (measured at 300 K) does not fit; the 5 K data fit needs a roughly 60 Å thicker layer than the X-ray data, which is one third of the total layer thickness. This cannot be explained by any STO tetragonal-to-cubic phase transformation (see section 2.1.1) nor by the dilatation due to the temperature difference (which, by the way, would be negative instead of positive). Still, this fit fits better than the recipe-based fit in fig. 7.2a.

To reach 5 K, before starting to cool down, a vacuum of 10^{-6} Torr or better is applied onto the used cryostat. During the cooling down process, a small leakage might have introduced air into the cryostat, but due to the only minor leakage, the pressure did not spike up. It is possible that the air, which is relatively dry here, could have condensated at the sample holder and sample surface.

The very dry room conditions make a water layer seem unlikely. Additionally, water has a negative SLD (-0.5*10^{-6}Å^{-2}), while a positive SLD is needed. Therefore water was eliminated as a material candidate immediately. The two major components inside air are nitrogen and oxygen. In fig. 7.4c fits for oxygen and nitrogen as capping layer material are displayed, the fitting parameters are in tab. 7.7 (oxygen), tab. 7.6 (nitrogen) and tab. 7.5 (vacuum). These candidates have different melting and boiling temperatures (oxygen having the higher ones) and additionally, nitrogen is diamagnetic, while oxygen is paramagnetic above 50K and antiferromagnetic below [71]. Therefore, the frozen gas layer was determined to consist mainly of oxygen.

The shape of the magnetic profile below the ice layer is unfortunately no longer identifiable: The structural profile seems more likely with the surface particle model. But due to the frozen layer growing over time and the neutron measurement being performed at 3 different sample and detector positions, for the high-Q part, the frozen gas layer should be larger than the front part. Therefore, the magnetic profile below the frozen gas layer is no longer uniquely identifiable. On the other hand, the nuclear surface particle model is definitively needed, see the kink in the SLD profile around z=200 Å. To perform a reference measurement on what was intended from the MBE recipe to be proposed constant $(LS)_1M_1O$ structure, sample 301a was measured at the polarized neutron reflectometer TREFF@MLZ. The measurements were performed after cooling-down in 0.7 T at 5 K and 0.7 T. For a better comparability, the used fitting parameters for all 5 fits are listed in tab. 7.8. The constant stoichiometry approach was used in fit 5 (fig. 7.5e). This fit requires a capping layer of arbitrary density to simulate rough, but still $(LS)_1M_1O$ inside air. The fitting algorithm requires a weird kink in the magnetic structure and the XRR pattern is not fitted well. The deviating fit at the first few fringes ($Q < 0.1$Å^{-1}) is a sign for continuity problem issues adressed by Tolan [27].

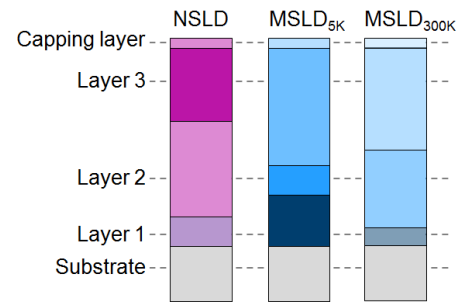

(a) Sketch of different layer structures used for fitting in surface particle model

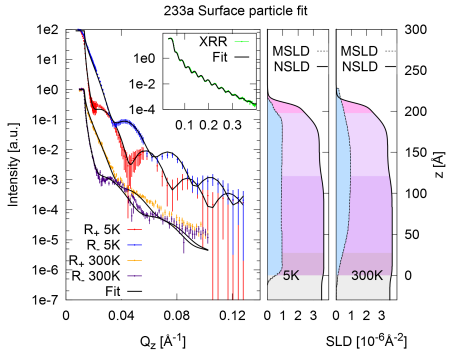

(b) 233a (centered Mn excess) fitted with surface particle model (5K measured at MARIA@MLZ, 300K at MR@SNS)

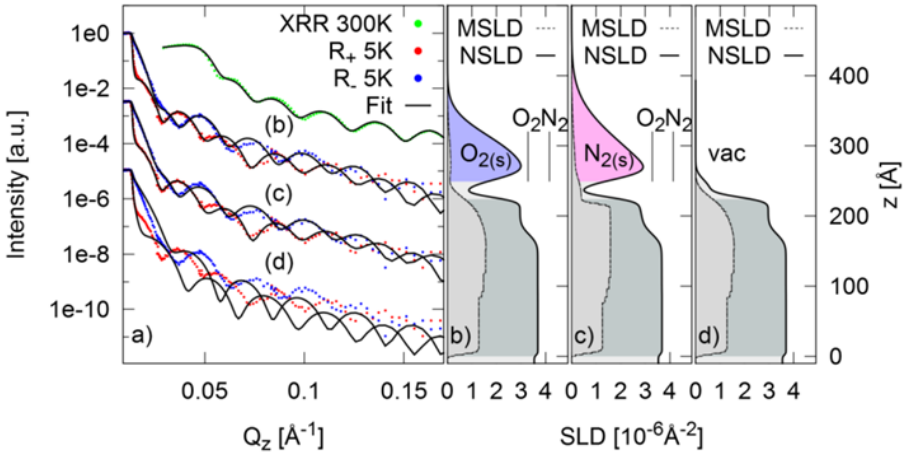

(c) 230a: Comparison of different frozen gases; taken with permission from [92]

Figure 7.4: Surface particle model applied on samples 233a (centered Mn excess) and 230a (edged Mn excess)

Table 7.4: Parameters for 233 PNR fit - surface particle model in fig. 7.4b - FOM: 7.8567e-02

	Sublayer	d ($d_{errorbar}$) [Å]	σ ($\sigma_{errorbar}$) [Å]	LS:M (LS:$M_{errorbar}$)	Magnetism
NSLD	top	14.96(-5e-02, 4e-02)	3.77 (-6e-02, 3e-02)	0.9995 (-5e-04, 5e-04)	-
	$LSMO_3$	77.1 (-1e-01, 8e-01)	13.266 (-6e-03, 4e-03)	0.5742 (-2e-04, 8e-04)	-
	$LSMO_2$	93.2(-2e-01, 8e-01)	14.2 (-1e-01, 3e-01)	0.50008 (-8e-05, 2e-05)	-
	$LSMO_1$	27.93 (-9.3e-01, 0.7e-01)	6.175 (-0.5e-02, 2.4e-02)	0.5 (fixed)	-
	Substrate	-	5.67 (-7e-02, 3e-02)	-	-
$MSLD_{5K}$	top	14.96(-5e-02, 4e-02)	3.008 (-8e-03, 2e-03)	-	0.763 (-3e-03, 7e-03)
	M_3	77.1 (-1e-01, 8e-01)	5.28 (-3e-02, 2e-02)	-	2.18 (-8e-02, 2e-02)
	M_2	93.2(-2e-01, 8e-01)	24.78 (-0.8e-01, 1.2e-01)	-	1.993 (-1.3e-02, 0.7e-02)
	M_1	27.93 (-9.3e-01, 0.7e-01)	30.487 (-9.54e-01, 0.07e-01)	-	1.844 (-4e-03, 6e-03)
	Substrate	-	5.07 (-1.6e-01, 0.3e-01)	-	-
$MSLD_{300K}$	top	14.96(-5e-02, 4e-02)	4.013 (-1.3e-02, 0.7e-02)	-	0.1066 (-6e-04, 3e-04)
	M_3	77.1 (-1e-01, 8e-01)	32.43 (-3e-02, 7e-02)	-	2.328 (-8e-03, 2e-03)
	M_2	93.2(-2e-01, 8e-01)	37.424 (-4e-03, 6e-03)	-	1.91 (-1e-02, 9e-02)
	M_1	27.93 (-9.3e-01, 0.7e-01)	24.895 (-9.3e-02, 0.4e-02)	-	0.0003 (-3e-04, 1e-04)
	Substrate	-	5.07 (-1.6e-01, 0.3e-01)	-	-

Table 7.5: Parameters for 230 PNR fit - surface particle model (Fit V; FOM 2.1136e-01)

	Sublayer	d ($d_{errorbar}$) [Å]	σ ($\sigma_{errorbar}$) [Å]	LS:M (LS:$M_{errorbar}$)	Magnetism
NSLD	top	25.094 (-4e-03, 5e-03)	9.894 (-4e-03, 5e-03)	0.99998 (-9.8e-04, 0.2e-04)	-
	$LSMO_3$	52.92 (-2e-02, 8e-02)	5.376 (-0.5e-02, 1.4e-02)	0.68304 (-0.3e-04, 9.6e-04)	-
	$LSMO_2$	81.197 (-7e-03, 3e-03)	10.645 (-5e-03, 5e-03)	0.50104 (-0.4e-04, 9e-04)	-
	$LSMO_1$	90.9452 (-4e-02, 5e-02)	6.289 (-9e-03, 1e-03)	0.5	-
	Substrate	-	2.3597 (-9.6e-03, 0.3e-03)	-	-
$MSLD_{5K}$	top	25.094 (-4e-03, 5e-03)	9.894 (-4e-03, 5e-03)	-	0.00403 (-3e-05, 1e-05)
	M_3	28.24002 (-0.2e-04, 2.8e-04)	12.689 (-0.9e-02, 1.1e-02)	-	2.257 (-0.07e-01, 2.40e-01)
	M_2	106.67 (-5e-02, 5e-02)	20.0082 (-2e-04, 8e-04)	-	3.495 (-4e-03, 5e-03)
	M_1	90.15 (-5e-02, 5e-02)	28.829 (-9e-03, 1e-03)	-	2.7497 (-7e-04, 3e-04)
	Substrate	-	2.3597 (-9.6e-03, 0.3e-03)	-	-
$MSLD_{300K}$		top 25.094 (-4e-03, 5e-03)	9.894 (-4e-03, 5e-03)	-	0.6485 (-5e-04, 5e-04)
	M_3	28.24002 (-0.2e-04, 2.8e-04)	12.689 (-0.9e-02, 1.1e-02)	-	1.8655 (-2e-04, 5e-04)
	M_2	106.67 (-5e-02, 5e-02)	20.0082 (-2e-04, 8e-04)	-	1.860 (-8e-03, 5e-03)
	M_1	90.15 (-5e-02, 5e-02)	28.829 (-9e-03, 1e-03)	-	0.1918 (-1e-04, 2e-04)
	Substrate	-	2.3597 (-9.6e-03, 0.3e-03)	-	-

Table 7.6: Parameters for 230 PNR fit - surface particle model (Fit N; FOM: 8.4801e-02)

	Sublayer	d ($d_{errorbar}$) [Å]	σ ($\sigma_{errorbar}$) [Å]	LS:M (LS:$M_{errorbar}$)	Magnetism
NSLD	Nitrogen	49.91 (-1e-02, 1e-02)	51.988 (-6.8e-02, 0.1e-02)		0.358 (-8e-03, 2e-03)
	top		9.896(-6e-03, 4e-03)	0.9992 (-2e-04, 8e-04)	-
	$LSMO_3$	52.989 (-9.8e-02, 0.1e-02)	5.376 (-6e-03, 3e-03)	0.6832 (-0.2e-03, 1.7e-03)	-
	$LSMO_2$	81.194 (-1.4e-02, 0.5e-02)	10.648 (-8e-03, 2e-03)	0.5012 (-2e-04, 3e-04)	-
	$LSMO_1$	90.006 (-1.6e-02, 0.3e-02)	6.289 (-9e-03, 1e-03)	0.5	-
	Substrate	-	2.572 (-2e-03, 8e-03)	-	-
$MSLD_{5K}$	top	25.092 (-1.1e-02, 0.8e-02)	9.896(-6e-03, 4e-03)	-	0.862 (-2e-03, 8e-03)
	M_3	10.344 (-4e-03, 6e-03)	17.014 (-4e-03, 6e-03)	-	0.972 (-2e-03, 3e-03)
	M_2	130.953 (-1.4e-02, 0.5e-02)	2.409 (-8e-03, 1e-03)	-	3.4999 (-9.0e-04, 0.7e-04)
	M_1	82.892 (-2e-03, 8e-03)	17.741 (-2e-03, 8e-03)	-	2.735 (-4e-03, 5e-03)
	Substrate	-	2.572 (-2e-03, 8e-03)	-	-
$MSLD_{300K}$	top	25.092 (-1.1e-02, 0.8e-02)	9.896(-6e-03, 4e-03)	-	0.6484 (-4e-04, 5e-04)
	M_3	10.344 (-4e-03, 6e-03)	17.014 (-4e-03, 6e-03)	-	1.8691 (-9.0e-03, 0.9e-03)
	M_2	130.953 (-1.4e-02, 0.5e-02)	2.409 (-8e-03, 1e-03)	-	1.8591 (-9.0e-03, 0.8e-03)
	M_1	82.892 (-2e-03, 8e-03)	17.741 (-2e-03, 8e-03)	-	0.191 (0.000e+00, 1e-03)
	Substrate	-	2.572 (-2e-03, 8e-03)	-	-

Table 7.7: Parameters for 230 PNR fit - surface particle model (Fit O; FOM: 8.8178e-02)

	Sublayer	d (d$_{errorbar}$) [Å]	σ ($\sigma_{errorbar}$) [Å]	LS:M (LS:M$_{errorbar}$)	Magnetism
NSLD	Oxygen	62.678 (-7e-03, 2e-03)	29.86 (-5.6e-02, 0.3e-02)		0.1964 (-4e-04, 6e-04)
	top	25.07 (-7e-02, 3e-02)	9.895 (-5e-03, 4e-03)	0.9993(-2e-04, 7e-04)	-
	$LSMO_3$	52.94 (-4e-02, 1e-02)	5.377 (-6e-03, 3e-03)	0.682 (-2e-03, 8e-03)	-
	$LSMO_2$	81.196 (-6e-03, 4e-03)	10.649 (-9.3e-03, 0.6e-03)	0.5002 (-0.2e-03, 1.8e-03)	-
	$LSMO_1$	90.997 (-7e-03, 3e-03)	6.2898 (-8e-04, 2e-04)	0.5	-
	Substrate	-	2.352 (-2e-03, 7e-03)	-	-
$MSLD_{5K}$	top	25.07 (-7e-02, 3e-02)	9.895 (-5e-03, 4e-03)	-	0.00401 (-1e-05, 9e-05)
	M_3	28.24 (-3e-02, 6e-02)	12.686 (-6e-03, 4e-03)	-	2.2497 (-7e-04, 3e-04)
	M_2	106.69 (-3e-02, 6e-02)	20.007 (-6e-03, 3e-03)	-	3.499 (-8e-03, 1e-03)
	M_1	90.2 (-1.6e-01, 0.4e-01)	28.825 (-5e-03, 5e-03)	-	2.749 (-9.1-03, 0.8e-03)
	Substrate	-	2.352 (-2e-03, 7e-03)	-	-
$MSLD_{300K}$	top	25.07 (-7e-02, 3e-02)	9.895 (-5e-03, 4e-03)	-	
	M_3	28.24 (-3e-02, 6e-02)	12.686 (-6e-03, 4e-03)	-	
	M_2	106.69 (-3e-02, 6e-02)	20.007 (-6e-03, 3e-03)	-	
	M_1	90.2 (-1.582e-01, 0.4e-01)	28.825 (-5e-03, 5e-03)	-	
	Substrate	-	2.352 (-2e-03, 7e-03)	-	-

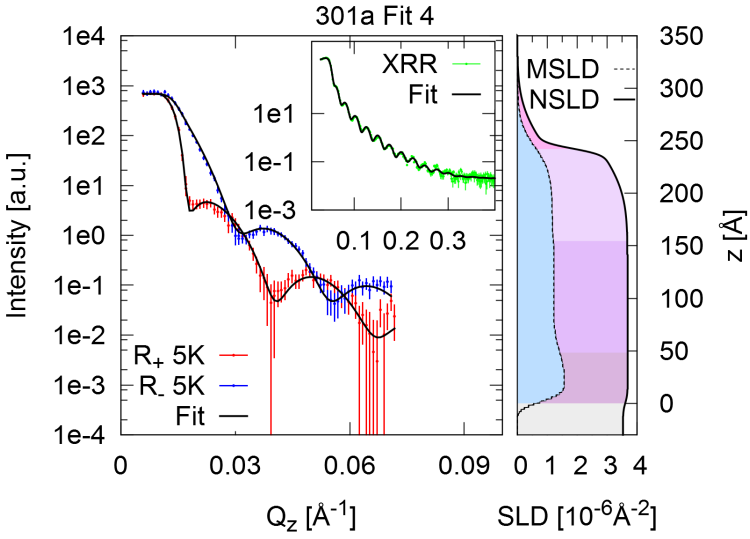

(a) Best fit (Fit 04)

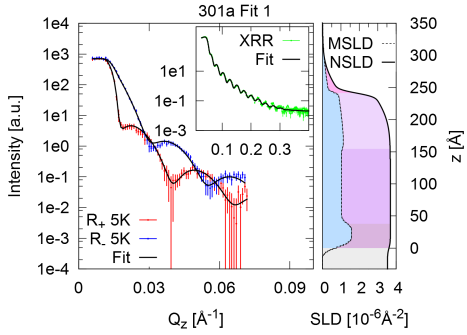

(b) Fit 01: Surface particle model, all parameters fitted

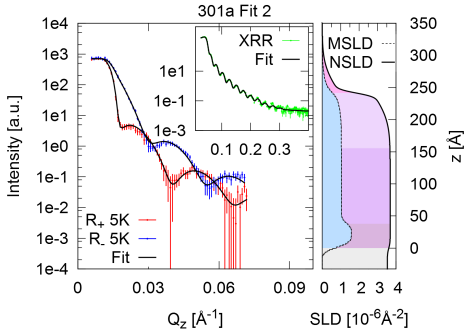

(c) Fit 02: Step-wise ecreasing magnetism towards surface

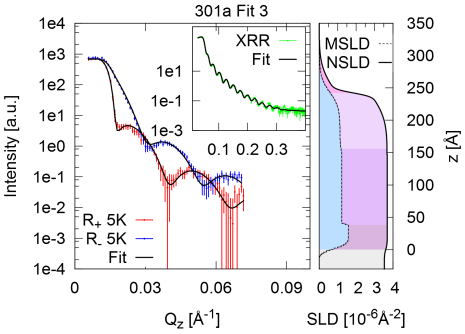

(d) Fit 03: Small magnetic roughness

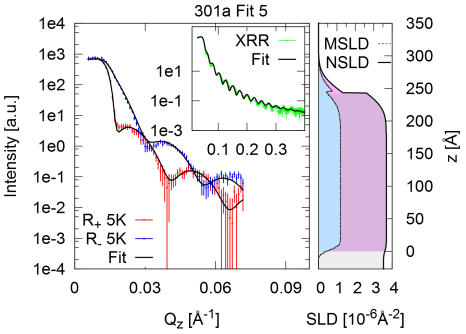

(e) Fit 05: Constant LS_1M_1O

Figure 7.5: Comparison of influence of different models for fitting the 301a measured at TREFF@MLZ

Table 7.8: Parameters for 233 PNR fit - surface particle model (Fit 12)

Layer	Parameter	Fit01	Fit02	Fit03	Fit04	Fit05
$LSMO_{top}$	d	0.08	0.04	0.2	0.3	3
	σ	34.2	34.1	31.7	33.6	21.1
	δ	0.0087	0.0088	0.00868	0.009	0.0112
	concLS:M	0.6	0.630	0.600	0.600	0.5
	M_{top}	1.43	1.41	1.37	1.43	0.84
	$\sigma(M_{top})$	50.0	26.6	25.3	26.3	26.4
$LSMO_3$	d	87	86	86	88	0.0
	σ	4.6	4.6	4.5	4.5	0.0
	concLS:M	0.528	0.531	0.539	0.523	0.5
	M_3	2.59	2.30	2.50	2.58	0.0
	$\sigma(M_3)$	2.8	7.8	13.7	14.6	0.0
$LSMO_2$	d	117	118	118	106	0.0
	σ	0.5	0.005	0.01	0.3	0.0
	concLS:M	0.51	0.517	0.521	0.500	0.5
	M_2	2.29	2.30	2.70	2.70	0.0
	$\sigma(M_2)$	5.6	7.3	6.7	5.7	0.0
$LSMO_1$	d	38	38	38	48	242
	σ	0.001	1.0	0.0001	7.0	2.1
	concLS:M	0.5	0.5	0.5	0.5	0.5
	M_1	3.4995	3.50	3.50	3.50	2.64
	$\sigma(M_1)$	5.2	5.7	0.5	14.4	18.1
Substrate	σ	6.5	6.5	6.0	6.1	5.6
FOM		6.27e-02	6.31e-02	6.50e-02	6.63e-02	9.03e-02

Therefore, fits using the surface particle model were tested here, too. The magnetic model was changed and the resulting fits were plotted. The most likely candidate is fit 4, which is shown enlarged in fig. 7.5a.

Fit 1 (fig. 7.5b) was the fit produced by GenX while setting all parameters free. There, an enhanced magnetism at the interface is simulated, followed by a lower magnetism region, after which a slightly higher magnetization value is used in layer 3. For all simulations, the capping layer is magnetic with a magnetic SLD in the order of the nuclear SLD value.

For fit 2 in fig. 7.5c, the magnetization of the different sublayer was set in a way that the interface magnetization still is larger than the magnetization afterwards, but that the layer 3 has a slightly smaller magnetization than layer 2. In fit 3 (fig. 7.5d), the impact of the magnetization roughness was investigated by giving the largest difference - between layer 1 and 2 - a sharp interface.

Regarding the fits in fig. 7.5, the constant stoichiometry approach in fit 5 fits slightly less good than the other fits. Between fit 1 to fit 4, there is no significant influence of the different SLD profiles on the combined X-ray and neutron fits. Fit 4 seems to be most probable version, but only based on the PNR data there is no detailed analysis of the magnetic structure feasible. This is emphasized by the very small differences of the figure of merit for the different fits (tab. 7.8, last line). To investigate the nuclear structure further, TEM measurements were performed starting in section 7.2.

7.2 Electron microscopy

So far, all samples were characterized via scattering methods, namely in-situ RHEED and ex-situ LEED, XRR, XRD and PNR. All these scattering techniques only provide information in reciprocal space and average over the whole sample. To gain insight in real space and to verify the estimated quality, high-angle annular dark-field (HAADF) scanning transmission electron microscopy (STEM) measurements have been performed.

A remark concerning the visualization of TEM images

For TEM images, the standard display mode uses a grey color scale due to its high information density. In some publications, additional information gained via EELS [93] or EDX [94] or further data analysis like an FFT filtered image [95] is implemented by coloring special regions or atoms. Other groups highlight features in the TEM images by adding colors [96]. In this work, instead of coloring only certain features, a different base color scale "blue - white - red" was used (see fig. 7.7) additionally to the classical grey scale with higher intensity following the colors "black - grey - white" as in fig. 7.6. This color scale was chosen to emphasize the difference of features with neighboring intensities.

7.2.1 Overview images

Two samples were studied by STEM: Sample 230b (edged Mn excess) has an LSMO layer with nominally additional MnO_x layers concentrated at the surface and interface of the sample. Sample 301a was prepared as stoichiometric $(LS)_1M_1O_3$ sample in shuttered growth mode, therefore a pure perovskite LSMO layer was expected.

In fig. 7.6, HAADF STEM images of the lamella cross sections are shown. Due to the TEM preparation process described in section 3.10, several additional layers are visible: The bottom part consists of STO, followed by the thin LSMO layer. On top of the LSMO layer, there is Au conduction layer, above are the Pt protection layers.

In the following the layer region (marked by the orange rectangle) is examined in detail. In fig. 7.7, flat LSMO film areas can be identified. Additionally, in both samples at the interface of LSMO layer and Au capping layer, some defects are visible. In accordance to the SEM image of fig. 7.6a, these defects could resemble particles on top of the sample. The particles consist of MnO and appear darker than the rest because of the small nuclear charge density of MnO compared to the other involved materials. The finding of these particles is very intriguing and will be studied in section 7.10.

7.2.2 Flat film areas

Here, local details are discussed. For a quantification in terms of surface/interface roughness or mean lattice parameters of the samples, XRR and XRD (performed in sections 6.1 and 6.3) and are the methods of choice.

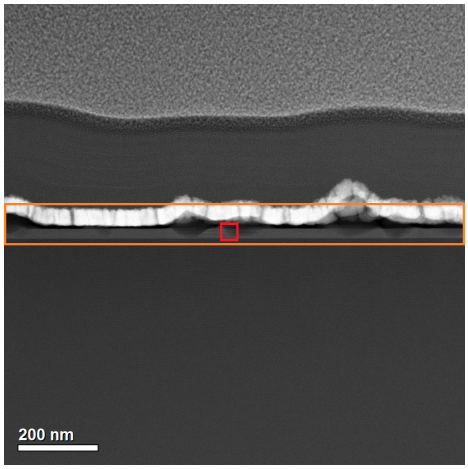

(a) TEM of sample 301a (pure LSMO), overview; the zoomed area of the red square is enlarged in fig. 7.10c, the orange area is enlarged in fig. 7.7a

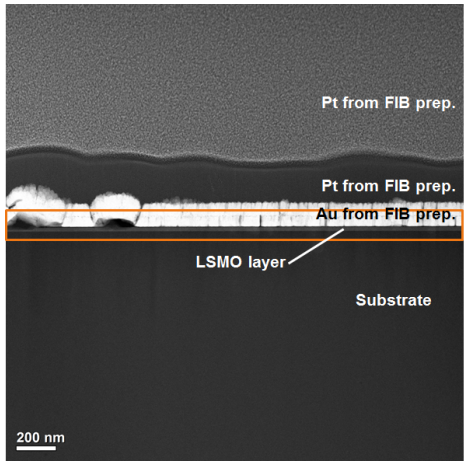

(b) TEM of sample 230b (edged Mn excess), overview; cut around layer (orange area) is shown in fig. 7.7b

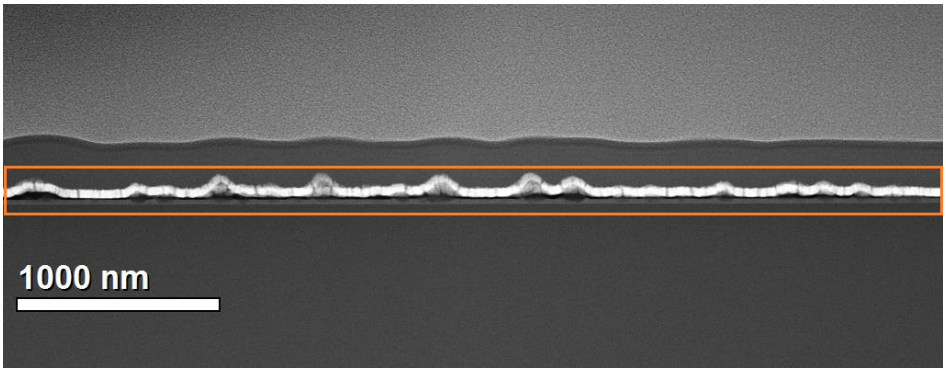

(c) TEM of sample 301a overview; cut around layer (orange area) is shown in fig. 7.7c

Figure 7.6: TEM: Overview images

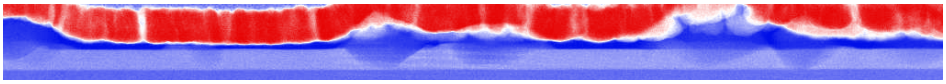

(a) TEM of sample 301a (pure LSMO), 1 μm long overview, colorcoded version area around the layer of fig. 7.6a

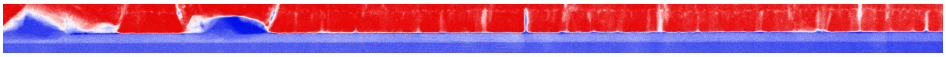

(b) TEM of sample 230b (edged Mn excess), 1.6 μm long overview, version around layer of fig. 7.6b colored

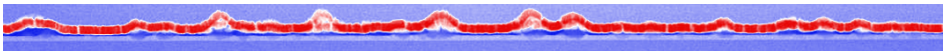

(c) TEM of sample 301a, 4.6 μm long overview, colored area around the layer in fig. 7.6c

Figure 7.7: TEM: Colored versions of layer regions of overview images in fig. 7.6

In fig. 7.8a, HAADF STEM images of layer and substrate of sample 301a (pure LSMO) are shown. Regarding the perovskite notation ABO_3, red and orange marked spots represent A atoms, blue spots are B atoms. The most intense spots in both images are associated to columns containing Sr and La/Sr atoms, respectively. The intensity scales of these images are identical. The higher HAADF intensity at the deposited layer is due to higher scattering power of the material. Indeed, the substrate consists of $_{38}$Sr, $_{22}$Ti and $_{8}$O while the layer is made of $_{57}$La, $_{38}$Sr, $_{25}$Mn and $_{8}$O. The unit cells appear to be not orthogonal; this seeming distortion is an artifact of the sequential image formation in scanning mode and stems from sample drift over the 20 s of image acquisition.

To further interpret the images of fig. 7.8a, Fourier transformations were performed via 2D-FFT routine of the microscopy data analysis program Gwyddion [97]. Fig. 7.8b and 7.8c show the Fourier transformation of the full image area. The well-defined spots point out the perfect delta-shaped distance distribution of all atomic distances. Streaks originating at the Fourier coefficients of high amplitude originate from scan distortions due to sample drift, inaccurate reproduction of scan positions in successive scan lines (scan noise), and from the aperiodic image content in the full area.

In fig. 7.9, neither Jahn-Teller distortions nor different Mn valencies - the most probable causes for distortions inside a LSMO film - could be detected. The STEM signal averages the 20-50 nm thick cross-section; inside this depth, there is no sign of Mn atoms at La/Sr positions. Neither half-plane dislocations nore grains with (110) displacement are detected. For larger sample thickness, the signal can be very delocalized due to a significant spreading of the convergent electron beam within the sample volume. Therefore the grey area between the dark STO and bright LSMO does not necessarily arise from an intermixing zone of that size.

In fig. 7.9a, sample 301a (pure $La_{2/3}Sr_{1/3}MnO_3$) is shown. A well-defined interface separates the LSMO layer from the STO substrate. No dislocations are visible within these images inside the LSMO areas. The shown area is defect-free.

Within sample 230b (edged Mn excess) in fig. 7.9c, due to the MBE recipe in fig. 6.5a, one expects 14 additional MnO_x layers each contributing a one atom thick rocksalt structure, which should be visible by eye in the high-resolution STEM images. Instead, one observes a perfect perovskite structure. Inside the well-ordered layer, there is no sign of any additional rock salt structure, and no vertical stoichiometric gradient nor vertical MnO_x structures. Between

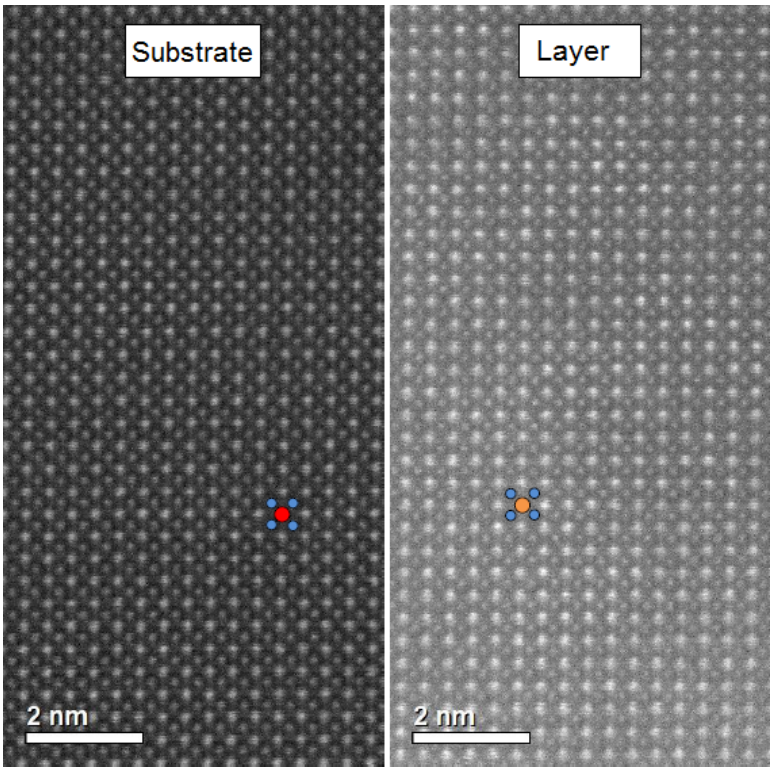

(a) HRTEM of $SrTiO_3$ substrate and $La_{2/3}Sr_{1/3}MnO_3$ layer area of sample 301a; red/orange marked atoms are A atoms in ABO_3 structure (here: La/Sr), blue are B atoms (here: Mn/Ti)

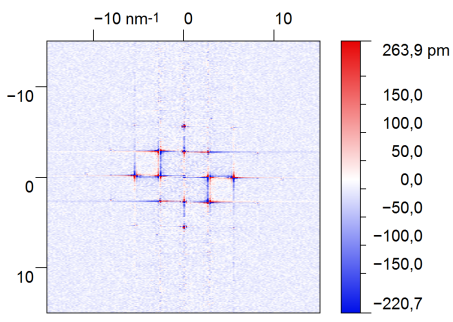

(b) 2D FFT of substrate in fig. 7.8a

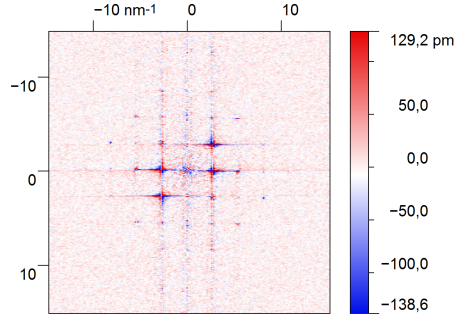

(c) 2D FFT of layer in fig. 7.8a

Figure 7.8: Sample 301a (pure LSMO): HRTEM images of substrate and layer and Fourier-transformed images of a squared area inside these HRTEM images. The stripes in fig. 7.8b and fig. 7.8c are a result of the narrow area and therefore an artifact

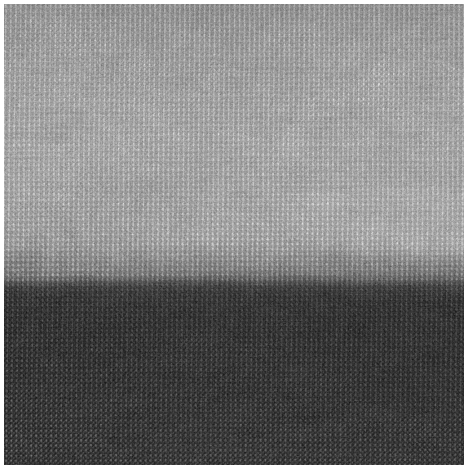

(a) Flat area of sample 301a: Expected perovskite structure (image length: 18.04 nm)

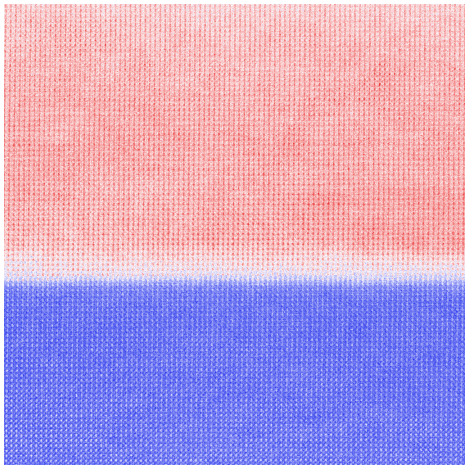

(b) 301a interface, colored version of fig. 7.9a

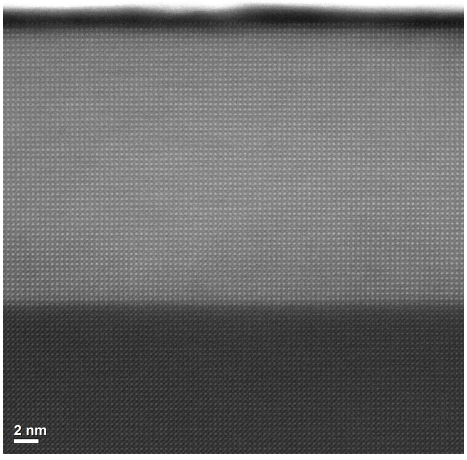

(c) Flat area of sample 230b ("edged Mn excess"): Pure perovskite structure

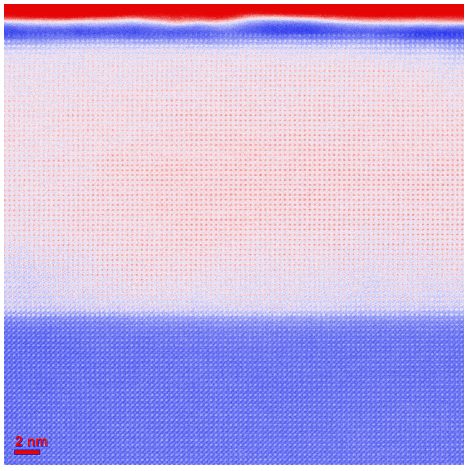

(d) 230b, colored version of fig. 7.9c

Figure 7.9: TEM of flat areas: Atomically sharp interface and surface for both samples, only the perovskite structure of STO substrate and LSMO layer are visible

substrate and layer, there is a sharp interface as well as a sharp surface on top of the sample. Additionally, in fig. 7.9c the surface is a straight line.

7.2.3 Defect areas

In fig. 7.6, aside from flat film areas, MnO particles are visible in both samples. In all images of fig. 7.10, layer and substrate show a well-defined LSMO/STO interface with the first few unit cells always consisting of stoichiometric perovskite LSMO, and no grains sprouting at substrate. Therefore, the substrate is not stimulating the particle growth. In the layer overview in fig. 7.7 and in the zoomed in images in fig. 7.10, there are no particles directly at the LSMO/STO interface. Some particles grew inside the layer, most visible dark defect zones resulting from particles are at the top of the single layer. Traces left by single particles as well as clustered particles are detected for sample 301a (pure LSMO) in fig. 7.7a and for sample 230b (edged Mn excess) in fig. 7.7b. In case of several particles in close vicinity, the layer tends to form bulges around the particles at the sample surface, see e.g. fig. 7.10b: The right-hand layer part is flat and smooth, but between the two particles, there is a higher layer thickness detected. No typical penetration depth of particles could be determined. One observes that the particle size distribution is far broader than the typical 20% needed for distinct features in scattering experiments [98].

Even in fig. 7.10 the perovskite structure is the only visible structure in all HRTEM images. Hence the composition of the films is not dependent of the amount of MnO which was added during deposition and for different samples. Focus on another defect zone in fig. 7.10e/7.10f again shows the perovskite structure, and the brightness corresponds of the surrounding LSMO layer to the La amount in LSMO.

7.2.4 EDX identification of the elements

On sample 230b (edged Mn excess) also EDX measurements were performed; the examined areas are shown in fig. 7.11. In fig. 7.11a a flat film region inside the sample was investigated to measure the stoichiometry of layer and substrate. The investigated defect area is displayed in fig. 7.11c.

In fig. 7.12, the according EDX spectra are shown. The layer of fig. 7.11a has a La:Sr ratio of 2:1, thus La(0.67)Sr(0.33), see fig. 7.12a. The stoichimeteric error is ca. 2%, 1% due to statistical noise and 1% systematic uncertainty due to background. Inside the layer, there is no Ti signal; inside the substrate, there is pure $SrTiO_3$, see fig. 7.12b. The EDX spectrum in fig. 7.12c of the defect particle in fig. 7.11c revealed only Mn and O, no signal of La or Sr. This defect particle is therefore a MnO_x sediment/separation with unknown Mn:O ratio. The Cu signals inside the EDX spectra originate from the sample holder.

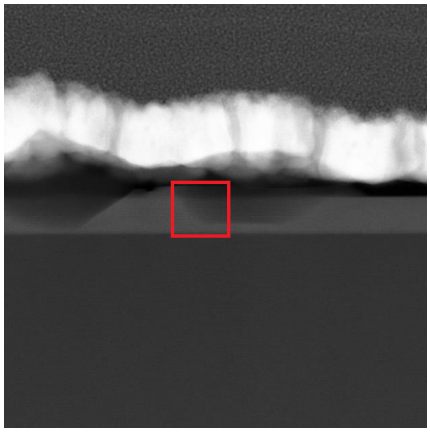

(a) 301a zoom of red marked area from fig. 7.6a (image length: 144.7 nm)

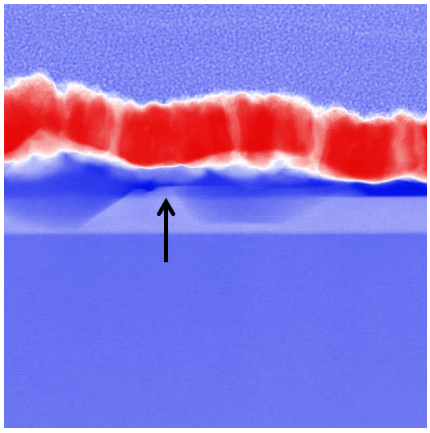

(b) colored version of 7.10a; inserted arrow points towards bulge

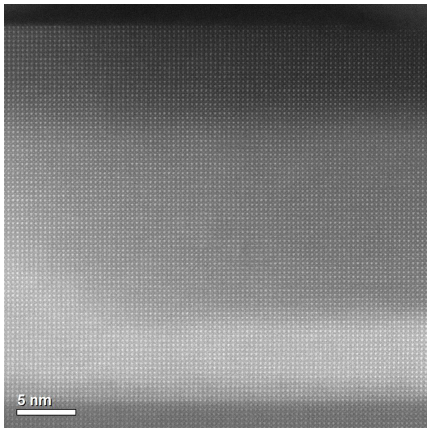

(c) Zoomed view of red area in fig. 7.10a: Perfect perovskite structure

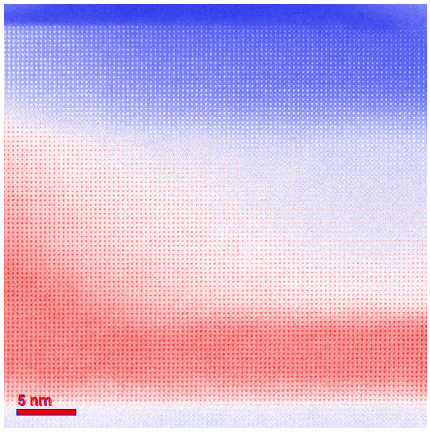

(d) colored version of fig. 7.10c

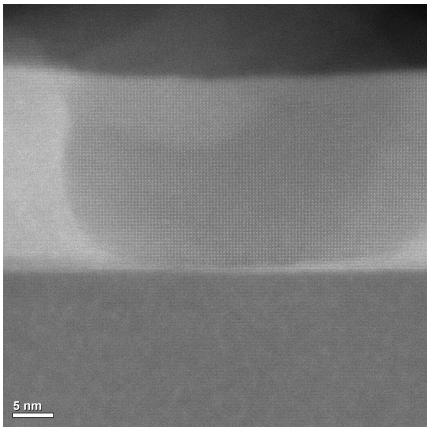

(e) Other defect zone: Perfect perovskite structure

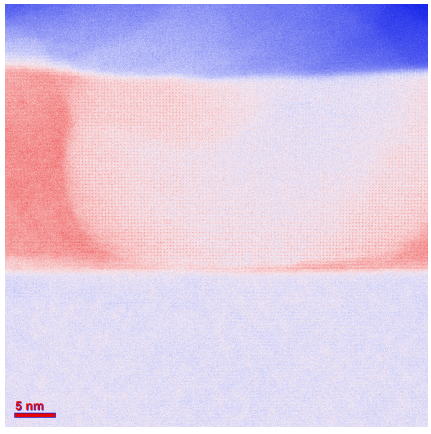

(f) colored version of fig. 7.10e

Figure 7.10: Defect areas of sample 301a ("pure LSMO")

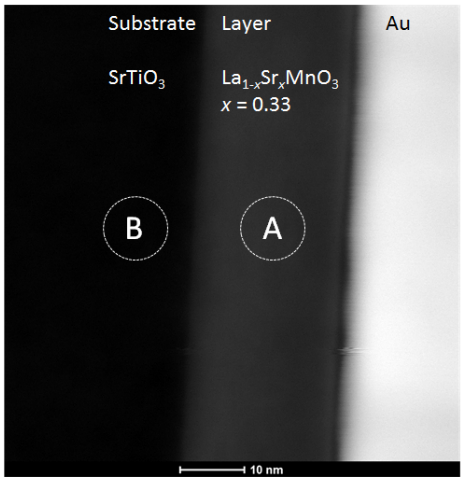

(a) Areas in which the EDX spectra of fig.7.12b and fig.7.12a were performed

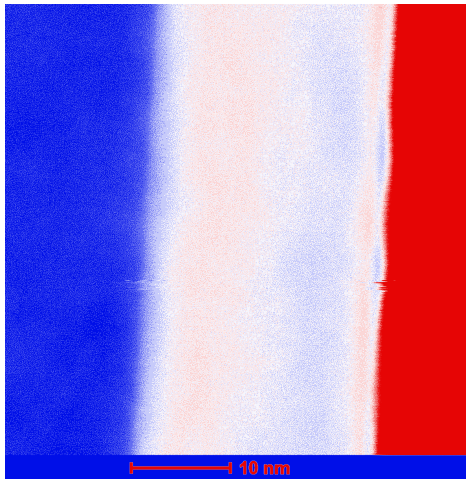

(b) Colored version of fig. 7.11a

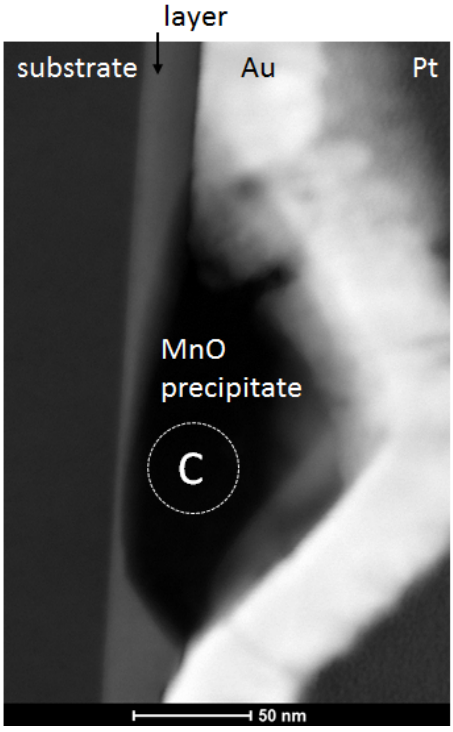

(c) Areas in which the EDX spectrum of fig.7.12c was performed

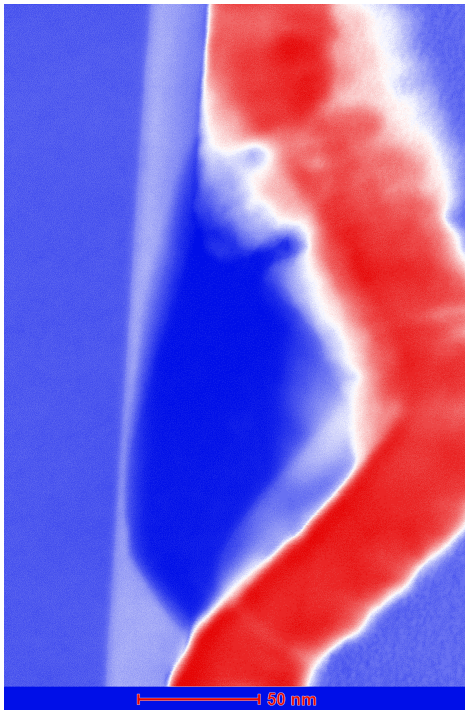

(d) Colored version of fig. 7.11c

Figure 7.11: EDX performed at sample 230b: Flat film area and clustered particles area

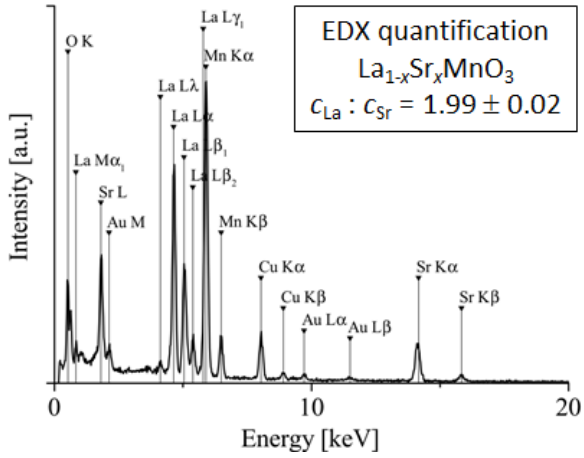

(a) EDX spectrum of layer

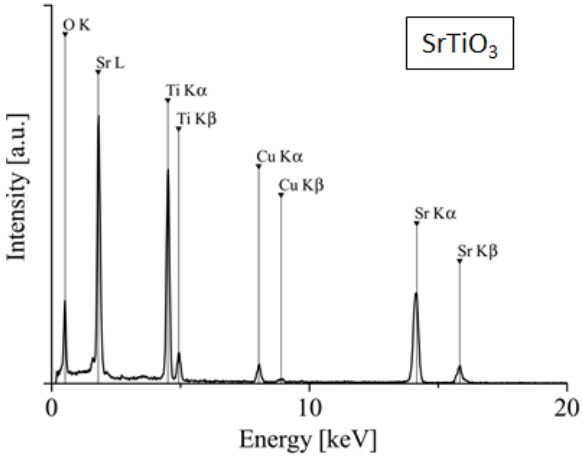

(b) EDX spectrum of substrate

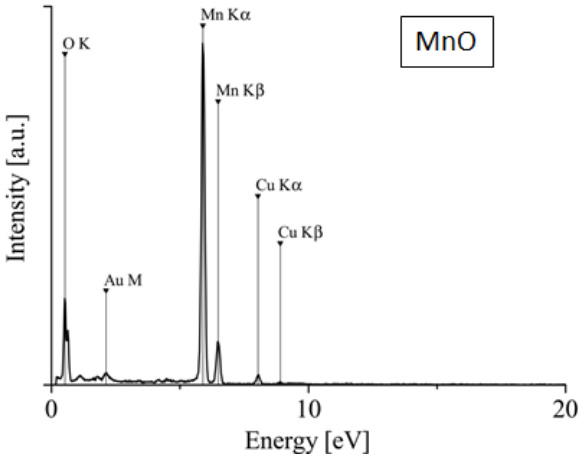

(c) EDX spectrum of precipitate

Figure 7.12: EDX at sample 230b: Spectra of areas shown in fig. 7.11

Chapter 8

Precipitate investigation

8.1 Precipitate volume quantification via SEM and TEM

To quantify the total amount of defect particles, two microscopy images were studied in detail to estimate the mean grain volume and distance to project the total amount of particle volume inside the LSMO layer of sample 301a (pure LSMO).

The SEM image in fig. 8.1a was taken to show the Pt structure on top of the Au layer, which was deposited onto the LSMO film to prepare the sample for TEM measurements. Fourier transformation of the upper part, marked by a frame, shows uncorrelated size and location of islands below the Au layer, see the smeared-out area instead of a well-defined circle which could be expected for monodisperse particles in fig. 8.1b. To quantify the grain structure, that area was analyzed via the grain analysis algorithm of the program Gwyddion [97], see tab. 8.1. The averaged grain radius was subtracted by the thickness of the Au layer of 300 Å. The particle density is given by the total investigated area devided by the number of grains. This was used to estimate the total grain volume inside the 1 cm^2 sample to 6.4*10^{-13} m^3. In case of a homogeneously covered sample, this gave a particle layer thickness of 64 Å.

To cross-check the total grain volume obtained from the SEM image, the TEM cross-section overview of sample 301a (pure LSMO) in fig. 7.6c was reviewed in detail. In this image cross-sections of particles are visible. The lower part of the particles appear as dark area inside the layer structure and the upper particle part as bright area inside the Au capping layer (darker than the surrounding Au). Standard auto-detecting functions like the one used to perform the SEM statistics failed to identify the particle size due to this contrast issue. Therefore, ellipsoids were drawn inside the particles, see fig. 8.2a. These ellipsoids were used to quantify the length, height and distance to next ellipsoid. In total, a layer area of 4.6 μm length was evaluated containing

Table 8.1: Statistics of sample 301a based on SEM image in fig. 8.1a; see text for details

Number of grains	4155
Total investigated area	73 μm^2
Averaged grain area	17.5*10^{-15} m^2
Averaged grain radius	74.6 nm
Averaged grain radius -30 nm Au layer	44.6 nm
Estimated total grain volume of 1 cm^2 sample area	6.4*10^{-13} m^3
Estimated particle layer height on 1 cm^2 sample area	64 Å

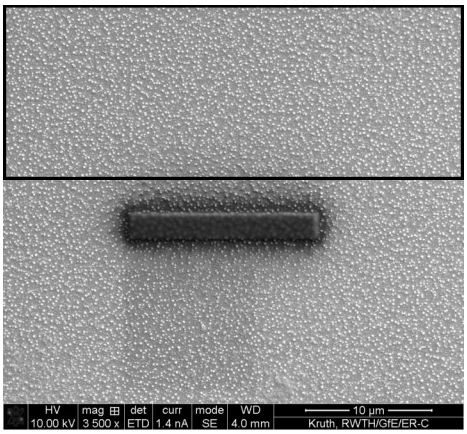

(a) SEM image of sample surface of sample 301a (pure LSMO) with Au cover layer and Pt-C stripe described in section 3.10 (p. 32)

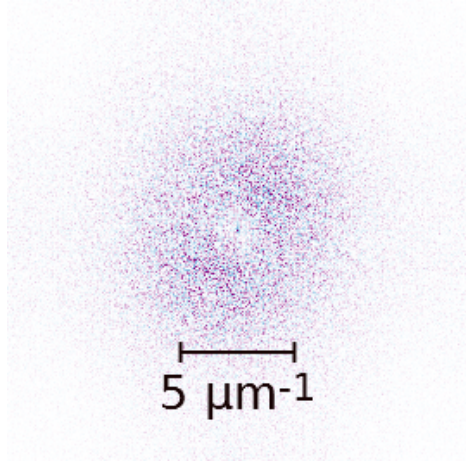

(b) Fourier transformation of rectangle area of SEM image in fig. 8.1a: No preferred direction

Figure 8.1: SEM image on which the statistics of tab. 8.1 is based

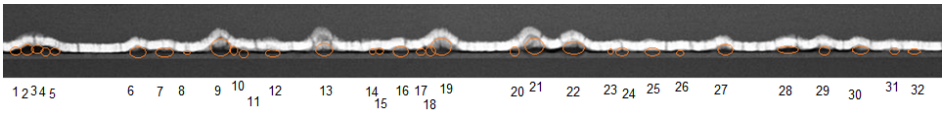

(a) TEM image of sample 301a with inserted enumerated orange ellipsoids

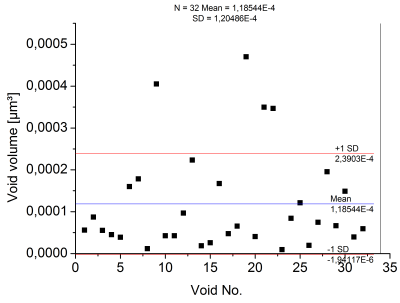

(b) Void volume

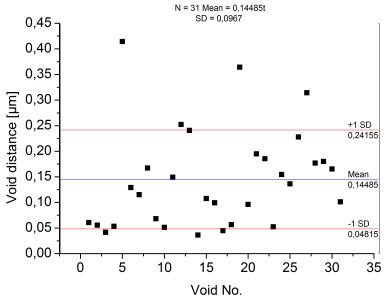

(c) Distance between neighboring voids

Figure 8.2: TEM image on which the statistics in tab. 8.2 is based

Table 8.2: Statistics of sample 301a based on TEM image in fig. 8.2a

Investigated particles	32
Mean particle volume	$1.18*10^{-4}\ \mu m^3$
Mean particle distance	$0.145\ \mu m$
Estimated total grain volume of 1 cm^2 sample area	$5.6*10^{-13}\ m^3$
Estimated particle layer height on 1 cm^2 sample area	56 Å

32 particles. The particle volume was then calculated as particle height times the square of the particle length times $\pi/6$. The result is shown in fig. 8.2b. The particle volume distribution is definitively not monodisperse. In fig. 8.2b, the particle distance is displayed in dependence of the particle number. There is no typical distance between the particles. The statistical details are given in tab. 8.2; the resulting total particle volume inside the film was estimated to be $5.6*10^{-13}$ m^3 or an average particle layer thickness of 56 Å. Compared to the 64 Åestimated on basis of the SEM image, both methods - interpretation of an SEM image of the Au layer and evaluation of artifacts in a 4.6 μm long TEM image - give the identical result.

8.2 Precipitate volume quantification from XRR and XRD

The particles visible in the TEM and SEM images are of different size and at uncorrelated locations and therefore it is not easy to determine the particle existence via scattering methods. On the other hand, the pure, monocrystalline LSMO onto STO substrate is very prominent with respect to potential particle reflexes and there are no stoichiometric or lattice deviations even around the voids in fig. 7.10. Still, the question rises as to whether these particles could be detected via XRR or XRD.

The capping layers introduced for the XRR fit in fig. 6.7a have a thickness of a few Å while the particles measured via TEM and SEM show a height of a few nm. Additionally, for detection via XRR the particles need to be monodisperse with respect to particle size and an identical vertical position inside the layer due to the in-plane averaging characteristics of the XRR measurements. Therefore, a particle volume could not estimated in the XRR fits.

For sample 230a as for sample 301b, a full XRD scan with range of Q_z=0..7 Å^{-1} was performed, see fig. 8.3. Inside the full XRD scans, only the STO substrate and LSMO layer peaks are visible; there is no hint of any kind of additional material inside these scans. On the other hand, the intensity of a single-phase, fully polycrystalline material (e.g. powder) with mass of the thin film would be smaller by a factor of 9000 (90 °divided by used angle resolution of 0.01 °). The layer peak is only 2.5 orders of magnitude larger than the background. Therefore, with a laboratory X-Ray source, only the LSMO layer on top of a STO substrate can be probed and analyzed in terms of crystallinity, or oxygen saturation.

8.3 Surface imaging via AFM

Additional AFM measurements were performed by Patrick Schöffmann (JCNS@MLZ) to investigate the surface between the particles, especially if there are atomically flat terraces [65]. To emphasize the layer structure, high intensity areas are masked out (purple colored areas).

In fig. 8.4a the AFM measurement of the sample to test the LS_3M_2O stoichiometry of section 6.2 is shown. Flat terraces can be identified with offshore islands of the same height. The terraces are around 100 nm to 200 nm long, which indicate a substrate miscut of around 0.004 ° to 0.002 °.

For sample 301 the substrate surface miscut could no longer be determined due to high particle density. Bottom left in fig. 8.4b, one terrace is visible including offshore islands in top direction.

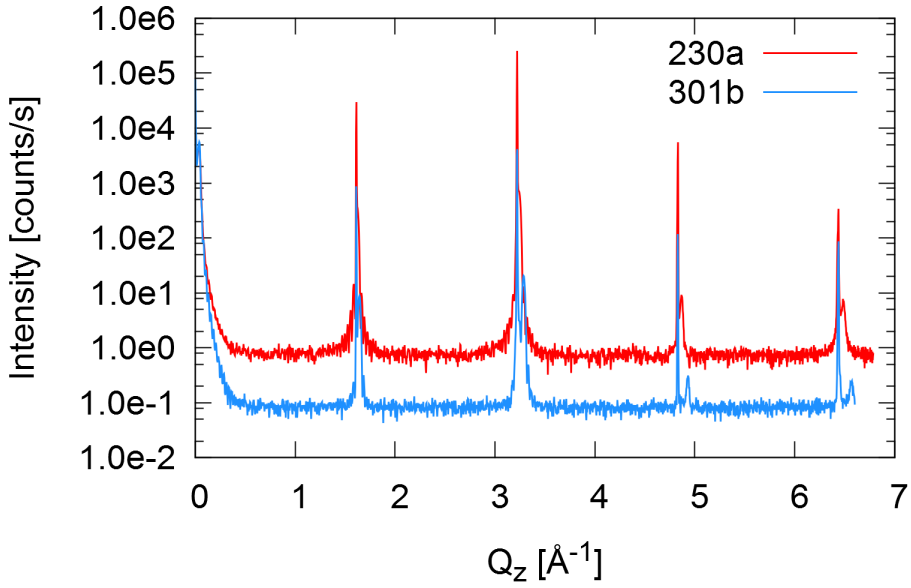

Figure 8.3: X-ray diffraction scans along the reciprocal space direction perpendicular to the sample surface of sample 230 ("edged Mn excess") and 301 ("pure LSMO"), scan of sample 301 shifted in intensity for clarity; additional powder peaks are estimated to be 3 orders of magnitude below the background at 1 counts/s

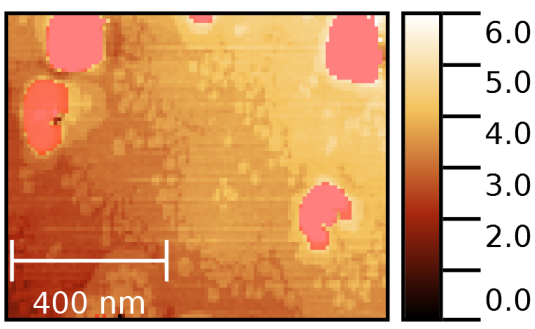

(a) AFM image of sample 292a ($(LS)_3M_2O$)

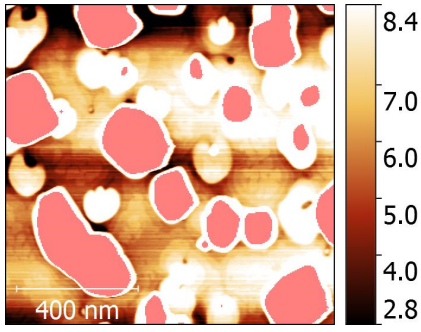

(b) AFM image of sample 301a (pure LSMO)

Figure 8.4: AFM measurements of 292a and 301a; color scale in nm; masked-out areas are marked in purple

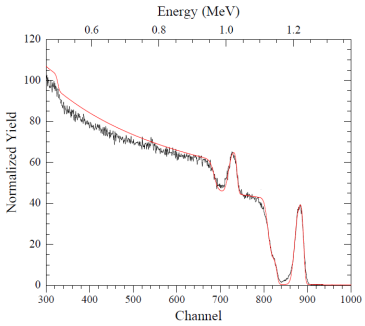

Figure 8.5: RBS data and simulation of sample 301a

The very bright area in the upper part is an effect of the AFM tip damping; the tip was adjusted to detect very small differences in height and could not follow the shape of the particles anymore, therefore brushed over the particles. For the same reason, the height is overrated.

The quantification of the total particle volume inside the sample by AFM is difficult. AFM gives only information about the topography, and not about the absolute particle height. Additionally, the measurements were performed to determine if the sample surfaces are terrace-like and therefore not suitable to quantify the particle height. To optimize the characterization of one particle, one should reduce the investigated area; this of course only provides one with a local information about that investigated area and supplies one no longer with any useful total volume information.

8.4 Surface composition investigation via AES

The size of the focused beam of the AES setup is in the range of a few hundred μm to a few mm. Therefore, particles with a size of nm covering ca. 15% of surface are undetectable via AES; still the LSMO signal from LSMO areas is visible in total and is indistinguishable from a $(LS)_7M_8O$ stoichiometry, which is the nominal composition for LSMO plus 0.15*MO. With respect to section 3.2 (p. 26), the difference between $(LS)_7M_8O$ and $(LS)_1M_1O$ cannot be resolved via AES.

8.5 Sample composition determination via RBS

RBS on sample 301a in fig. 8.5 detected a stoichiometric composition of $La_{0.95}Sr_{0.63}Mn_{2.4}O$, which is roughly $(LS)_2M_3O$ instead of the $(LS)_1M_1O$ called for by the MBE recipe. This could be due to a fault ion gauge head and therefore a lack of effusion cell equilibrium, and therefore an exceptional bad quality in that sample batch.

If the detected $(LS)_2M_3O$ splits into pure LSMO and additional MnO_x, therefore fully transforming the Mn excess into particles, the particle contribution is 1/3 of the layer. This is in agreement with the calculations based on TEM and SEM images in section 8.1.

Table 8.3: Parameters and errors for hysteresis simulations in fig. 8.6

Sample name	230b	301b
M_{S1} [Am^2]	2.0965e-07 (1e-11)	1.95e-07 (1e-9)
H_{C1} [T]	0.017566 (9e-06)	0.017 (0.001)
H_{EB1} [T]	0.002176 (9e-06)	-0.0010 (0.0005)
w_1 [°]	196.8 (0.2)	130 (5)
M_{S2} [Am^2]	1.776e-08 (3e-11)	1.6e-8 (1e-9)
H_{C2} [T]	0.74	0.70 (0.01)
H_{EB2} [T]	0.1005 (0.0007)	-0.030 (0.005)
w_2 [°]	4.69 (0.02)	10 (1)
$M_{S2}/(M_{S1}+M_{S2})$	0.055	0.076

8.6 Perecipitate stoichiometry analysis via SQUID

Magnetic measurements were performed at the two samples which were investigated via TEM. A field-cooled measurement was performed from 370 K to 5 K for 301b (pure LSMO, fig. 8.6a) and 350 K to 5K for sample 230b (edged Mn excess, fig. 8.6c). Both samples show a kink at the transition temperature of STO around 105 K and an additional kink below 50 K, which was before interpreted to be the oxygen transition temperature [71]; even the SQUID manufacturer gave an application note about the phenomenon that oxygen might freeze and give a contribution like this [99].

With respect to the EDX measurements in section 7.2.4, it is known that there is a MnO_x excess with unknown x. In the family of manageseoxides, Mn_3O_4 has a phase transition from paramagnetic at room temperature to ferrimagnetic below 41-43 K [100]. Therefore the kink below 50 K is an indicator for the Mn_3O_4 assumption.

Additionally, hysteresis loops were measured at 5 K. The loops for sample 301b (fig. 8.6b) and 230b (fig. 8.6d) show a behavior which can be fitted as two independent hysteresis loops, one having a coercive field of 0.7 T with a magnetization of one order of magnitude below the other hysteresis loop, see tab. 8.3.

For sample 230b, hysteresis loops were measured at other temperatures. The minor loop vanishes below 50 K, which is in the vicinity of the Mn_3O_4 ferrimagnetic-to-paramagnetic-transition temperature.

The hysteresis loop with smaller coercitive field and bigger saturation does not change significantly between 5 K and 40 K and afterwards only the saturation value starts to shrink, and therefore is the contribution of the LSMO layer material.

For antiferromagnets, a coercitive field of 0.7 T is very low. In comparison with [101], the hysteresis loop with the bigger coercitive field must arise from Mn_3O_4 contributions.

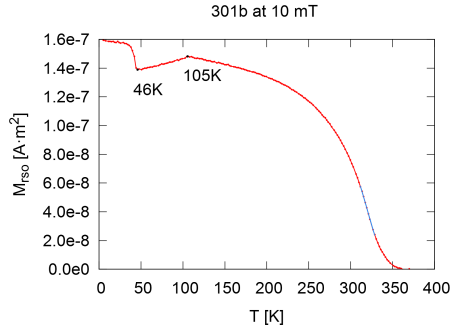

(a) Field-cooled curve of sample 301b (pure LSMO)

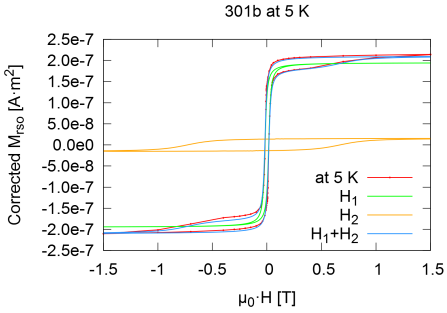

(b) 301b: Hysteresis loop at 5K

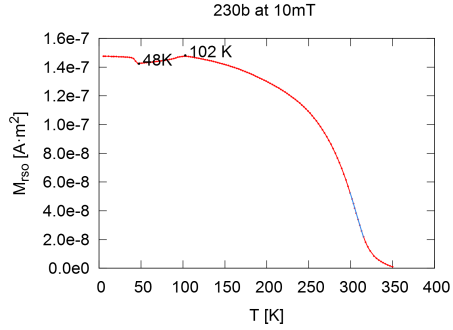

(c) Field-cooled measurement of sample 230b (edged Mn excess)

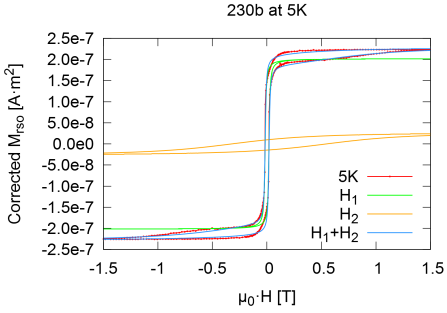

(d) Magnetization vs. field at 5K of 230b

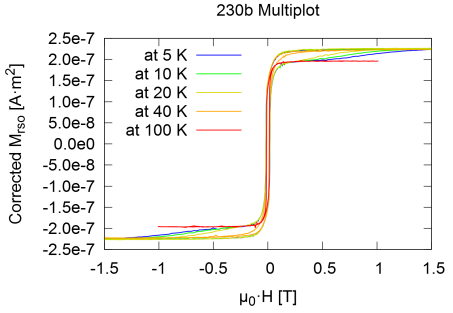

(e) Multiple hysteresis loops

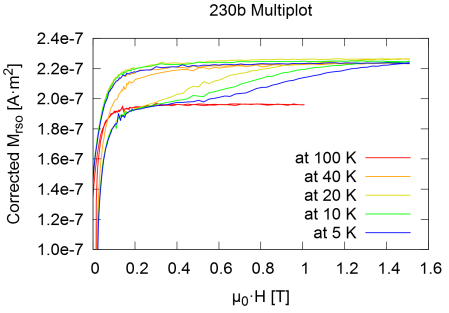

(f) Zoom inside multiple hysteresis loops

Figure 8.6: M(T) and M(H) measurements of sample 301b (pure LSMO) and 230b (edged Mn excess). The M(T) measurements show between 50 K and 370 K standard behavior of pure LSMO

Chapter 9

Discussion

LSMO thin film samples were produced via co-deposition. In section 5.1 (p. 47), the reproducibility, homogenity and high quality of these samples was shown.

The aim was to create stoichiometric gradients to investigate the influence of local stoichiometry on the magnetic profile inside the thin film. For the growth of these gradients, the shuttered growth technique was utilized in section 6.3 (p. 63) to deposit via atomic-layer-by-atomic-layer deposition additional MnO layers with layer height of one atom in that way that different MnO excess profiles inside the thin films should have been created. RHEED intensity oscillations observed during growth appeared to verify the successful growth of such gradient structures. Fig. 6.5g (page 64) displays the expected, nominal structure of the layer as aimed for with the MBE procedure used. The sample quality was cross-checked via XRR and XRD.

If the atoms released via the shutter openings were stuck at the sample surface immediately without affecting the sample in any other way, the height-resolved stoichiometries in fig. would have been created.

PNR simulations in section 7.1.1 (p. 67) performed to determine the magnetic structure of the structural gradient samples do not fit. Only when the stoichiometric profile of the simulations is changed towards a layer consisting of LSMO with an additional MnO contribution towards the surface (see section 7.1.2, p. 73), the simulations follow the data.

The PNR measurement fits show that the structure inside the sample has to be different than the one expected from the MBE recipe. The next step was the study of the samples in real space. TEM measurements (section 7.2.1-7.10, pp. 83)reveal instead of the gradient structure, pure single-phase LSMO with cavities, which were determined via EDX to be MnO precipitates, as sketched in fig. 9.1b. Evidently LSMO prefers to grow in a perovskite structure and the

(a) Sketch: Graded LSMO with additional flat Manganeseoxide layers at different vertical positions

(b) Sketch: Pure LSMO with manganeseoxide precipitates, uncorrelated in particle diameter and position

Figure 9.1: Sketch of nominal and actual stoichiometry profiles of the gradient samples

additional MnO moves towards the surface like a surfactant and clusters there to form surface-near precipitates. Further SQUID measurements in section 8.6 (p. 98) support the assumption that the majority of this manganeseoxide is Mn_3O_4.

The so-called stoichiometric gradient samples deviate from the assumed local and global stoichiometry. There is a Mn_3O_4 excess and a pure LSMO layer. The amount of additional Mn_3O_4 for sample 230 ("edged Mn excess") is interpretated, that the MnO excess of additional layers might cluster forming MnO_x particles. The additional particle material in sample 301 might originate from not stable enough MBE effusion cell rates. While for the gradient sample series 224-233 the effusion cells were continuously running for 6 days before sample preparation, sample 301a ("pure LSMO") was prepared after a series of temperature drop-downs of effusion cells during the last few days. Before preparation of sample 301a ("pure LSMO"), the effusion cells were only for a few hours at their targeted temperature instead of a week.

During preparation of sample 230 ("edged Mn excess") the additional Mn_3O_4 was deposited mostly at start and end of the thin film deposition, for sample 301 the Mn excess was deposited homogeneously during growth. Still, TEM revealed for both samples the same location for the Mn_3O_4 excess - clustering as precipitates and not sprouting at the LSMO/STO interface, but aside from that in no specific sample height or with a typical diameter, see fig. 7.6 (p. 84). SQUID measurements in section 8.6 (p. 98) showed identical behavior for samples 230b ("edged Mn excess") and 301b ("pure LSMO"), too. This shows that the Mn_3O_4 precipitates are independent of the MBE effusion cell shutter opening intervals.

For both samples the RHEED intensity oscillations corresponding to the amount of via MBE recipe proposed layer material were observed. This was interpreted as proof that inside the layers the stoichiometric gradients were created. In section 6.1 (page 59) the number of MBE opening intervals and therefore assumed perovskite unit cells were found to correspond to the total layer thickness of sample 301 ("pure LSMO"). The RHEED pattern of sample 230 ("edged Mn excess") shows double-decreased intensities for double-Mn shutter opening intervals but TEM revealed clustered MnO precipitates instead of MnO layers inside LSMO. Therefore, the RHEED intensity oscillations provide an indication of the top atomic layer of the layer structure during growth. As an assumption, the MnO is floating like a surfactant, stays on top during layer growth and clusters gradually.

While for co-deposition the sample preparation was optimized in section 4.2 (p. 36) to create smooth homogeneous layers via letting the single atoms diffuse into the correct position, in fully-shuttered mode it is crucial that the deposited atoms stick and form an atomic layer. On the one hand, the new atomic layer needs enough energy to not grow amorphously and becomes a part of the perovskite lattice, on the other hand the new layer is not supposed to have enough energy threshold for crystallization to cluster with itself rather than with the underlying material.

Ishii et al. [102] pointed out that already during the second part of the growth process, the film deposition, a surface in non-equilibrium state can give rise to adsorption, surface diffusion and dissociation processes before the incoming oxidized La, Sr and Mn crystallize as layer or nucleate as precipitate. Additionally, the process only for cooling down from 900 °C to 800 °C in 300 seconds takes significantly longer than diffusion processes with a time scale of seconds.

In case of small deviations from ideal off-stoichiometry, at 900 °C the defect particle distribution is homogeneous on the sample with a maximized particle distance [102]. Due to the effusion cell-based deposition method and therefore the stoichiometric errorbar of less than 2%, one can obtain the off-stoichiometry via optimizing the growth temperature; this should enlarge the areas of pure LSMO stoichiometry. Since Mn_3O_4 and LSMO are chemically compatible [103], the LSMO/MO multilayers and gradient structures were grown at high temperatures to achieve high defect distances. Small amounts of solid state diffusion might occur, but the crystal optics error density needs only to be low enough to create a sufficient sample quality. Though Mn_3O_4 films on LSMO films are known to tend to grow with a zig-zag shaped [101] or undulating interface [104], in-situ performed RHEED seemed to prove the growth of these structures to be well above the crystallization threshold.

In terms of LSMO, the growth was optimized. In terms of additional MnO_x layers inside this LSMO layer, the growth conditions lead to phase separation instead of a multilayer structure. This effect was only noticed due to the combination of multiple methods, especially PNR and TEM.

RHEED as in-situ surveillance method showed all essential characteristics to consider the growth of the attempted stoichiometric gradients to be successful. LEED showed the crystalline structures of the sample surfaces which do not contradict the assumption of stoichiometric gradients. XRR and XRD show existence of layer structure corresponding to RHEED intensity oscillations and amount of deposited material.

None of these methods investigates the depth-sensitive magnetic properties or the local real-space structure. PNR closes the gap concerning the magnetic structure, and TEM concerning the real-space local structure. Applying both these techniques revealed a different picture from the one gained via RHEED, LEED, XRR and XRD. This corroborates the need for the combination of methods sensitive to global structure, magnetic structure and local real-space structure. Only the combination of these methods reveal the existence of self-purifying $La_{2/3}Sr_{1/3}MnO_3$ epitaxial films with surface precipitation of Mn_3O_4 particles for excess Mn ratios and thus a solid insight to the behavior of samples.

Chapter 10

Outlook

During the detailed analysis of the various LSMO samples, several prospective approaches for further studies emerged:

The idea of stoichiometric gradient structures and the stoichiometric influence on the magnetic profile is particularly intriguing. To focus on the magnetic profile, one could produce such gradients in a system of less preparation complexity, e.g. grow 2 different metals, one ferromagnetic, one not, as amorphous structure. Kirby et al. [105] recently published a study about Ni_xCu_{1-x} system and could show that with PNR it is feasible to investigate the magnetic profile of such a gradient structure. Obviously, there is a large variety of material systems with multiple potential behaviors awaiting further studies.

A detailed investigation of growth parameters for the LSMO gradient structures is definitively fascinating, varying the MO or LSO content. While the parameters determined via co-deposition are a good start, the recent results however indicate that these parameters for shuttered deposition should not be used without careful cross-check by complementary methods. Additionally, very fascinating for thin film growth is the observation that RHEED revealed the crystallized unit cells, but not necessarily predicted correctly the local stoichiometry of the sample post preparation.

Moreover, a detailed study on the influence of MnO deposited at different time in shuttered gradient deposition onto the particle density, size and distribution might give a deeper insight into the growth process itself. Because aging of the existing samples cannot be ruled out, fresh samples are needed for such a study. Additionally, by varying the deposition parameters, i.e. lowering the substrate temperature during growth or using a lower chamber pressure, it might be possible to produce such gradient samples in the LSMO family.

TEM revealed that LSMO is an excellent basis material for magnetoelectric epitaxial composites due to the highly precise perovskite structure around the precipitates. After depositing a LSMO start layer, one could deposit monodisperse ferroelectric nanoparticles while still growing LSMO. This potentially results in an embedded structure of ordered ferroelectric nanoparticles inside a ferromagnetic matrix in contrast to the magnetic nanoparticles inside a ferroelectric layer [106]. Additionally, the standard disadvantage of composites over multilayer structures, the reduced coupling, should be overcome by the epitaxial ordering [107].

Chapter 11

Summary

Thin $La_{2/3}Sr_{1/3}MnO_3$ films were produced by Oxide MBE. Parameters to influence thin film quality during growth were identified and optimized. The targeted LSMO stoichiometry could be achieved. The reproducibility was successfully shown by growing 12 samples with identical MBE preparation parameters. These samples prove that homogeneous films with 1.5 cm substrate length are feasible.

Additional samples were grown by the shuttered growth technique. The intensity modulation seen in RHEED data were correlated with MBE logfiles using scripts specially developed for that purpose. A correlation between RHEED intensity oscillations and effusion cell opening intervals could be established, leading to the assumption that the opening intervals were responsible for the modulation in the vertical stoichiometry and stoichiometric gradients. XRR and XRD measurements supported that finding.

Combined PNR and XRR data fitting reveal inconsistencies in the stoichiometric gradient model; only SLD profiles with significant MnO_x excess towards the surface agree with the data. TEM measurements confirm that a pure LSMO layer with partly embedded, phase-separated MnO_x particles exists, instead of the nominally assumed graded multilayer structure. TEM and RBS show that the volume for MnO_x excess for sample 301a ("pure LSMO") is 1/3 of the total layer material. Further SQUID measurements establish the particles to have a Mn_3O_4 stoichiometry.

The results clearly show that the common combination of methods leads to an incomplete picture of samples with stoichiometric gradients as the combination of PNR as scattering and TEM as imaging method render a significantly different picture of the sample composition.

Chapter 12

Acknowledgements

This work would not have been possible without the help and support of numerous people. I want to thank the following people for contributing to this work:

Prof. Dr. Thomas Brückel for offering me the opportunity to work in this very interesting field and for supporting me throughout the time. I want to thank him in particularly for enabling me to work at JCNS@MLZ. By this, I had the opportunity to produce my own samples at the MBE and get to know the day-to-day neutron instrument operation during this work.

Prof. Dr. Joachim Mayer for agreeing to take the second revision of this work and to offer the possibility of TEM measurements.

Sabine Pütter for the great support in every part of this thesis, for all the time and patience, your scientific support and advice and the numerous discussions with you really brought this work forward.

Stefan Mattauch for the kind introduction into the operation of MARIA. Stefan Mattauch and Adreas Ofner for the tremendous trust to let me explore TREFF. Alexander Weber for the data reduction support.

Juri Barthel and Max Kruth (ER-C/Forschungszentrum Jülich GmbH) for the TEM sample preparation, STEM, TEM, HR-TEM and EDX measurements and the very enlightening numerous discussions.

Stefan Geprägs (Walter-Meissner-Institut/BAdW) for the possibility to perform XRD and SQUID measurements, as well as the the Peter Link and Christian Breunig (Neutron Optics group@MLZ) and Armin Kriele (Soft Hard Matter Lab@MLZ) for letting me use their X-ray reflectometer.

Valeria Lauter, Artur Glavic and Hailemariam Ambaye for the scientific support during the neutron reflectometry beamtime at the Magnetism Reflectometer at SNS. Artur Glavic and Frank Gossen for introducing me to all the experimental techniques and the strong encouragement to gain as much knowledge as feasible.

Jürgen Schubert and Willi Zander (PGI-9/Forschungszentrum Jülich GmbH) for the RBS measurements and data evaluations. Jürgen Schubert for the continuous mentoring, the fruitful discussions and suggestions during this work.

Jeffrey McCord (Institute for Materials Science, CAU University of Kiel) for the MOKE microscopy image and the fruitful discussions about MOKE interpretation.

Patrick Schöffmann for the AFM measurements and his huge scientific curiosity.

Alfred Richter, Marco Gödel, Daniel Vujevic, Bernard Großmann, Harald Kusche, Andreas Nebel, Vladimir Ossovyi, Simon Staringer, and Harald Schneider for their technical support.

Olaf Holderer, Vladimir Hutanu, Sebastian Jaksch, Henrich Frielinghaus, Walter van Herck, Jörg Voigt and Martin Meven for their willingness to give insight into scientific daily life.

Barbara Daegener and Michael Beißel for their enduring patience and indefatigable encouragement.

Thomas Gutberlet, Ida Berts, Rainer Bruchhaus, Bernhard Hopfenmüller, Antonella Campanella, Rui Wang, Erxi Feng, Viviane Pecanha Antonio, Amir Syed Mohd, Guido Vehres, Franziska Michel, Johannes Reim, Markus Schmitz, Markus Waschk, Genevieve Wilbs, Barbara Gold, Naveen Kumar Chogondahalli Muniraju, Laura Stingaciu, Eva Steinberger, Piotr Zolnierczuk, Klaus Bussmann, Peter Harbott, Elisabeth Josten, Ina Lommatzsch, Ramona Bucher, the Quantum group@MLZ and all the JCNS members for the nice time.

Alice Klapper for the outstanding support during all the time.

And my family, especially Victoria, Ralph, Robert, Daniela, Michael, Katharina, Martin, Oskar, Friederike, Konrad, Knut, Irene, Dorothea, Torben, Stella, Holger, Ines, and Tabea, for their constant support and love.

Bibliography

[1] C. Aruta, M. Minola, A. Galdi, R. Ciancio, A. Y. Petrov, N. B. Brookes, G. Ghiringhelli, L. Maritato, and P. Orgiani, "Off-stoichiometry effect on orbital order in A-site manganites probed by x-ray absorption spectroscopy," *Phys. Rev. B*, vol. 86, no. 11, pp. 115 132–, Sep. 2012. [Online]. Available: http://link.aps.org/doi/10.1103/PhysRevB.86.115132

[2] R. G. Palgrave, P. Borisov, M. S. Dyer, S. R. C. McMitchell, G. R. Darling, J. B. Claridge, M. Batuk, H. Tan, H. Tian, J. Verbeeck, J. Hadermann, and M. J. Rosseinsky, "Artificial construction of the layered Ruddlesden-Popper manganite $La_2Sr_2Mn_3O_{10}$ by Reflection High Energy Electron Diffraction monitored Pulsed Laser Deposition," *J. Am. Chem. Soc.*, vol. 134, no. 18, pp. 7700–7714, Mar. 2012. [Online]. Available: http://dx.doi.org/10.1021/ja211138x

[3] F. Y. Bruno, J. Garcia-Barriocanal, M. Varela, N. M. Nemes, P. Thakur, J. C. Cezar, N. B. Brookes, A. Rivera-Calzada, M. Garcia-Hernandez, C. Leon, S. Okamoto, S. J. Pennycook, and J. Santamaria, "Electronic and magnetic reconstructions in $La_{0.7}Sr_{0.3}MnO_3/SrTiO_3$ heterostructures: A case of enhanced interlayer coupling controlled by the interface," *Physical Review Letters*, vol. 106, no. 14, p. 147205, Apr. 2011.

[4] D. Niebieskikwiat, L. E. Hueso, J. A. Borchers, N. D. Mathur, and M. B. Salamon, "Nanoscale magnetic structure of ferromagnet/antiferromagnet manganite multilayers," *Phys. Rev. Lett.*, vol. 99, no. 24, pp. 247 207–, Dec. 2007. [Online]. Available: http://link.aps.org/doi/10.1103/PhysRevLett.99.247207

[5] M. Matvejeff, E. Ahvenniemi, R. Takahashi, and M. Lippmaa, "Magnetic coupling at perovskite and rock-salt structured interfaces," *Applied Physics Letters*, vol. 107, no. 14, p. 141604, 2015. [Online]. Available: http://scitation.aip.org/content/aip/journal/apl/107/14/10.1063/1.4931705

[6] [Online]. Available: http://www.mlz-garching.de/MBE

[7] H. K. Sato, C. Bell, Y. Hikita, and H. Y. Hwang, "Stoichiometry control of the electronic properties of the $LaAlO_3/SrTiO_3$ heterointerface," *Appl. Phys. Lett.*, vol. 102, no. 25, pp. 251 602–4, Jun. 2013. [Online]. Available: http://dx.doi.org/10.1063/1.4812353

[8] J. H. Haeni, C. D. Theis, D. G. Schlom, W. Tian, X. Q. Pan, H. Chang, I. Takeuchi, and X.-D. Xiang, "Epitaxial growth of the first five members of the $Sr_{n+1}Ti_nO_{3n+1}$ Ruddlesden-Popper homologous series," *Appl. Phys. Lett.*, vol. 78, no. 21, pp. 3292–3294, May 2001. [Online]. Available: http://dx.doi.org/10.1063/1.1371788

[9] N. Ikeda, T. Nagata, J. Kano, and S. Mori, "Present status of the experimental aspect of RFe_2O_4 study," *Journal of Physics: Condensed Matter*, vol. 27, no. 5, pp. 053 201–, 2015. [Online]. Available: http://stacks.iop.org/0953-8984/27/i=5/a=053201

[10] Y. Liu and X. Ke, "Interfacial magnetism in complex oxide heterostructures probed by neutrons and X-rays," *Journal of Physics: Condensed Matter*, vol. 27, no. 37, pp. 373 003–, 2015. [Online]. Available: http://stacks.iop.org/0953-8984/27/i=37/a=373003

[11] C. Lu, W. Hu, Y. Tian, and T. Wu, "Multiferroic oxide thin films and heterostructures," *Applied Physics Reviews*, vol. 2, no. 2, p. 021304, 2015. [Online]. Available: http://scitation.aip.org/content/aip/journal/apr2/2/2/10.1063/1.4921545

[12] M. Bibes, J. E. Villegas, and A. Barthelemy, "Ultrathin oxide films and interfaces for electronics and spintronics," *Advances In Physics*, vol. 60, no. 1, pp. 5–84, 2011.

[13] S. D. Ha and S. Ramanathan, "Adaptive oxide electronics: A review," *Journal of Applied Physics*, vol. 110, no. 7, p. 071101, Oct. 2011.

[14] J. Hemberger, A. Krimmel, T. Kurz, H. A. K. von Nidda, V. Y. Ivanov, A. A. Mukhin, A. M. Balbashov, and A. Loidl, "Structural, magnetic, and electrical properties of single-crystalline $La_{1-x}Sr_xMnO_3$ ($0.4 \leq x \leq 0.85$)," *Physical Review B*, vol. 66, no. 9, p. 094410, Sep. 2002.

[15] R. Bruchhaus, *Electronic Oxides - Correlation Phenomena, Exotic Phase and Novel Functionalities*, ser. 41^{st} IFF Springschool 2010. Forschungszentrum Jülich GmbH, 2010, ch. Crystal Structures and Chemical Bonds in Transition Metal Oxides, pp. A1.1–A1.23.

[16] T. Brückel, "A neutron primer: Elastic scattering and the properties of the neutron," in *Neutron Scattering*. Forschungszentrum Jülich GmbH, 2010.

[17] D. R. Y. u. H. B. Horst Kp̈pel, Ed., *The Jahn-Teller Effect - Fundamentals andd Implications for Physics and Chemistry*. Springer, 2009.

[18] G. F. Dionne, *Magnetic Oxides*. Springer, 2009.

[19] J. L. Maurice, D. Imhoff, J. P. Contoury, and C. Colliex, "Interfaces in 100 epitaxial heterostructures of perovskite oxides," *Philosophical Magazine*, vol. 86, no. 15, pp. 2127–2146, 2006.

[20] W. Meevasana, P. D. C. King, R. H. He, S.-K. Mo, M. Hashimoto, A. Tamai, P. Songsiriritthigul, F. Baumberger, and Z.-X. Shen, "Creation and control of a two-dimensional electron liquid at the bare $SrTiO_3$ surface," *Nat Mater*, vol. 10, no. 2, pp. 114–118, Feb. 2011. [Online]. Available: http://dx.doi.org/10.1038/nmat2943

[21] A. F. Santander-Syro, O. Copie, T. Kondo, F. Fortuna, S. Pailhes, R. Weht, X. G. Qiu, F. Bertran, A. Nicolaou, A. Taleb-Ibrahimi, P. Le Fevre, G. Herranz, M. Bibes, N. Reyren, Y. Apertet, P. Lecoeur, A. Barthelemy, and M. J. Rozenberg, "Two-dimensional electron gas with universal subbands at the surface of $SrTiO_3$," *Nature*, vol. 469, no. 7329, pp. 189–193, Jan. 2011. [Online]. Available: http://dx.doi.org/10.1038/nature09720

[22] F. Gervais, J.-L. Servoin, A. Baratoff, J. G. Bednorz, and G. Binnig, "Temperature dependence of plasmons in Nb-doped $SrTiO_3$," *Phys. Rev. B*, vol. 47, no. 13, pp. 8187–8194, Apr. 1993. [Online]. Available: http://link.aps.org/doi/10.1103/PhysRevB.47.8187

[23] D. G. Schlom, L. Q. Chen, C. B. Eom, K. M. Rabe, S. K. Streiffer, and J. M. Triscone, "Strain tuning of ferroelectric thin films," *Annual Review of Materials Research*, vol. 37, pp. 589–626, 2007.

[24] U. Rücker and E. Kentzinger, "Thin film systems: Scattering under grazing incidence," in *Probing the Nanoworld - Microscopies, Scattering and Specxtroscopies of the Solid State*, ser. IFF Spring School. Forschungszentrum Jülich GmbH, 2007.

[25] L. G. Parratt, "Surface studies of solids by total reflection of X-rays," *Phys. Rev.*, vol. 95, no. 2, pp. 359–, Jul. 1954. [Online]. Available: http://link.aps.org/doi/10.1103/PhysRev.95.359

[26] E. Kentzinger, U. Rücker, B. Toperverg, F. Ott, and T. Brückel, "Depth-resolved investigation of the lateral magnetic correlations in a gradient nanocrystalline multilayer," *Phys. Rev. B*, vol. 77, no. 10, pp. 104 435–, Mar. 2008. [Online]. Available: http://link.aps.org/doi/10.1103/PhysRevB.77.104435

[27] M. Tolan, *X-ray Scattering from Soft-Matter Thin Films - Materials Science and Basic Research*, ser. Springer Tracts in Modern Physics. Springer, 1999, vol. 148. [Online]. Available: http://rd.springer.com/book/10.1007%2FBFb0112834

[28] G. Roth, *Lecture Notes of the JCNS Laboratory Course Neutron Scattering*. Forschungszentrum Jülich GmbH, 2015, ch. Diffraction, pp. 4.1–4.37.

[29] P. F. Fewster, "X-ray analysis of thin films and multilayers," *Reports On Progress In Physics*, vol. 59, no. 11, pp. 1339–1407, Nov. 1996.

[30] [Online]. Available: https://icsd.fiz-karlsruhe.de/

[31] A. Glavic. [Online]. Available: https://sourceforge.net/projects/plotpy

[32] [Online]. Available: http://www.dca.fi/product-dca/m600-mbe-system

[33] [Online]. Available: http://www.specs.de/cms/upload/PDFs/SPECS_Prospekte/2010_11_ErLEED_100_150_brochure_final_web.pdf

[34] [Online]. Available: http://www.k-space.com/wp-content/uploads/kSA400Software.pdf

[35] [Online]. Available: http://www.gammavacuum.com/index.php/product?id=7

[36] [Online]. Available: http://www.oaresearch.co.uk/oaresearch/rfatomspec

[37] [Online]. Available: http://www.staibinstruments.com/rheed/rheed_systems.html

[38] [Online]. Available: http://www.eurotherm.com/index.php?route=product/download/get&download_id=109

[39] L. E. Davis, N. C. Mac Donald, P. W. Palmberg, G. E. Riach, and R. E. Weber, Eds., *Handbook of Auger Electron Spectroscopy*. Physical Electronics Industries, Inc., 1976.

[40] T. Kubo and H. Nozoye, "Surface structure of SrTiO3(1 0 0)," *Surface Science*, vol. 542, no. 3, pp. 177 – 191, 2003. [Online]. Available: http://www.sciencedirect.com/science/article/pii/S0039602803009981

[41] I. Hernandez-Calderon and H. Hoechst, "New method for the analysis of reflection high-energy electron diffraction: α-Sn(001) and InSb(001) surfaces," *Phys. Rev. B*, vol. 27, no. 8, pp. 4961–4965, Apr. 1983. [Online]. Available: http://link.aps.org/doi/10.1103/PhysRevB.27.4961

[42] M. J. W. L.-M. Peng, S. L. Dudarev, *High Energy Electron Diffraction and Microscopy*. Oxford University Press, 2004.

[43] G. Heger, "Symmetry of crystals," in *Laboratory Course Neutron Scattering Lectures*. Forschungszentrum Jülich GmbH, 2014.

[44] J. Gustafson, M. Shipilin, C. Zhang, A. Stierle, U. Hejral, U. Ruett, O. Gutowski, P.-A. Carlsson, M. Skoglundh, and E. Lundgren, "High-energy surface x-ray diffraction for fast surface structure determination," *Science*, vol. 343, no. 6172, pp. 758–761, 2014. [Online]. Available: http://www.sciencemag.org/content/343/6172/758.abstract

[45] J. Neave, B. Joyce, P. Dobson, and N. Norton, "Dynamics of film growth of GaAs by MBE from RHEED observations," vol. 31, no. 1, pp. 1–8–, 1983. [Online]. Available: http://dx.doi.org/10.1007/BF00617180

[46] D. G. Schlom, J. N. Eckstein, E. S. Hellman, S. K. Streiffer, J. S. Harris, M. R. Beasley, J. C. Bravman, T. H. Geballe, C. Webb, K. E. von Dessonneck, and F. Turner, "Molecular beam epitaxy of layered D-Ba-Cu-O compounds," *Applied Physics Letters*, vol. 53, no. 17, pp. 1660–1662, 1988. [Online]. Available: http://scitation.aip.org/content/aip/journal/apl/53/17/10.1063/1.100443

[47] J. Haeni, C. Theis, and D. Schlom, "RHEED intensity oscillations for the stoichiometric growth of SrTiO3 thin films by reactive molecular beam epitaxy," vol. 4, no. 2-3, pp. 385–391–, 2000. [Online]. Available: http://dx.doi.org/10.1023/A%3A1009947517710

[48] J. Klein, C. Höfener, L. Alff, and R. Gross, "In situ monitoring of the growth of oxide thin films at high oxygen pressure," *Superconductor Science and Technology*, vol. 12, no. 11, pp. 1023–, 1999. [Online]. Available: http://stacks.iop.org/0953-2048/12/i=11/a=398

[49] B. Mercey, P. A. Salvador, P. Lecoeur, W. Prellier, M. Hervieu, C. Simon, D. Chippaux, A. M. Haghiri-Gosnet, and B. Raveau, "In-situ monitoring of the growth and characterization of $(PrMnO3)_n/(SrMnO3)_n$ superlattices," *Journal of Applied Physics*, vol. 94, no. 4, pp. 2716–2724, 2003.

[50] S. Franchi, "Chapter 1 - molecular beam epitaxy: fundamentals, historical background and future prospects," in *Molecular Beam Epitaxy*, M. Henini, Ed. Oxford: Elsevier, 2013, no. A2, pp. 1–46. [Online]. Available: http://www.sciencedirect.com/science/article/pii/B9780123878397000014

[51] A. Glavic, "Multiferroicity in oxide thin films and heterostructures," Ph.D. dissertation, RWTH Aachen, 2012.

[52] W.-K. Chu, J. W. Mayer, and M.-A. Nicolet, "Chapter 4 - backscattering spectrometry of thin films," in *Backscattering Spectrometry*. Academic Press, 1978, pp. 89–122. [Online]. Available: http://www.sciencedirect.com/science/article/pii/B9780121738501500090

[53] U. Rücker, W. Bergs, B. Alefeld, E. Kentzinger, and T. Brückel, "Polarization analysis for the 2D position-sensitive detector of the HADAS reflectometer in Jülich," *Physica B: Condensed Matter*, vol. 297, no. 1-4, pp. 140–142, Mar. 2001. [Online]. Available: http://www.sciencedirect.com/science/article/pii/S0921452600008565

[54] V. Lauter, H. Ambaye, R. Goyette, W.-T. Hal Lee, and A. Parizzi, "Highlights from the magnetism reflectometer at the SNS," *Physica B: Condensed Matter*, vol. 404, no. 17, pp. 2543–2546, Sep. 2009. [Online]. Available: http://www.sciencedirect.com/science/article/pii/S092145260900369X

[55] S. P. Stefan Mattauch, Alexandros Koutsioubas, "MARIA: Magnetic reflectometer with high incident angle," *Journal of large-scale research facilities*, vol. 1, p. A8, 2015. [Online]. Available: https://jlsrf.org/index.php/lsf/article/view/29

[56] T. G. Jürgen Thomas, *Analytische Transmissionselektronenmikroskopie: Eine Einführung für den Praktiker*. Springer, 2013.

[57] C. B. C. David B. Williams, *Transmission Electron Microscopy: A Textbook for Materials Science*. Springer.

[58] K. T. Doris Meertens, Max Kruth, "FEI Helios NanoLab 400S FIB-SEM," *Journal of large-scale research facilities*, vol. 2, p. A60, 2016.

[59] A. Krehan, A. Vogt, and W. Gruenewald, "New ion beam milling system for fast and efficient site specific sample preparation," *Microscopy and Microanalysis*, vol. 10, no. SupplementS02, pp. 956–957, 2004. [Online]. Available: http://dx.doi.org/10.1017/S1431927604881054

[60] [Online]. Available: http://www.microscopyconsumables.se/tem/grids-omniprobe

[61] [Online]. Available: https://www.fei.com/products/tem/tecnai

[62] K. T. Marc Heggen, Martina Luysberg, "FEI Titan 80-300 STEM," *Journal of large-scale research facilities*, vol. 2, p. A42.

[63] S. Pennycook, "Z-contrast stem for materials science," *Ultramicroscopy*, vol. 30, no. 1, pp. 58–69, 1989. [Online]. Available: http://www.sciencedirect.com/science/article/pii/0304399189901733

[64] *N9410-90001 Agilent 5500 SPM Users Guide*, Rev b-5 ed. Agilent Technologies, Inc., August 2009.

[65] P. Schöffmann, "Untersuchung von dünnen Oxidschichten mit dem Rasterkraftmikroskop," Bachelor thesis, TU München, 2014.

[66] C.-M. C. Michel A. Van Hove, William H. Weinberg, *Low-Energy Electron Diffraction. Experiment, Theory and Surface Structure Determination*, ser. Springer Series in Surface Sciences, 1986, vol. 6.

[67] H. Y. Hwang, "Perovskites - oxygen vacancies shine blue," *Nature Materials*, vol. 4, no. 11, pp. 803–804, Nov. 2005.

[68] E. S. Vlakhov, T. I. Donchev, A. Y. Spasov, K. Dorr, K. A. Nenkov, A. Handstein, S. Pignard, and H. Vincent, "Structural and magnetotransport properties of magnetron sputtered $La_{0.7}Sr_{0.3}MnO_3$ thin films," *Vacuum*, vol. 69, no. 1-3, pp. 249–253, Dec. 2002.

[69] S. Majumdar, H. Huhtinen, H. S. Majumdar, and P. Paturi, "Stress and defect induced enhanced low field magnetoresistance and dielectric constant in $La_{0.7}Sr_{(0.3}MnO_3$ thin films," *Journal of Alloys and Compounds*, vol. 512, no. 1, pp. 332–339, Jan. 2012.

[70] D. Pesquera, M. Wojcik, E. Jedryka, V. Laukhin, N. Dix, F. Sanchez, G. Herranz, and J. Fontcuberta, "Interface and bulk charge localization in manganite thin films," *Adv. Mater. Interfaces*, vol. 1, no. 6, pp. n/a–n/a, 2014. [Online]. Available: http://dx.doi.org/10.1002/admi.201400079

[71] S. Gregory, "Magnetic susceptibility of oxygen adsorbed on graphite," *Phys. Rev. Lett.*, vol. 40, no. 11, pp. 723–725, Mar. 1978. [Online]. Available: http://link.aps.org/doi/10.1103/PhysRevLett.40.723

[72] P. Orgiani, C. Aruta, R. Ciancio, A. Galdi, and L. Maritato, "Enhanced transport properties in $La_xMnO_{3-\delta}$ thin films epitaxially grown on $SrTiO_3$ substrates: The profound impact of the oxygen content," *Appl. Phys. Lett.*, vol. 95, no. 1, pp. 013 510–3, Jul. 2009. [Online]. Available: http://dx.doi.org/10.1063/1.3168649

[73] P. Orgiani, A. Galdi, C. Aruta, V. Cataudella, G. De Filippis, C. A. Perroni, V. Marigliano Ramaglia, R. Ciancio, N. B. Brookes, M. Moretti Sala, G. Ghiringhelli, and L. Maritato, "Multiple double-exchange mechanism by Mn^{2+} doping in manganite compounds," *Phys. Rev. B*, vol. 82, no. 20, pp. 205 122–, Nov. 2010. [Online]. Available: http://link.aps.org/doi/10.1103/PhysRevB.82.205122

[74] A. Galdi, C. Aruta, P. Orgiani, N. B. Brookes, G. Ghiringhelli, M. Moretti Sala, R. V. K. Mangalam, W. Prellier, U. Lüders, and L. Maritato, "Magnetic properties and orbital anisotropy driven by Mn^{2+} in nonstoichiometric $La_xMnO_{3-\delta}$ thin films," *Phys. Rev. B*, vol. 83, no. 6, pp. 064 418–, Feb. 2011. [Online]. Available: http://link.aps.org/doi/10.1103/PhysRevB.83.064418

[75] W. Braun, *Applied RHEED: Reflection High-Energy Electron Diffraction During Crystal Growth*. Springer Berlin Heidelberg, 1999.

[76] R. A. Cowley, "The phase transition of strontium titanate," *Philosophical Transactions of the Royal Society of London A: Mathematical, Physical and Engineering Sciences*, vol. 354, no. 1720, pp. 2799–2814, Dec. 1996. [Online]. Available: http://rsta.royalsocietypublishing.org/content/354/1720/2799.abstract

[77] Y. Lin, A. E. Becerra-Toledo, F. Silly, K. R. Poeppelmeier, M. R. Castell, and L. D. Marks, "The (2 x 2) reconstructions on the $SrTiO_3$ (001) surface: A combined scanning tunneling microscopy and density functional theory study," *Surface Science*, vol. 605, no. 17-18, pp. L51–L55, Sep. 2011. [Online]. Available: http://www.sciencedirect.com/science/article/pii/S0039602811002287

[78] E. Beyreuther, A. Thiessen, S. Grafström, K. Dörr, and L. M. Eng, "Large photoconductivity of oxygen-deficient $La_{0.7}Ca_{0.3}MnO_3/SrTiO_3$ heterostructures," *Journal of Physics: Condensed Matter*, vol. 22, no. 17, pp. 175 506–, 2010. [Online]. Available: http://stacks.iop.org/0953-8984/22/i=17/a=175506

[79] J. A. Bock, S. Lee, S. Trolier-McKinstry, and C. A. Randall, "Metallic-like to nonmetallic transitions in a variety of heavily oxygen deficient ferroelectrics," *Applied Physics Letters*, vol. 107, no. 9, p. 092902, 2015. [Online]. Available: http://scitation.aip.org/content/aip/journal/apl/107/9/10.1063/1.4929879

[80] D. A. Mota, Y. Romaguera-Barcelay, A. Tkach, J. P. de la Cruz, P. M. Vilarinho, P. B. Tavares, J. A. Moreira, and A. Almeida, "Induced polarized state in intentionally grown oxygen deficient $KTaO_3$ thin films," *J. Appl. Phys.*, vol. 114, no. 3, pp. 034 101–8, Jul. 2013. [Online]. Available: http://dx.doi.org/10.1063/1.4813324

[81] A. Lopez-Bezanilla, P. Ganesh, and P. B. Littlewood, "Research update: Plentiful magnetic moments in oxygen deficient $SrTiO_3$," *APL Materials*, vol. 3, no. 10, p. 100701, 2015. [Online]. Available: http://scitation.aip.org/content/aip/journal/aplmater/3/10/10.1063/1.4932347

[82] P. Orgiani, A. Y. Petrov, R. Ciancio, A. Galdi, L. Maritato, and B. A. Davidson, "Evidence of direct correlation between out-of-plane lattice parameter and metal-insulator transition temperature in oxygen-depleted manganite thin films," *Applied Physics Letters*, vol. 100, no. 4, p. 042404, 2012. [Online]. Available: http://link.aip.org/link/?APL/100/042404/1

[83] C. Schlueter, P. Orgiani, T.-L. Lee, A. Y. Petrov, A. Galdi, B. A. Davidson, J. Zegenhagen, and C. Aruta, "Evidence of electronic band redistribution in $La_{0.65}Sr_{0.35}MnO_{3-\delta}$ by hard x-ray photoelectron spectroscopy," *Phys. Rev. B*, vol. 86, no. 15, pp. 155 102–, Oct. 2012. [Online]. Available: http://link.aps.org/doi/10.1103/PhysRevB.86.155102

[84] M. D. Kuz'min, "Shape of temperature dependence of spontaneous magnetization of ferromagnets: Quantitative analysis," *Phys. Rev. Lett.*, vol. 94, no. 10, pp. 107 204–, Mar. 2005. [Online]. Available: http://link.aps.org/doi/10.1103/PhysRevLett.94.107204

[85] O. Yefanov, V. Kladko, M. Slobodyan, and Y. Polischuk, "XVis: an educational open-source program for demonstration of reciprocal-space construction and diffraction principles," *Journal of Applied Crystallography*, vol. 41, no. 3, pp. 647–652, 2008. [Online]. Available: http://dx.doi.org/10.1107/S0021889808008625

[86] P. F. Fewster, "Reciprocal space mapping," *Critical Reviews in Solid State and Materials Sciences*, vol. 22, no. 2, pp. 69–110, Jun. 1997. [Online]. Available: http://dx.doi.org/10.1080/10408439708241259

[87] E. E. Fullerton, I. K. Schuller, H. Vanderstraeten, and Y. Bruynseraede, "Structural refinement of superlattices from x-ray-diffraction," *Physical Review B*, vol. 45, no. 16, pp. 9292–9310, 1992.

[88] A. Paul, N. Paul, J. Jutimoosik, R. Yimnirun, S. Rujirawat, B. Höpfner, I. Lauermann, M. Lux-Steiner, S. Mattauch, and P. Böni, "Change in interface magnetism of an exchange-coupled system due to the presence of nonmagnetic spacers," *Phys. Rev. B*, vol. 87, no. 1, pp. 014 431–, Jan. 2013. [Online]. Available: http://link.aps.org/doi/10.1103/PhysRevB.87.014431

[89] J. McCord, "Progress in magnetic domain observation by advanced magneto-optical microscopy," *Journal of Physics D: Applied Physics*, vol. 48, no. 33, pp. 333 001–, 2015. [Online]. Available: http://stacks.iop.org/0022-3727/48/i=33/a=333001

[90] M. Bjorck and G. Andersson, "Genx: an extensible X-ray reflectivity refinement program utilizing differential evolution," *Journal of Applied Crystallography*, vol. 40, pp. 1174–1178, Dec. 2007.

[91] W. Jauch and A. Palmer, "Anomalous zero-point motion in $SrTiO_3$ results from γ-ray diffraction," *Phys. Rev. B*, vol. 60, no. 5, pp. 2961–2963, Aug. 1999. [Online]. Available: http://link.aps.org/doi/10.1103/PhysRevB.60.2961

[92] A. Steffen, A. Glavic, O. Holderer, H. Frielinghaus, H. Ambaye, S. Pütter, and T. Brückel, "Frozen O2 layer revealed by neutron reflectometry," *Results in Physics*, vol. 6, pp. 263–264, 2016. [Online]. Available: http://www.sciencedirect.com/science/article/pii/S2211379716300298

[93] S.-H. Bo, F. Wang, Y. Janssen, D. Zeng, K.-W. Nam, W. Xu, L.-S. Du, J. Graetz, X.-Q. Yang, Y. Zhu, J. B. Parise, C. P. Grey, and P. G. Khalifah, "Degradation and (de)lithiation processes in the high capacity battery material $LiFeBO_3$," *J. Mater. Chem.*, vol. 22, no. 18, pp. 8799–8809, 2012. [Online]. Available: http://dx.doi.org/10.1039/C2JM16436A

[94] T. A. Pham, A. Schreiber, E. V. Sturm (nee Rosseeva), S. Schiller, and H. Cölfen, "Hemolysin coregulated protein 1 as a molecular gluing unit for the assembly of nanoparticle hybrid structures," *Beilstein Journal of Nanotechnology*, vol. 7, pp. 351–363, 2016.

[95] T. Rieger, D. Grutzmacher, and M. I. Lepsa, "Misfit dislocation free InAs/GaSb core-shell nanowires grown by molecular beam epitaxy," *Nanoscale*, vol. 7, no. 1, pp. 356–364, 2015. [Online]. Available: http://dx.doi.org/10.1039/C4NR05164E

[96] C. Gomez-Navarro, J. C. Meyer, R. S. Sundaram, A. Chuvilin, S. Kurasch, M. Burghard, K. Kern, and U. Kaiser, "Atomic structure of reduced graphene oxide," *Nano Lett.*, vol. 10, no. 4, pp. 1144–1148, Apr. 2010. [Online]. Available: http://dx.doi.org/10.1021/nl9031617

[97] D. Necas and P. Klapetek, "Gwyddion: an open-source software for SPM data analysis," *Central European Journal of Physics*, vol. 10, no. 1, pp. 181–188, Feb. 2012.

[98] R. Pynn, *Neutron scattering - A primer*, 1990. [Online]. Available: https://www.ncnr.nist.gov/summerschool/ss14/pdf/NeutronScatteringPrimer.pdf

[99] *MPMS Application Note 1014-210B: Oxygen Contamination*, Quantum Design Std., 1997.

[100] R. B. B. Boucher and M. Perrin, "Magnetic structure of Mn_3O_4 by neutron diffraction," *J. Appl. Phys.*, vol. 42, p. 1615, 1971.

[101] D. Mukherjee, N. Bingham, M. Hordagoda, M.-H. Phan, H. Srikanth, S. Witanachchi, and P. Mukherjee, "Influence of microstructure and interfacial strain on the magnetic properties of epitaxial $Mn_3O_4/La_{0.7}Sr_{0.3}MnO_3$ layered-composite thin films," *J. Appl. Phys.*, vol. 112, no. 8, pp. 083 910–8, Oct. 2012. [Online]. Available: http://dx.doi.org/10.1063/1.4759237

[102] Y. Ishii, H. Sato, A. Sawa, T. Yamada, H. Akoh, K. Endo, M. Kawasaki, and Y. Tokura, "Precipitate-free films of $La_{1-x}Sr_xMnO_3$ grown on the substrates with artificial step edges," *Applied Physics Letters*, vol. 85, no. 17, pp. 3800–3802, 2004. [Online]. Available: http://scitation.aip.org/content/aip/journal/apl/85/17/10.1063/1.1807969

[103] B. Vertruyen, R. Cloots, M. Ausloos, J.-F. Fagnard, and P. Vanderbemden, "Electrical transport and percolation in magnetoresistive manganite/insulating oxide composites: Case of $La_{0.7}Ca_{0.3}MnO_3/Mn_3O_4$," *Phys. Rev. B*, vol. 75, no. 16, pp. 165 112–, Apr. 2007. [Online]. Available: http://link.aps.org/doi/10.1103/PhysRevB.75.165112

[104] D. Mukherjee, N. Bingham, M.-H. Phan, H. Srikanth, P. Mukherjee, and S. Witanachchi, "Ziz-zag interface and strain-influenced ferromagnetism in epitaxial $Mn_3O_4/La_{0.7}Sr_{0.3}MnO_3$ thin films grown on SrTiO3 (100) substrates," *Journal of Applied Physics*, vol. 111, no. 7, p. 07D730, 2012. [Online]. Available: http://scitation.aip.org/content/aip/journal/jap/111/7/10.1063/1.3680531

[105] B. Kirby, H. Belliveau, D. Belyea, P. Kienzle, A. Grutter, P. Riego, A. Berger, and C. W. Miller, "Spatial evolution of the ferromagnetic phase transition in an exchange graded film," *Phys. Rev. Lett.*, vol. 116, no. 4, pp. 047 203–, Jan. 2016. [Online]. Available: http://link.aps.org/doi/10.1103/PhysRevLett.116.047203

[106] J. Van Den Boomgaard, D. Terrell, R. Born, and H. Giller, "An in situ grown eutectic magnetoelectric composite material," vol. 9, no. 10, pp. 1705–1709–, 1974. [Online]. Available: http://dx.doi.org/10.1007/BF00540770

[107] N. Ortega, A. Kumar, J. F. Scott, and R. S. Katiyar, "Multifunctional magnetoelectric materials for device applications," *Journal of Physics: Condensed Matter*, vol. 27, no. 50, pp. 504 002–, 2015. [Online]. Available: http://stacks.iop.org/0953-8984/27/i=50/a=504002

[108] A. David, Y. Tian, P. Yang, X. Gao, W. Lin, A. B. Shah, J.-M. Zuo, W. Prellier, and T. Wu, "Colossal positive magnetoresistance in surface-passivated oxygen-deficient strontium titanite," *Sci. Rep.*, vol. 5, pp. –, May 2015. [Online]. Available: http://dx.doi.org/10.1038/srep10255

List of Figures

List of Tables

Appendix A

List of relevant samples

For this work, multiple samples were produced and investigated. This list was prepared to give an overview over the samples.

Table A.1: List of relevant samples; nominal stoichiometry in brackets

Deposition method	Sample series	Sample name	Section (page)
Co-deposition	Growth parameters	049 056 059	C.1.1 (147)
		134	4.2.5 (41)
	Reproducibility	156 159 160 165 166 168	5.1 (47)
		196	5.3 (54)
Co- and shuttered deposition	calibration sample	296	4.3.1 (45)
Shuttered deposition	constant stoichiometry	228	3.2 (26)
		291 ($(LS)_4M_3O$)	4.3 (41)
		301 (pure LSMO)	6.1 (59)
		288 ($(LS)_2M_1O$) 292 ($(LS)_3M_2O$)	6.2 (60)
	Gradients	224 (top Mn excess) 230 (edged Mn excess) 233 (centered Mn excess)	6.3 (63)

Appendix B

MBE-related scripts

The used Oxide MBE has a state-of-the-art surveillance for sample preparation. Data were produced during rate calibration, during sample growth and for inside-MBE structural characterization. In the following section, the used tools to handle the data and their output are shown and described.

B.1 Logfiles

B.1.1 Effusion cell calibration

For rate calibration, the information Δ frequency vs. time had to be monitored and a stable, element-specific Hz/s value was targeted. During sample preparation, this was performed inside the MBE surveillance program of DCA.

The logfiles, providing with quartz crystal frequency, element-specific effusion cell temperature and shutter opening time, were after calibration plotted for calibration traceability via applying the python file in listing B.1. This file creates a png image and a gnuplot file in listing B.2 to afterwards modify the png (e.g. zoom inside the time axis).

The program scans which element shutters were opened to then plot that information as a colored rectangle with top value as targeted rate. The frequency change is plotted. The temperatures of the cells opened during the recording time are plotted as difference from their final value $\pm$ 12 °C. If the Δtemperature curves are visible inside the image, this is a sign of a stable temperature, e.g. for La, 24 °C/1670 °C is a variation of less than 1.5 %.

To load in the data, the file "mbe.py" of Plot-Script[31] was utilized.

Listing B.1: Logfile rate visualization: Python file

```
'''
Version 0.9 - works, but has to be improved
- include the E-Guns as material
- seperate title in .gpl file to create 2014/08/07 14:07 instead of 201408071407
- check if tempmaterial and shuttermaterial entries are identical
- check for "1" in shutter column to plot temperature and shutter column
- search for column frequency instead of using the last column of the document
- reduce import instances
'''

#check what is needed here in detail
import os, sys, re
import subprocess
```

```
import numpy
import mbe as read_data

logfile = read_data.read_data(sys.argv[1])[0] #[0] necessary for output syntax in mbe.py:
    return [output]

#Lists which might have to be modified; used for color&frequency dictionaries
color_element = ['La', 'Mn', 'Co', 'Pt', 'Fe', 'Sr', 'Ti', 'Gun1', 'Gun2']
color_code = ['\#5AC449', '\#A8089E', '\#00005D', '\#747489', '\#8B6914', '\#12DC0F', '\#
    A52A2A', '\#BFBFBF', '\#FF0000']
freq_target = [0.1199, 0.0825, 0.02, 0.02, 0.02, 0.0658, 0.02, 0.02, 0.02]

#seperate "Cell#4-La" from "Shutter" to be able to search for material output, shutter,
    temperature
words = []
for i in range(len(logfile.dimensions())):
    words.append(logfile.dimensions()[i].split('␣'))

#search for shutter columns, save material name as "shuttermaterial", save column number as "
    shuttercol"
zwischen = []
shuttermaterial = []
shuttercol = []
for i, word in enumerate(words):
    if len(word) > 1:
        if word[1] == 'Shutter':
# if word[0] != 'Plasma' and word[0] != 'Manipulator':
            if not word[0] == 'Plasma':
                if not word[0] == 'Manipulator':
                    zwischen.append(word[0].split('-'))
#                     shuttermaterial.append((word[0].split('-'))[1]) direkt anhaengen
                    shuttercol.append(i)
#         if re.search(r"^E-Gun", cellname[0]) is not None:
#             parts2 = cellname[0].split('-')
#         return parts2[1]
#shuttercol.append(parts2[1])
for i in range(len(zwischen)):
    shuttermaterial.append(zwischen[i][1])

#search for temperature columns, save material name as "tempmaterial", save column number as "
    tempcol", save final value of temperature as "tempEnd"
tempcol = []
tempzwischen = []
tempEnd = []
for i in shuttercol:
    if words[i+1][1] == 'Temperature':
        tempcol.append(i+1)
        tempzwischen.append(words[i+1][0].split('-'))
        tempEnd.append(str(logfile.data[i+1][-1]).strip("[]"))
tempmaterial = []
for i in range(len(tempzwischen)):
    tempmaterial.append(tempzwischen[i][1])

#color&frequency dictionaries
#color_element are the possible materials, color_code are the individual colors for each
    element
#sorted_elements contains used materials inside logfile, sorted_color provides with color code
     for sorted_elements, sorted_freq with targeted delta frequency for sorted_elements
#dict to further use color_dictionary['(element)'] to get the colorcode for each element
color_dictionary = dict(zip(color_element, color_code))
freq_dictionary = dict(zip(color_element, freq_target))
sorted_elements=[]
sorted_color=[]
sorted_freq=[]
for key in shuttermaterial: #key in state_vector.keys():
    sorted_color.append(color_dictionary['{}'.format(key)])
    sorted_freq.append(freq_dictionary['{}'.format(key)])
    sorted_elements.append(key)

'''
Start gnuplot script: Plot the derivative of frequency vs. time, plot the temperature
    difference of effusion cells from final value,
```

```
    #indicate via rectangle if shutter element was open, upper limit showing the targeted element-
        specific delta frequency value
    '''
    logfilename = "{}.gpl".format(os.path.splitext(os.path.basename(sys.argv[1]))[0])
81  tu=os.path.splitext(os.path.basename(sys.argv[1]))[0]
    with open("%s" % logfilename, "w") as myfile:
        myfile.write('#set terminal windows font "Arial,16"'+'\n')
        myfile.write('#set size 900,700\n')
        myfile.write('set term pngcairo enhanced size 800,600 font "Arial,18" lw 2 nocrop\n')
86      myfile.write('set output "{}.png"'.format(os.path.splitext(os.path.basename(sys.argv[1]))
            [0])+'\n\n')
    #     myfile.write('set grid'+'\n'+'set title "{}"'.format(os.path.splitext(os.path.basename(
        sys.argv[1]))[0])+'\n')
        myfile.write('set grid'+'\n'+'set title "Logfile started at {}/{}/{} {}:{}:{}"'.format(tu
            [0:2],tu[2:4],tu[4:6],tu[6:8],tu[8:10],tu[10:12])+'\n')
        myfile.write('set xlabel "Time (h)"'+'\n'+'set ylabel "Freq. change (-Hz/s)"'+'\n'+'set
            y2label "Temperature ({/Symbol \260}C)"'+'\n')
        myfile.write('set key bmargin'+'\n'+'set style fill transparent solid 0.5')
91      myfile.write('\n'+'set y2tics 10'+'\n')
        myfile.write('set y2range [-12:12]'+'\n')
        myfile.write('set yrange[0.6*'+str(min(sorted_freq))+':'+str(max(sorted_freq))+'*1.1]'+'\n
            ')
        myfile.write('x1=0; y1=0; x2=0; y2=0'+'\n')
        myfile.write('derivative(x,y)=(y1=y2, x1=x2, x2=x, y2=y, ($0>0 ? (y2-y1)/(x2-x1) : 1/0))
            '+'\n')
96      myfile.write('\n\n')
        myfile.write('shuttercol=\"'+str(shuttercol).strip('[]')+'\"\n')
        myfile.write('sorted_color=\"')
        myfile.write(' '.join(sorted_color)+'\"\n')
        myfile.write('sorted_elements=\"')
101     myfile.write(' '.join(sorted_elements)+'\"\n')
        myfile.write('tempcol=\"'+str(tempcol).strip('[]')+'\"\n')
        myfile.write('tempEnd=\"')
        myfile.write(' '.join(tempEnd)+'\"\n')
        myfile.write('sorted_freq=\"'+str(sorted_freq).strip("[]")+'\"\n')
106     myfile.write('item_shuttercol(n)=word(shuttercol,n)'+'\n')
        myfile.write('item_sorted_color(n)=word(sorted_color,n)'+'\n')
        myfile.write('item_sorted_elements(n)=word(sorted_elements,n)'+'\n')
        myfile.write('item_tempEnd(n)=word(tempEnd,n)'+'\n')
        myfile.write('item_tempcol(n)=word(tempcol,n)'+'\n')
111     myfile.write('item_sorted_freq(n)=word(sorted_freq,n)'+'\n')
        myfile.write("plot '{}'".format(os.path.basename(sys.argv[1]))+' using ')
        myfile.write('($1/3600):($1>0 ?(-1*derivative($1,'+str(len(logfile.data))+')):1/0)
            every 2 t "Rate" w lines lw 1.5 lc rgb "#000000",')
        myfile.write("for [i=1:words(sorted_elements)] '{}'".format(os.path.basename(sys.argv[1]))
            +' using ($1/3600):(column(item_tempcol(i)+1)-item_tempEnd(i)) axes x1y2 t ""."(
            item_sorted_elements(i))." {/Symbol D}Temperature" w lines lw 3 lc rgb
            item_sorted_color(i),')
        myfile.write("for [i=1:words(sorted_elements)] '{}'".format(os.path.basename(sys.argv[1]))
            +' using ($1/3600):((column(item_shuttercol(i)+1)*0.01)+item_sorted_freq(i)-0.01) w
            filledcurves y1=item_sorted_freq(i)-0.01 title "".(item_sorted_elements(i))."-Shutter"
            lc rgb item_sorted_color(i) axes x1y1\n')
116     myfile.write('exit')

    #following stuff for automatically created .png via gnuplot
    proc = subprocess.Popen(['gnuplot','-p'],
                            stdin=subprocess.PIPE,
121                         )
    proc.stdin.write('load "{}"'.format(os.path.splitext(os.path.basename(sys.argv[1]))[0])+'.gpl"
        \n')
    proc.communicate()
```

Listing B.2: Logfile rate visualization: Gnuplot file

```
    #set terminal windows font "Arial,16"
2   #set size 900,700
    set term pngcairo enhanced size 800,600 font "Arial,18" lw 2 nocrop
    set output "140806102152.png"

    set grid
7   set title "Logfile started at 14/08/06 10:21:52"
```

```
set xlabel "Time (h)"
set ylabel "Freq. change (-Hz/s)"
set y2label "Temperature ({/Symbol °}C)"
set key bmargin
set style fill transparent solid 0.5
set y2tics 10
set y2range [-12:12]
set yrange[0.6*0.0658:0.1199*1.1]
x1=0; y1=0; x2=0; y2=0
derivative(x,y)=(y1=y2, x1=x2, x2=x, y2=y, ($0 > 0 ? (y2-y1)/(x2-x1) : 1/0))


shuttercol="3, 6, 9"
sorted_color="\#5AC449 \#12DC0F \#A8089E"
sorted_elements="La Sr Mn"
tempcol="4, 7, 10"
tempEnd="1545.0 511.0 1075.0"
sorted_freq="0.1199, 0.0658, 0.0825"
item_shuttercol(n)=word(shuttercol,n)
item_sorted_color(n)=word(sorted_color,n)
item_sorted_elements(n)=word(sorted_elements,n)
item_tempEnd(n)=word(tempEnd,n)
item_tempcol(n)=word(tempcol,n)
item_sorted_freq(n)=word(sorted_freq,n)
plot '140806102152.log' using ($1/3600): ($1 >0 ? (-1*derivative($1,$23)):1/0) every 2 t "Rate
    " w lines lw 1.5 lc rgb "#000000", for [i=1:words(sorted_elements)] '140806102152.log'
    using ($1/3600):(column(item_tempcol(i)+1)-item_tempEnd(i)) axes x1y2 t "".(
    item_sorted_elements(i))." {/Symbol D}Temperature" w lines lw 3 lc rgb item_sorted_color(i
    ), for [i=1:words(sorted_elements)] '140806102152.log' using ($1/3600):((column(
    item_shuttercol(i)+1)*0.01)+item_sorted_freq(i)-0.01) w filledcurves y1=item_sorted_freq(i
    )-0.01 title "".(item_sorted_elements(i))."-Shutter" lc rgb item_sorted_color(i) axes x1y1
exit
```

B.1.2 Logfile during growth visualization

With respect to the gnuplot output of the calibration logfile, the following script in listing B.3 was modified in terms of input file (line 3), title (line 4), displayed time (line 6 and 7) and used column numbers (line 26). The so created image was used to check if the used recipe was processed correctly. Additionally, for oxide samples the values for forwarded and reflected plasma were displayed to verify the oxygen content inside the chamber during growth.

Listing B.3: Logfile during growth visualization

```
set terminal windows enhanced font "Arial,18" size 900, 600

blubb = "130711123040.log"

set title "168ab-LSMO-STO"
set xrange [15000:21000]
set x2range [15000:21000]

set grid
set yrange [1:4]
set y2range [:260]
set y2tics 50
set ylabel "Shutter"
set y2label "Power [W]"
set xlabel "Time [s]"
set key bmargin
set ytics ("Mn" 1.5, "La, Sr" 2.5)
set format x "%.te%T"

##5AC449 is green, #A8089E violet, "#FFA500" yellow

set style fill transparent solid 0.5
```

```
columncolor="#FFA500 #A8089E #5AC449 #FF0000"      ##5AC449 is green, #A8089E violet,
Element="Forw. Plasma Mn La Ref. Plasma"      #126E0D modified green for Sr, "#FFA500" yellow, "#
    FF0000" red
Colu = "15 11 2 16"                                  #temperature columns

item_colcol(n)=word(columncolor,n)
item_E(n) = word(Element,n)
item_C(n) = int(word(Colu,n))            #column(item_C) only works if item_C is defined as
    integer, not word


plot for [i=1:1] blubb using ($1):(column(item_C(i))) w filledcurves x1 title "".(item_E(i))
    lc rgb item_colcol(i) axes x2y2,\
for [i=2:3] blubb using ($1):(column(item_C(i))+i-1) w filledcurves y1=i-1 title "".(item_E(i)
    ) lc rgb item_colcol(i) axes x1y1, \
for [i=4:4] blubb using ($1):(column(item_C(i))) w filledcurves x1 title "".(item_E(i)) lc rgb
     item_colcol(i) axes x2y2
```

B.1.3 MBE recipes of the samples presented in this work

All samples were grown via recipe. Already for the simplest possible sample growth, wait for a precise shutter opening interval, the recipe provides with an easy way of reproducibility. Later, complicated MBE recipe structures with varying shutter opening interval for different effusion cell materials during growth of one sample were realized. An example recipe for co-deposition is shown in listing B.4, for half-shuttered deposition in listing B.5, fully shuttered deposition in listing B.6 and for a stoichiometric gradient in listing B.7

Listing B.4: Co-deposition

```
Total Time: 5400.0
Wait Until Manipulator Temperature > 899.0
Open Cell#3_La
Open Cell#5_Sr
Open Cell#6_Mn
Open Plasma
Pause 5400.0
Close Cell#3_La
Close Cell#5_Sr
Close Cell#6_Mn
Set Manipulator Ramp Rate 20.0
Set Manipulator Setpoint 20.0
Set Cell#3_La Setpoint 500.0
Set Cell#5_Sr Setpoint 500.0
Set Cell#6_Mn Setpoint 500.0
Wait Until Manipulator Temperature < 100.0
Close MFC
Set Plasma Flow 0.020

End
```

Listing B.5: Half-shuttered deposition

```
Total Time: 5456.0
Open Cell#3_La
Open Cell#5_Sr
Open Cell#6_Mn
While Loop 22
Close Cell#3_La
Close Cell#5_Sr
Pause 62.0
Open Cell#3_La
Open Cell#5_Sr
Pause 186.0
While End
Close Cell#3_La
Close Cell#5_Sr
Close Cell#6_Mn
Set Manipulator Ramp Rate 20.0
Set Manipulator Setpoint 20.0
Wait Until Manipulator Temperature < 100.0
Close MFC
Set Plasma Flow 0.020
End
```

Listing B.6: Fully shuttered deposition

```
Total Time: 3468.0
While Loop 25
While Loop 2
Open Cell#4_La
Open Cell#5_Sr
Pause 68.0
Close Cell#4_La
Close Cell#5_Sr
Open Cell#6_Mn
Pause 68.0
Close Cell#6_Mn
While End
Open Cell#4_La
Open Cell#5_Sr
Pause 68.0
Close Cell#4_La
Close Cell#5_Sr
While End

Set Manipulator Ramp Rate 20.0
Set Manipulator Setpoint 20.0
Wait Until Manipulator Temperature < 100.0
End
```

Listing B.7: Fully shuttered gradient deposition

```
Total Time: 9120.0
Open Cell#6_Mn
Pause 60.0
Close Cell#6_Mn

While Loop 8
Open Cell#3_La
Open Cell#5_Sr
Pause 60.0
Close Cell#5_Sr
Close Cell#3_La
Open Cell#6_Mn
Pause 60.0
Close Cell#6_Mn
While End

Open Cell#6_Mn
Pause 60.0
Close Cell#6_Mn

While Loop 7
Open Cell#3_La
Open Cell#5_Sr
Pause 60.0
Close Cell#5_Sr
Close Cell#3_La
Open Cell#6_Mn
Pause 60.0
Close Cell#6_Mn
While End

Open Cell#6_Mn
Pause 60.0
Close Cell#6_Mn

While Loop 7
Open Cell#3_La
Open Cell#5_Sr
Pause 60.0
Close Cell#5_Sr
Close Cell#3_La
```

```
42  Open Cell#6_Mn
    Pause 60.0
    Close Cell#6_Mn
    While End

47  Open Cell#6_Mn
    Pause 60.0
    Close Cell#6_Mn

    While Loop 6
52  Open Cell#3_La
    Open Cell#5_Sr
    Pause 60.0
    Close Cell#5_Sr
    Close Cell#3_La
57  Open Cell#6_Mn
    Pause 60.0
    Close Cell#6_Mn
    While End

62  Open Cell#6_Mn
    Pause 60.0
    Close Cell#6_Mn

    While Loop 6
67  Open Cell#3_La
    Open Cell#5_Sr
    Pause 60.0
    Close Cell#5_Sr
    Close Cell#3_La
72  Open Cell#6_Mn
    Pause 60.0
    Close Cell#6_Mn
    While End

77  Open Cell#6_Mn
    Pause 60.0
    Close Cell#6_Mn

    While Loop 5
82  Open Cell#3_La
    Open Cell#5_Sr
    Pause 60.0
    Close Cell#5_Sr
    Close Cell#3_La
87  Open Cell#6_Mn
    Pause 60.0
    Close Cell#6_Mn
    While End

92  Open Cell#6_Mn
    Pause 60.0
    Close Cell#6_Mn

    While Loop 5
97  Open Cell#3_La
    Open Cell#5_Sr
    Pause 60.0
    Close Cell#5_Sr
    Close Cell#3_La
102 Open Cell#6_Mn
    Pause 60.0
    Close Cell#6_Mn
    While End

107 Open Cell#6_Mn
    Pause 60.0
    Close Cell#6_Mn

    While Loop 4
112 Open Cell#3_La
    Open Cell#5_Sr
    Pause 60.0
    Close Cell#5_Sr
    Close Cell#3_La
117 Open Cell#6_Mn
    Pause 60.0
    Close Cell#6_Mn
    While End

122 Open Cell#6_Mn
    Pause 60.0
    Close Cell#6_Mn

    While Loop 4
127 Open Cell#3_La
    Open Cell#5_Sr
    Pause 60.0
    Close Cell#5_Sr
    Close Cell#3_La
132 Open Cell#6_Mn
    Pause 60.0
    Close Cell#6_Mn
    While End

137 Open Cell#6_Mn
    Pause 60.0
    Close Cell#6_Mn

    While Loop 3
142 Open Cell#3_La
    Open Cell#5_Sr
    Pause 60.0
    Close Cell#5_Sr
    Close Cell#3_La
147 Open Cell#6_Mn
    Pause 60.0
    Close Cell#6_Mn
    While End

152 Open Cell#6_Mn
    Pause 60.0
    Close Cell#6_Mn

    While Loop 3
157 Open Cell#3_La
    Open Cell#5_Sr
    Pause 60.0
    Close Cell#5_Sr
    Close Cell#3_La
162 Open Cell#6_Mn
    Pause 60.0
    Close Cell#6_Mn
    While End

167 Open Cell#6_Mn
    Pause 60.0
    Close Cell#6_Mn

    While Loop 2
172 Open Cell#3_La
    Open Cell#5_Sr
    Pause 60.0
    Close Cell#5_Sr
    Close Cell#3_La
177 Open Cell#6_Mn
    Pause 60.0
    Close Cell#6_Mn
    While End

182 Open Cell#6_Mn
    Pause 60.0
    Close Cell#6_Mn
```

```
While Loop 2
Open Cell#3_La
Open Cell#5_Sr
Pause 60.0
Close Cell#5_Sr
Close Cell#3_La
Open Cell#6_Mn
Pause 60.0
Close Cell#6_Mn
While End

Set Manipulator Setpoint 0.0
Set Manipulator Ramp Rate 20.0
Wait Until Manipulator Temperature < 100.0
Close MFC
End
```

B.1.4 MBE recipe visualization

To describe the vertical sample composition, the MBE recipe was used to get an image via gnuplot. For RHEED interpretation, the recipe information were printed behind the interpreted RHEED channel, immediately enabling the reader to investigate if the RHEED intensity follows the shutter opening times. In case of very complicated recipes with multiple loop-inside-loop structures, e.g. in recipe B.7, a visualization helped to check the outcome of the aimed sample.

The program "visualize_shutters.py"(B.8) is a tool designed to get a png image from a MBE recipe via once pressing the enter key. It scans which element shutters were opened to then plot that information as a colored rectangles vs. time.

The program accepts as input file any MBE recipe used for sample growth. For further changes in the png such as scaling or shifting an additional gnuplot file is created. The gpl script output for recipe in listing B.7 is shown in listing B.9, the image outputs for the four different recipe types in fig. B.1.

Listing B.8: MBE recipe visualization: Python file

```
'''
Version 0.9.2 - nearly finished, open for suggestions, code still not beautified and not
    documented, therefore not version 1.0
'''
import sys
import os
import re
import numpy as np
import subprocess
#material: everything after an "open" or "close", therefore e.g. La or E-Gun1; due to gnuplot
    interpretation of "-", E-Gun further called Gun

def parseline(lines, index, previous_times, current_state, previous_states):
    line = lines[index]
    words = line.split()
    if len(words) == 0:
        return True, index + 1
    if words[0] == 'Open':
        if not words[1] == 'Plasma' or not 'MFC':
            if len(words) != 2:
                print words
                exit("Open cell line does not contain exactly two words")
            material = extract_material(words[1:])
            if material is None:
                return True
            if current_state[material] == 1:
                exit("Trying to open material shutter twice")
            current_state[material] = 1
            return True, index + 1
    if words[0] == 'Close':
        if not words[1] == 'Plasma' or not 'MFC':
            if len(words) != 2:
                print words
                exit("Close cell line does not contain exactly two words")
            material = extract_material(words[1:])
            if material is None:
                return True, index + 1
            if current_state[material] == 0:
                exit("Trying to close material shutter twice")
            current_state[material] = 0
            return True, index + 1
    if words[0] == 'Pause':
        new_time = float(words[1]) + previous_times[-1]
        record_time(previous_times, new_time)
        record_states(previous_states, current_state)
```

```
            return True, index + 1
        if words[0] == 'While' and words[1] == 'Loop':
            repetition = int(words[2])
            for i in range(repetition):
                loop_index = index + 1
                continue_loop, loop_index = parseline(lines, loop_index, previous_times,
                    current_state, previous_states)
                while continue_loop:
                    continue_loop, loop_index = parseline(lines, loop_index, previous_times,
                        current_state, previous_states)
            return True, loop_index
        if words[0] == 'While' and words[1] == 'End':
            return False, index + 1
        return True, index + 1

    def record_time(previous_times, new_time):
        previous_times.append(new_time)

    def record_states(previous_states, new_states):
        for key in new_states.keys():
            previous_states[key].append(new_states[key])

    def extract_material(cellname):
        if re.search(r"^Cell#", cellname[0]) is not None:
            parts = cellname[0].split('_')
            if len(parts) != 2:
                print cellname
                exit("Cell␣name␣does␣not␣conform␣to␣format:␣Cell#x_M")
            return parts[1]
        if re.search(r"^E-Gun", cellname[0]) is not None:
            parts2 = cellname[0].split('-')
            return parts2[1]
        return None

    def get_initial_states(lines):
        result = {}
        for line in lines:
            words = line.split()
            if len(words) > 0:
                if words[0] == 'Open':
                    if not words[1] == 'Plasma' or not 'MFC':
                        if len(words) < 2:
                            print line
                            exit("Open␣cell␣line␣contains␣less␣than␣two␣words")
                        result[extract_material(words[1:])] = 0
        return result

    def parsefile(filename):
        inputfile = open(filename)
        filelines = inputfile.readlines()
        states = get_initial_states(filelines)
        state_history = {}
        for key in states:
            state_history[key] = []
        times = [0.0]
        inputfile = open(sys.argv[1])
        input_lines = inputfile.readlines()
        current_index = 0
        while current_index != len(input_lines):
            line_status, current_index = parseline(input_lines, current_index, times, states,
                state_history)
        return times, state_history

    if __name__ == '__main__':
        if len(sys.argv)!=2:
            exit("Usage:␣python␣visualize.py␣recipe.txt")
        time_vector, state_vector = parsefile(sys.argv[1])

    color_element = ['La', 'Mn', 'Co', 'Pt', 'Fe', 'Sr', 'Ti', 'Gun1', 'Gun2']
    color_code = ['\"#5AC449', '\"#A8089E', '\"#00005D', '\"#747489', '\"#8B6914', '\"#12DC0F', '
        \"#A52A2A', '\"#BFBFBF', '\"#FF0000']
    color_dictionary = dict(zip(color_element, color_code))
```

```
    ##to further use color_dictionary['(element)'] to get the colorcode

    sorted_elements=[]
    sorted_color=[]
    ytics_elements=[]
    for key in state_vector.keys():
        sorted_color.append(color_dictionary['{}'.format(key)])
        sorted_elements.append(key)
        ytics_elements.append('"{}" ({}+0.5)*a_intensity_scaling+a_intensity_shift'.format(key,str
            (state_vector.keys().index(key))))
        for i in ytics_elements:
            i.strip("'")
    #print sorted_color, sorted_elements, ytics_elements

    testoutput = "{}.gpl".format(os.path.splitext(os.path.basename(sys.argv[1]))[0])
    with open("%s" % testoutput, "w") as myfile:
        myfile.write('#set terminal windows font "Arial,16"'+'\n')
        myfile.write('#set size 800,600\n')
        myfile.write('set term pngcairo enhanced size 800,600 font "Arial,18" lw 2 nocrop \n')
        myfile.write('set output "{}.png"'.format(os.path.splitext(os.path.basename(sys.argv[1]))
            [0])+'\n\n')
        myfile.write('set grid'+'\n')
        myfile.write('set title "Recipe {}" \n'.format(os.path.splitext(os.path.basename(sys.argv
            [1]))[0]))
        myfile.write('a_time=0; a_intensity_shift=0; a_intensity_scaling=1'+'\n')
        myfile.write('#time=(value from MBE recipe)+a_time; intensity=(value from MBE recipe)*
            a_intensity_scaling+a_intensity_shift\n\n')
        myfile.write('xrange_end=1.05*{}'.format(time_vector[-1])+'+a_time\n')
        myfile.write('set xrange [0:xrange_end]'+'\n')
        myfile.write('set xlabel "Time [s]"'+'\n')
        myfile.write('set ylabel "Element Shutter" offset -5,0,0'+'\n')
        myfile.write('yrange_end=1.1*{}'.format(len(state_vector.keys()))+'*a_intensity_scaling+
            a_intensity_shift\n')
        myfile.write('#set yrange [:] \n')
        myfile.write('set yrange [0:yrange_end]'+'\n')
        myfile.write('set noytics \n') #necessary to see the labels doing the ytics
        for key in state_vector.keys():
            myfile.write('set label (1+'+str(state_vector.keys().index(key))+') at -xrange_end/10,
                '+str(state_vector.keys().index(key))+'+0.5 "'+key+'" \n')
        myfile.write('\n time_vector=\"'+str(time_vector).strip('[]')+'\"\n')
        myfile.write('item_time_vector(n) = word(time_vector,n)\n')
        for key in state_vector.keys():
            myfile.write(key + '=\"' + str(state_vector[key]).strip('[]')+'\"\n')
        for key in state_vector.keys():
            myfile.write('item_'+key+'(n) = word('+key+',n)\n')
        for key in state_vector.keys():
            myfile.write('do for [i=1:words('+key+')] { \n')
            myfile.write("set obj rect from item_time_vector(i)+a_time,(0+")
            myfile.write(str(state_vector.keys().index(key))+")*a_intensity_scaling+
                a_intensity_shift_to item_time_vector(i+1)+a_time,(item_"+key)
            myfile.write("(i)+"+str(state_vector.keys().index(key))+")*a_intensity_scaling+
                a_intensity_shift_fillcolor rgb "+color_dictionary['{}'.format(key)]+" behind")#
                item_sorted_color(i)
            myfile.write('\n}\n')
        myfile.write('\nplot x/1e7 notitle \n')
        myfile.write('#plot (RHEED-FILE) u 1:2 w l notitle lw 3 lc rgb "#FFA500" \n')
        myfile.write('exit')

    #following stuff for automatically created .png
    proc = subprocess.Popen(['gnuplot','-p'],
                            stdin=subprocess.PIPE,
                            )
    proc.stdin.write('load"{}'.format(os.path.splitext(os.path.basename(sys.argv[1]))[0])+'.gpl" \
        n')
    proc.communicate()
```

Listing B.9: MBE recipe visualization: Gnuplot file

```
#set terminal windows font "Arial,16"
#set size 800,600
set term pngcairo enhanced size 800,600 font "Arial,18" lw 2 nocrop
```

```
set output "131210-224ab-LSMO-STO.png"

set grid
set title "Recipe␣131210-224ab-LSMO-STO"
a_time=0; a_intensity_shift=0; a_intensity_scaling=1
#time=(value from MBE recipe)+a_time; intensity=(value from MBE recipe)*a_intensity_scaling+
     a_intensity_shift

xrange_end=1.05*8220.0+a_time
set xrange [0:xrange_end]
set xlabel "Time␣[s]"
set ylabel "Element␣Shutter" offset -5,0,0
yrange_end=1.1*3*a_intensity_scaling+a_intensity_shift
set yrange [0:yrange_end]
set noytics
set label (1+0) at -xrange_end/10,0+0.5 "Sr"
set label (1+1) at -xrange_end/10,1+0.5 "Mn"
set label (1+2) at -xrange_end/10,2+0.5 "La"

 time_vector="0.0,␣60.0,␣120.0,␣180.0,␣240.0,␣300.0,␣360.0,␣420.0,␣480.0,␣540.0,␣600.0,␣660.0,
     ␣720.0,␣780.0,␣840.0,␣900.0,␣960.0,␣1020.0,␣1080.0,␣1140.0,␣1200.0,␣1260.0,␣1320.0,␣
      1380.0,␣1440.0,␣1500.0,␣1560.0,␣1620.0,␣1680.0,␣1740.0,␣1800.0,␣1860.0,␣1920.0,␣1980.0,␣
      2040.0,␣2100.0,␣2160.0,␣2220.0,␣2280.0,␣2340.0,␣2400.0,␣2460.0,␣2520.0,␣2580.0,␣2640.0,␣
      2700.0,␣2760.0,␣2820.0,␣2880.0,␣2940.0,␣3000.0,␣3060.0,␣3120.0,␣3180.0,␣3240.0,␣3300.0,␣
      3360.0,␣3420.0,␣3480.0,␣3540.0,␣3600.0,␣3660.0,␣3720.0,␣3780.0,␣3840.0,␣3900.0,␣3960.0,␣
      4020.0,␣4080.0,␣4140.0,␣4200.0,␣4260.0,␣4320.0,␣4380.0,␣4440.0,␣4500.0,␣4560.0,␣4620.0,␣
      4680.0,␣4740.0,␣4800.0,␣4860.0,␣4920.0,␣4980.0,␣5040.0,␣5100.0,␣5160.0,␣5220.0,␣5280.0,␣
      5340.0,␣5400.0,␣5460.0,␣5520.0,␣5580.0,␣5640.0,␣5700.0,␣5760.0,␣5820.0,␣5880.0,␣5940.0,␣
      6000.0,␣6060.0,␣6120.0,␣6180.0,␣6240.0,␣6300.0,␣6360.0,␣6420.0,␣6480.0,␣6540.0,␣6600.0,␣
      6660.0,␣6720.0,␣6780.0,␣6840.0,␣6900.0,␣6960.0,␣7020.0,␣7080.0,␣7140.0,␣7200.0,␣7260.0,␣
      7320.0,␣7380.0,␣7440.0,␣7500.0,␣7560.0,␣7620.0,␣7680.0,␣7740.0,␣7800.0,␣7860.0,␣7920.0,␣
      7980.0,␣8040.0,␣8100.0,␣8160.0,␣8220.0"
item_time_vector(n) = word(time_vector,n)
Sr="0,␣1,␣0,␣1,␣0,␣1,␣0,␣1,␣0,␣1,␣0,␣1,␣0,␣1,␣0,␣1,␣0,␣0,␣1,␣0,␣1,␣0,␣1,␣0,␣1,␣0,␣1,␣0,␣1,␣0,␣
     1,␣0,␣0,␣1,␣0,␣1,␣0,␣1,␣0,␣1,␣0,␣1,␣0,␣1,␣0,␣1,␣0,␣0,␣1,␣0,␣1,␣0,␣1,␣0,␣1,␣0,␣1,␣0,␣1,␣0,␣
     0,␣1,␣0,␣1,␣0,␣1,␣0,␣1,␣0,␣1,␣0,␣1,␣0,␣0,␣1,␣0,␣1,␣0,␣1,␣0,␣1,␣0,␣1,␣0,␣0,␣1,␣0,␣1,␣0,␣1,␣
     0,␣1,␣0,␣1,␣0,␣0,␣1,␣0,␣1,␣0,␣1,␣0,␣1,␣0,␣0,␣1,␣0,␣1,␣0,␣1,␣0,␣1,␣0,␣0,␣1,␣0,␣1,␣0,␣1,␣0,␣
     0,␣1,␣0,␣1,␣0,␣1,␣0,␣0,␣1,␣0,␣1,␣0,␣0,␣1,␣0,␣1,␣0"
Mn="1,␣0,␣1,␣0,␣1,␣0,␣1,␣0,␣1,␣0,␣1,␣0,␣1,␣0,␣1,␣0,␣1,␣1,␣0,␣1,␣0,␣1,␣0,␣1,␣0,␣1,␣0,␣1,␣0,␣1,␣
     0,␣1,␣1,␣0,␣1,␣0,␣1,␣0,␣1,␣0,␣1,␣0,␣1,␣0,␣1,␣0,␣1,␣1,␣0,␣1,␣0,␣1,␣0,␣1,␣0,␣1,␣0,␣1,␣0,␣1,␣
     1,␣0,␣1,␣0,␣1,␣0,␣1,␣0,␣1,␣0,␣1,␣0,␣1,␣1,␣0,␣1,␣0,␣1,␣0,␣1,␣0,␣1,␣0,␣1,␣1,␣0,␣1,␣0,␣1,␣0,␣
     1,␣0,␣1,␣0,␣1,␣1,␣0,␣1,␣0,␣1,␣0,␣1,␣0,␣1,␣1,␣0,␣1,␣0,␣1,␣0,␣1,␣0,␣1,␣1,␣0,␣1,␣0,␣1,␣0,␣1,␣
     1,␣0,␣1,␣0,␣1,␣0,␣1,␣1,␣0,␣1,␣0,␣1,␣1,␣0,␣1,␣0,␣1"
La="0,␣1,␣0,␣1,␣0,␣1,␣0,␣1,␣0,␣1,␣0,␣1,␣0,␣1,␣0,␣1,␣0,␣0,␣1,␣0,␣1,␣0,␣1,␣0,␣1,␣0,␣1,␣0,␣1,␣0,␣
     1,␣0,␣0,␣1,␣0,␣1,␣0,␣1,␣0,␣1,␣0,␣1,␣0,␣1,␣0,␣1,␣0,␣0,␣1,␣0,␣1,␣0,␣1,␣0,␣1,␣0,␣1,␣0,␣1,␣0,␣
     0,␣1,␣0,␣1,␣0,␣1,␣0,␣1,␣0,␣1,␣0,␣1,␣0,␣0,␣1,␣0,␣1,␣0,␣1,␣0,␣1,␣0,␣1,␣0,␣0,␣1,␣0,␣1,␣0,␣1,␣
     0,␣1,␣0,␣1,␣0,␣0,␣1,␣0,␣1,␣0,␣1,␣0,␣1,␣0,␣0,␣1,␣0,␣1,␣0,␣1,␣0,␣1,␣0,␣0,␣1,␣0,␣1,␣0,␣1,␣0,␣
     0,␣1,␣0,␣1,␣0,␣1,␣0,␣0,␣1,␣0,␣1,␣0,␣0,␣1,␣0,␣1,␣0"
item_Sr(n) = word(Sr,n)
item_Mn(n) = word(Mn,n)
item_La(n) = word(La,n)
do for [i=1:words(Sr)]{
set obj rect from item_time_vector(i)+a_time,(0+0)*a_intensity_scaling+a_intensity_shift to
     item_time_vector(i+1)+a_time,(item_Sr(i)+0)*a_intensity_scaling+a_intensity_shift
     fillcolor rgb "#12DC0F␣behind
}
do␣for␣[i=1:words(Mn)]{
set␣obj␣rect␣from␣item_time_vector(i)+a_time,(0+1)*a_intensity_scaling+a_intensity_shift␣to␣
     item_time_vector(i+1)+a_time,(item_Mn(i)+1)*a_intensity_scaling+a_intensity_shift␣
     fillcolor␣rgb␣"#A8089E behind
}
do for [i=1:words(La)]{
set obj rect from item_time_vector(i)+a_time,(0+2)*a_intensity_scaling+a_intensity_shift to
     item_time_vector(i+1)+a_time,(item_La(i)+2)*a_intensity_scaling+a_intensity_shift
     fillcolor rgb "#5AC449␣behind
}

plot␣x/1e7␣notitle
#plot␣(RHEED-FILE)␣u␣1:2␣w␣l␣notitle␣lw␣3␣lc␣rgb␣"#FFA500"
exit
```

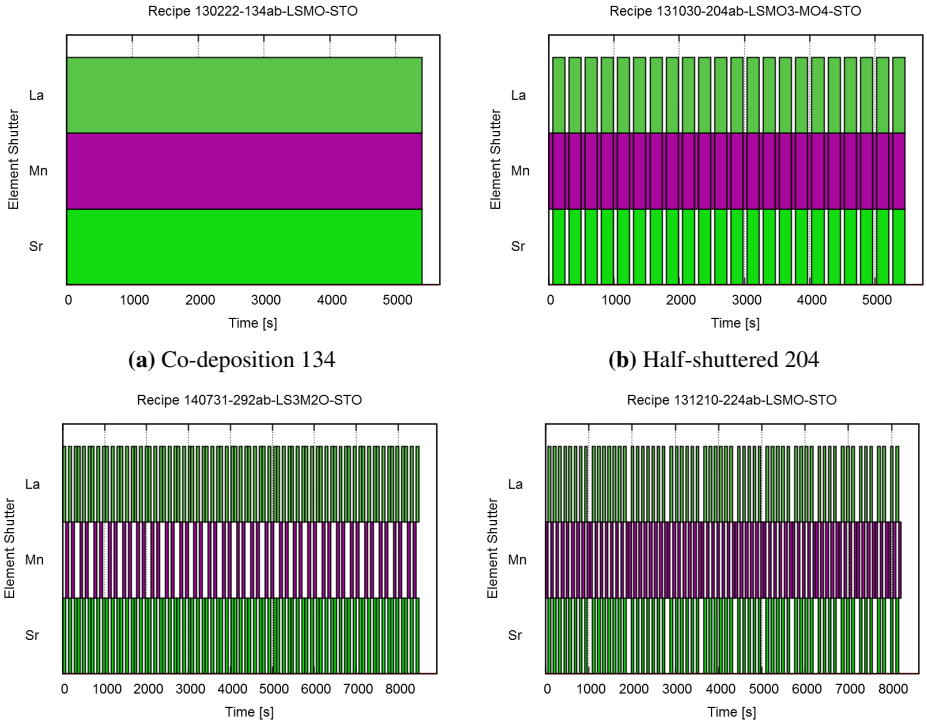

(a) Co-deposition 134

(b) Half-shuttered 204

(c) Fully shuttered 292

(d) Graded 224

Figure B.1: Visualization of MBE recipes immediately emphasizes difference of co-deposition, half-shuttered deposition and shuttered deposition; by bare eye, for the figure, the structural gradient can be identified

B.2 RHEED data visualization

To start RHEED discussions, in a first visualization the RHEED record (time vs. intensity) was printed with the MBE recipe in the background via gnuplot scripts like B.10. For easier comparison of the influence of certain lines inside recipe loop structures, after 12 to 15 shutter movings a line break was perfomed onto the RHEED signal and the MBE recipe; now, effects like "first unit cell after additionally introduced layer" can be analysed in contrast to each other via gnuplot scripts like B.11.

Listing B.10: RHEED intensity; in background MBE recipe

```
set terminal windows font "Arial,18"

blubb = "229ab-LSMO-STO-RHEED20131211.162707␣Window␣Data.txt"
set grid
set title "229ab-LSMO-STO"
set xrange [:10000]
set yrange [7:25]
#columncolors = "#0000FF #FF0000 #00FF00 #00FFFF #FF00FF #FF7F00 #7F00FF #008000 #800000
    #808000 #000080 #FFFF00 #0000FF"

#parameters from the [sample name]-rectangle.py which is based on the MBE recipe
c1=10; c2=20                #c1=y_min, c2=y_max of original graph; here: to calculate ytics
    positions
c3=12.979*60+8; c4=60               #c3=start time of deposition; c4=standard step size of
    time
c5 = 0                      #c5: Parameter to add up
##5AC449 is green, #A8089E is violet

#set of rectangles for visualization without line break; maybe easier than written inside MBE
    recipe

#1mal M - 7mal LS - M - 1 M - 6 LS - M

shutt = "7.␣6.␣5.␣4.␣3.␣2.␣2.␣3.␣4.␣5.␣6.␣7.␣8."

do for [b1 in shutt]{
set obj rect from c3+(c5+0)*c4,c1 to c3+(c5+1)*c4,c2 fillcolor rgb "#A8089E"
set for [i=0:b1] obj rect from c3+(c5+1+2*i)*c4,c1 to c3+(c5+2+2*i)*c4,c2 fillcolor rgb "#5
    AC449"
set for [i=0:b1] obj rect from c3+(c5+2+2*i)*c4,c1 to c3+(c5+3+2*i)*c4,c2 fillcolor rgb "#
    A8089E"
c5 = c5 + 2*b1 + 1
}

c3=396
i=6
plot blubb every ::c3+0+((i-2)*10800)::10799+((i-2)*10800) \
using ($1*60):($2*7/300) w l notitle lw 1 lc rgb "#FFA500"
```

Listing B.11: Linebreak version of listing B.10

```
set terminal windows font "Arial,18"

blubb = "140807-295ab-CenteredLS-LS4_5M3_5O-STOReal-time␣Window␣Analysis␣(␣Peak␣Int.␣).txt"
set grid
set title "295ab-LSMO-STO"
set xrange [0:1000]
set yrange [-400:100]
#columncolors: Special color code of first 17 ellipses of RHEED ksA program
columncolors = "#0000FF␣#FF0000␣#00FF00␣#00FFFF␣#FF00FF␣#FF7F00␣#7F00FF␣#008000␣#800000␣
    #808000␣#000080␣#FFFF00␣#0000FF␣#FF0000␣#F94BF2␣#00FFFF␣#00FF00"

set xlabel "Time␣[s]"
set ylabel "Intensity␣[a.u.]"

#parameters from the [sample name]-rectangle.py which is based on the MBE recipe
```

```
c1=65; c2=85                    #c1=y_min, c2=y_max of original graph; here: to calculate ytics
    positions
c3=12.;c4=76                     #c3=start time of deposition; c4=standard step size of time
c5 = 0                          #c5: Parameter to add up
##5AC449 is green, #A8089E is violet
#set of rectangles for visualization without line break; maybe easier than written inside MBE
    recipe

c11=0
shutt = "5. 5. 4. 4. 3. 3. 2. 2. 2. 2. 3. 3. 4. 4. 5. 5." #loop numbers from recipe
j=0

do for [b1 in shutt]{
set obj rect from c3+(c5+0)*c4,c1-c11 to c3+(c5+1)*c4,c2-c11 fillcolor rgb "#5AC449"
set for [i=0:b1-1] obj rect from c3+(c5+1+2*i)*c4,c1-c11 to c3+(c5+2+2*i)*c4,c2-c11 fillcolor
    rgb "#5AC449"
set for [i=0:b1-1] obj rect from c3+(c5+2+2*i)*c4,c1-c11 to c3+(c5+3+2*i)*c4,c2-c11 fillcolor
    rgb "#A8089E"
c5 = 0
c11 = c11 + 30
}

c11=30
#first plot legend linewith 14, then plot columns without legend; use ksA color code for
    columns
#plot for [i in "12. "] 1/0 w l t "0:".(int(i)-1) lw 14 lc rgb word(columncolors, int(i)-1),
#plot for [i in "12."] blubb u 1:int(i) w l notitle lw 1 lc rgb word(columncolors, int(i)-1)

#seconds per line: 11*c4, 11, 9, 9, 7, 7, 5, 5, 5, 5, 7, 7, 9, 9, 11, 11

sec_shift="0., 11., 22., 31., 40., 47., 54., 59., 64., 69., 74., 81., 88., 97., 106., 117."
sec_shift2="11., 22., 31., 40., 47., 54., 59., 64., 69., 74., 81., 88., 97., 106., 117., 128."
#Intensity shift per line: 0*c11, 1*c11, 2*c11, 3*c11, 4*c11, 5*c11, 6*c11, 7*c11...

item(n) = word(sec_shift,n)
item_2(n) = word(sec_shift2,n)
plot for [j=1:16] blubb every ::c3/2+(item(j))/2*c4::c3/2+(item_2(j))/2*c4 using ($1-(item(j))
    *c4):($12-(j-1)*c11) w l notitle lw 3 lc rgb "#FFA500"
```

Appendix C

Documentation: Logfiles and co.

C.1 Effusion Cell Rate Calibration

Logfiles of the gradient samples show that everything was ok for samples 224 (fig. C.2a) and 230 (fig. C.2b), and a short plasma collapse occured in sample production of 233 (fig. C.2c). Inside the logfile of sample 301a in fig. C.2d, additionally, the monitoring of the calibration sample is shown, first co-deposition, optimized calculations then leading to shuttered deposition, to cross-check the effusion cell rates via RHEED oscillations.

C.1.1 Temperature referencing

If STO is annealed in vacuum, it changes its color from white to grey. This is associated with oxygen vacancies and reversible. In the oxygen-deficient state, the carrier mobility is enhanced and a high colossal positive magnetoresistance is observed [108]. To see if the here used parameters lead to fully oxygen saturated samples, photos were taken after several heating steps in fig. C.5a. And indeed, oxygen vacancies shine blue [67]. Fig. C.5b proves the reversibility of these defects via annealing the sample inside the MBE setup in oxygen plasma. Fig. C.5c shows a photo of a sample directly after growth. The white sample corners in comparison to the grey (fully oxidized) LSMO film are the expected outcome; indeed, for all here investigated films the STO substrate has always a white color after sample production.

C.1.2 La evaporation via e-gun

For testing reasons, a few attempts were performed to grow LSMO with Sr and Mn from effusion cells and La via e-gun. The major challenge was the difference in the rates with and without oxygen. While for effusion cells the element output did not change with added oxygen plasma, the quartz monitor measured the oxides SrO, MnO to Mn_3O_4 instead of elements Sr or Mn, depending on the amount of oxygen flow. Pure and oxidized rates were monitored allowing the stability of element rates to be established. However, for the e-guns, the quartz crystal balance rates were also raised due to the additional oxygen, anyhow, the electron beam itself was scattered at the additional oxygen inside the chamber and therefore decreased in intensity. The precision of the quartz monitors as well as the stability of electron beam was not good enough to adjust the La rate with additional oxygen to achieve a LSMO stoichiometry despite attempts lasting few months and therefore an additional effusion cell was bought.

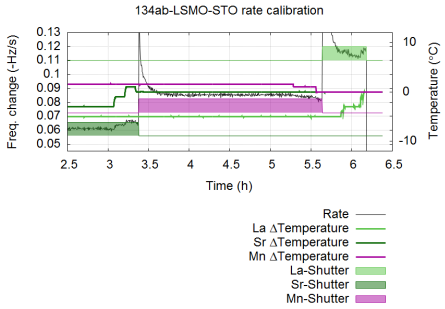

(a) Effusion cell rate calibration before growth of sample 134 (LSMO)

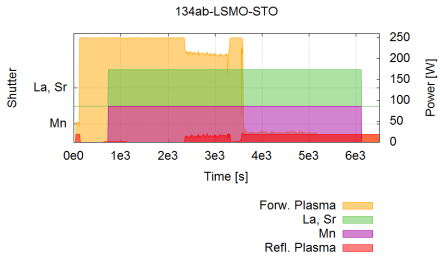

(b) Sample 134: Logfile during growth

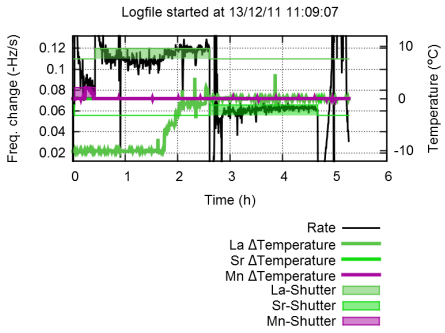

(c) Logfile 230 calibration

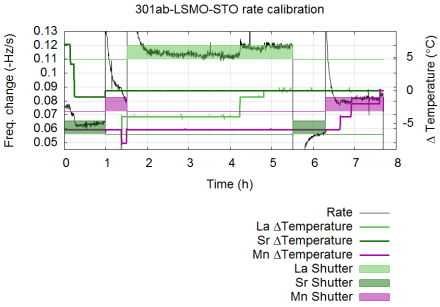

(d) 301 (LSMO)

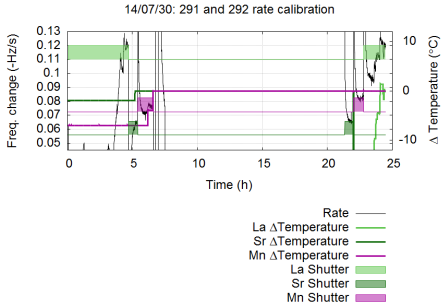

(e) 292 $(LS)_3M_2O$

Figure C.1: Logfiles of different samples regarding Quartz Crystal Balance for rate calibration

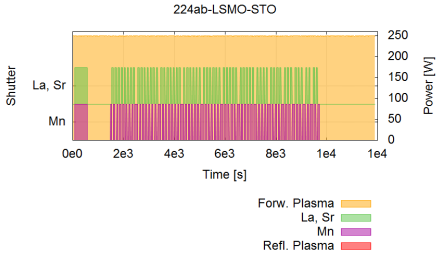

(a) Logfile 224 (top Mn excess)

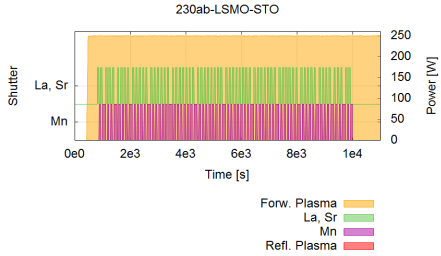

(b) Logfile 230 (edged Mn excess)

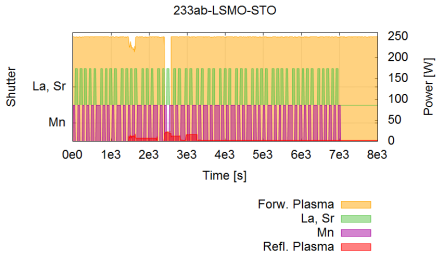

(c) Logfile 233 (centered Mn excess)

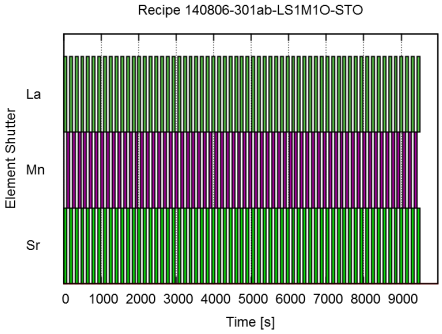

(d) MBE recipe 301ab

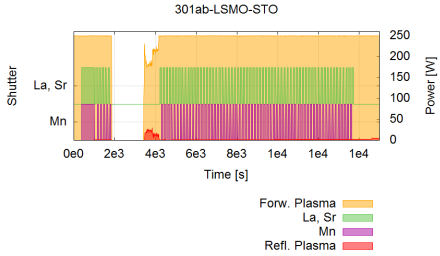

(e) Logfile for 301ab

Figure C.2: Logfiles of gradient samples: Everything ok for samples 224 and 230, short plasma collapse in sample production of 233

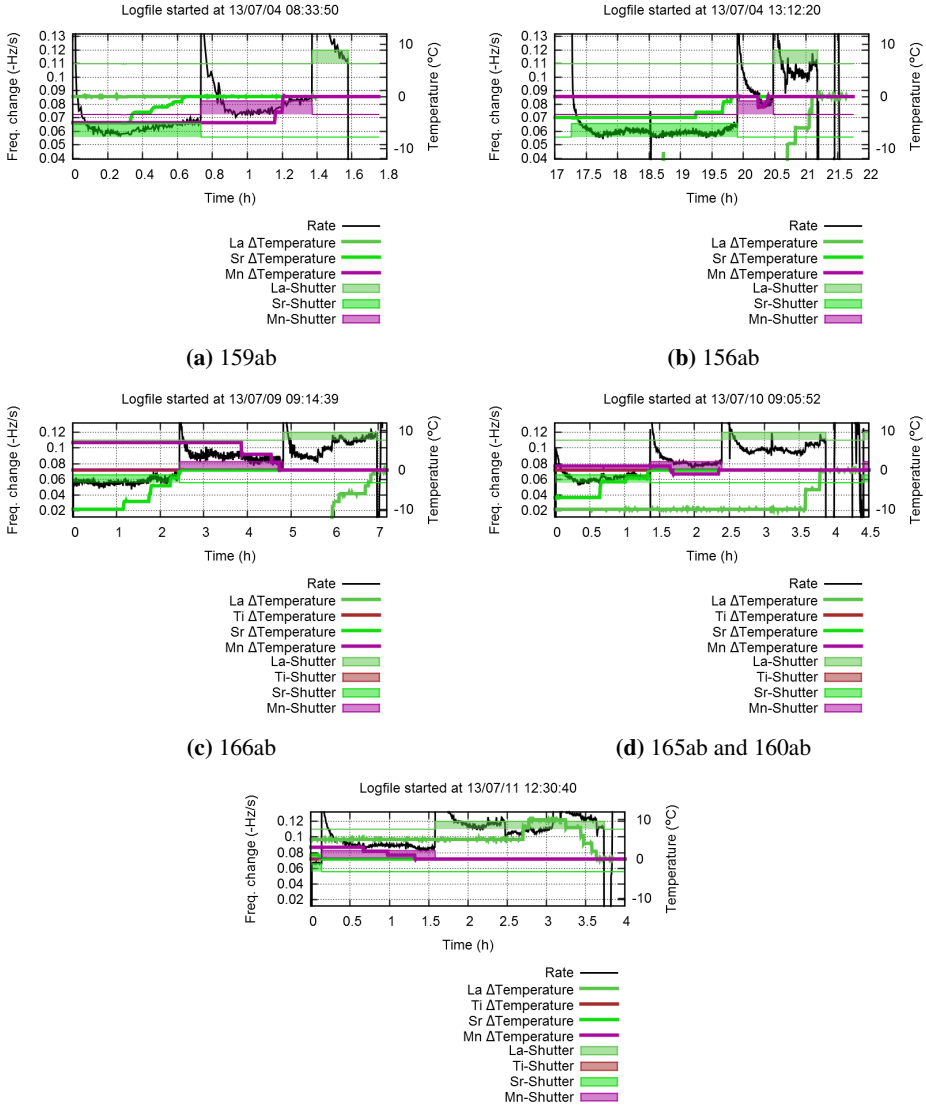

(a) 159ab

(b) 156ab

(c) 166ab

(d) 165ab and 160ab

(e) 168ab

Figure C.3: Logfiles 156ab-168ab regarding Quartz Crystal Balance for rate calibration

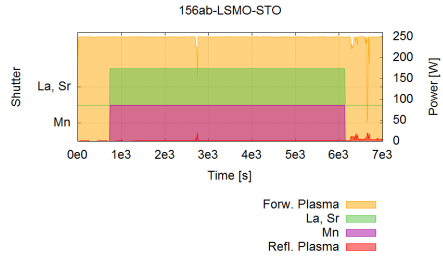

(a) 156ab

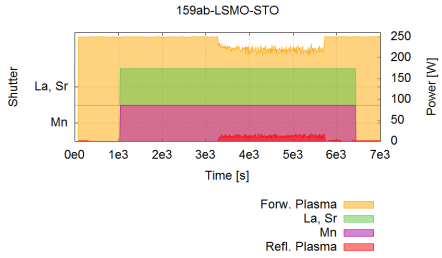

(b) 159ab

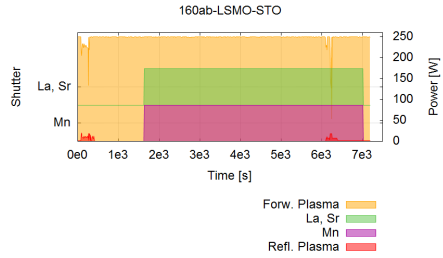

(c) 160ab

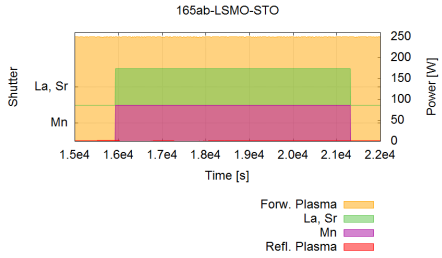

(d) 165ab

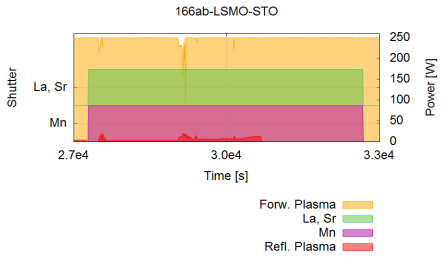

(e) 166ab

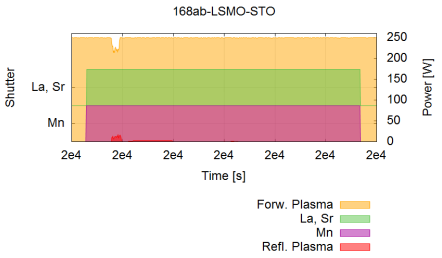

(f) 168ab

Figure C.4: Logfiles of sample series 156ab-168ab during growth

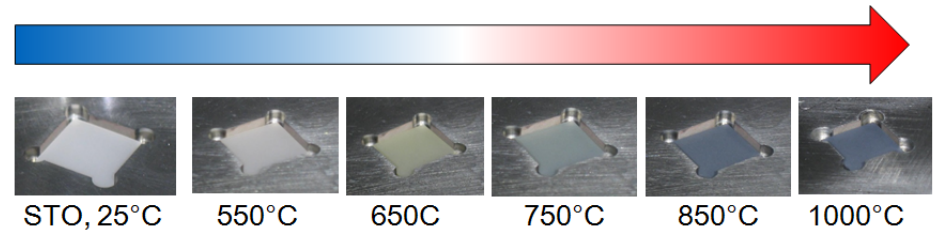

(a) STO substrate was heated at different temperatures in UHV; temperature-and-vacuum-induced color changes in agreement with literature [67]

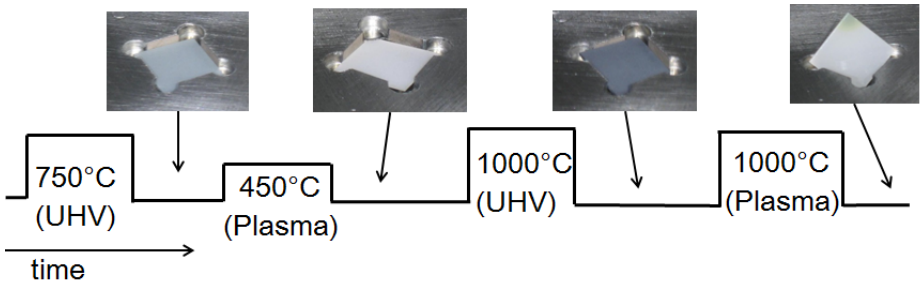

(b) STO substrate was heated several times, either in UHV or in oxygen plasma: The $SrTiO_3$ color changes are reversible

(c) LSMO/STO: After preparation, deposited LSMO shows color expected for 20nm thin film, while STO corners without deposited LSMO are white indicating no oxygen deficiencies

Figure C.5: $SrTiO_3$: Typical colors of used substrates are attributed to substrate heating history in UHV or oxygen plasma

Appendix D

List of Symbols and Abbreviations

D.1 Symbols

	Sample Composition
LSMO	$La_{2/3}Sr_{1/3}MnO_3$
LSO	$La_{2/3}Sr_{1/3}O$
LS:M	$(La_{2/3}Sr_{1/3})$ to (Mn) ratio; in $La_{2/3}Sr_{1/3}MnO_3$ 1:1
concLS:M	value of $(La_{2/3}Sr_{1/3})_{2*(1-concLS:M)}(Mn)_{2*concLS:M}O_3$; in $La_{2/3}Sr_{1/3}MnO_3$ 0.5
MO	MnO_x
STO	$SrTiO_3$
	Physical Nomenclature
a, b	in-plane lattice parameters
c	out-of-plane lattice parameter
d	layer thickness
FFT	Fast Fourier Transform
h, k	Miller indices of in-plane reciprocal lattice vectors
H, K	Miller indices normalized to reciprocal lattice units
l	Miller index of out-of-plane reciprocal lattice vector
L	Miller index normalized to reciprocal lattice units
λ	Wavelength
Q_z	Scattering vector
sccm	Standard Cubic Centimeters per Minute (T_n= 0 °C, P_n= 1.01 bar)
SLD	Scattering Length Density
SLD-δ	real part of scattering length density
σ	Roughness
T_C	Transition temperature to ferromagnetic order
$V(\vec{r})$	Scattering potential

D.2 Abbreviations

	Methods and instruments
AES	Auger Electron Spectroscopy
AFM	Atomic Force Microscopy
EDX	Energy-Dispersive X-ray spectroscopy
FIB	Focussed Ion Beam
FOM	Figure of merit
HAADF	High-Angle Annular Dark-Field
LEED	Low Energy Electron Diffraction
MARIA	MAgnetism Reflectometer with high Incident Angle@MLZ
MBE	Molecular Beam Epitaxy
MR	Magnetism Reflectometer@SNS
PNR	Polarized Neutron Reflectometry
QCB	Quartz Crystal Balance
RBS	Rutherford Backscattering Spectrometry
RHEED	Reflection High-Energy Electron Diffraction
SEM	Scanning Electron Microscopy
SQUID	Superconducting QUantum Interference Device
STEM	Scanning Transmission Electron Microscopy (STEM)
TEM	Transmission Electron Microscopy
TREFF	Temporary reflectometer for polarized neutron reflectometry@MLZ
XRD	X-Ray Diffraction
XRR	X-Ray Reflectivity
	Affiliations
ER-C	Ernst Ruska-Centre for Microscopy and Spectroscopy with Electrons (Forschungszentrum Jülich GmbH)
JCNS	Jülich Centre for Neutron Science (Forschungszentrum Jülich GmbH)
MLZ	Heinz Maier-Leibnitz Zentrum
WMI	Walther-Meißner-Institute for Low Temperature Research (Bavarian Academy of Sciences and Humanities)
PGI	Peter Grünberg Institute (Forschungszentrum Jülich GmbH)
CAU	Christian-Albrechts-Universität zu Kiel

Band / Volume 114
Single-Cell Analysis of Microbial Production Strains in Microfluidic Bioreactors
A. M. Grünberger (2015), XIX, 225 pp
ISBN: 978-3-95806-092-0

Band / Volume 115
Magnetic order and spin dynamics in the extended kagome system $CaBaCo_2Fe_2O_7$
J. Reim (2015), viii, 144 pp
ISBN: 978-3-95806-097-5

Band / Volume 116
Structural and electronic investigations on homo- and hetero-organic layers involving CuPc on silver single crystal surfaces
K. M. Schönauer (2015), x, 148 pp
ISBN: 978-3-95806-112-5

Band / Volume 117
First-principles investigation of inelastic magnetic excitations in nanostructures deposited on surfaces
B. J. Schweflinghaus (2016), v, 204 pp
ISBN: 978-3-95806-115-6

Band / Volume 118
Magnetic, structural, and electronic properties of $NiFe_2O_4$ ultrathin films
M. Hoppe (2016), vii, 118 pp
ISBN: 978-3-95806-122-4

Band / Volume 119
First-principle investigation of displacive response in complex solids
D. A. Klüppelberg (2016), xi, 179 pp
ISBN: 978-395806-123-1

Band / Volume 120
Beam Cooling at COSY and HESR - Theory and Simulation -
Part 1 Theory
H. Stockhorst, T. Katayama and R. Maier (2016), v, 192 pp
ISBN: 978-3-95806-127-9

Band / Volume 121
Scanning tunneling microscopy of single-molecule magnets and hybrid-molecular magnets: Two approaches to molecular spintronics
V. Heß (2016), x, 127 pp
ISBN: 978-3-95806-128-6

Band / Volume 122
Bulk and surface sensitive energy-filtered photoemission microscopy using synchrotron radiation for the study of resistive switching memories
M. C. Patt (2016), viii, 247 pp
ISBN: 978-3-95806-130-9

Band / Volume 123
Group IV Epitaxy for Advanced Nano- and Optoelectronic Applications
S. Wirths (2016), vi, 116, XXX pp
ISBN: 978-3-95806-132-3

Band / Volume 124
Strained Silicon-Germanium/Silicon Heterostructure Tunnel FETs for Low Power Applications
S. Blaeser (2016), iv, 91, xvii pp
ISBN: 978-3-95806-135-4

Band / Volume 125
Nanocavity Arrays for Extracellular Recording and Stimulation of Electroactive Cell Systems
A. Czeschik (2016), x, 162 pp
ISBN: 978-3-95806-144-6

Band / Volume 126
Band Structure Engineering in 3D Topological Insulators Investigated by Angle-Resolved Photoemission Spectroscopy
M. Eschbach (2016), VIII, 153 pp
ISBN: 978-3-95806-149-1

Band / Volume 127
Dynamics in colloid and protein systems: Hydrodynamically structured particles, and dispersions with competing attractive and repulsive interactions
J. Riest (2016), ix, 226 pp
ISBN: 978-3-95806-153-8

Band / Volume 128
Self-purifying $La_{2/3}Sr_{1/3}MnO_3$ epitaxial films: Observation of surface precipitation of Mn_3O_4 particles for excess Mn ratios
A. Steffen (2016), 154 pp
ISBN: 978-3-95806-162-0

Schlüsseltechnologien /
Key Technologies
Band / Volume 128
ISBN 978-3-95806-162-0